UNIVERSITY
of
GLASGOW

Gravitational Microlensing as a Diagnostic Tool for Stellar Astrophysics

by

Helen M. Bryce B.Sc. Hons.

Thesis
submitted to the
University of Glasgow
for the degree of
Ph.D.

Astronomy and Astrophysics Group

Department of Physics and Astronomy,

University of Glasgow,

Glasgow G12 8QQ

October 2001

PAGE NUMBERING AS FOUND IN THE ORIGINAL THESIS

Tuesday 21st August

Number of days of studentship: 1056 *(Thank-you for the sponsorship PPARC); Number of emotional pantwittage-type involvements:* 6 *(poor); Number of incidents involving answer machine mishaps/accidental dials:* 54 [1] *(v poor); Number of times cancelled credit cards due to loss within own flat;* 3*(v v poor)*

Hurrah, the thesis years are over! Must remember splendid members of Astronomy and Astrophysics group for all their help/friendship/tolerance over the last three years.

In particular, poor Martin has suffered with his first 'complete' PhD student, am so grateful for his generosity, ability to speak 'Poppet', reassurance about lack of 'mince'. Discussions of my work were always enjoyable (especially when accompanied by yummy home-baking on South Ronaldsay).

Wish also to model myself into super-woman, in manner of Daphne/Eve, never forget birthdays, special occasions, pet's names... Their gentle female support has been greatly appreciated and would happily buy any self help book they ever choose to write, especially if it gives advice on remembering to carry headache pills and stamps.

Unfortunately, Norman's sartorial advice will never pay off, am lost cause in battle of compacting wardrobe. However, all other advice was received gratefully. Must thank Graeme, also, for spoiling me in manner of small child unable to tie own shoelaces, but in v nice way. Gail has not only miraculously survived nearly three years with me in confined space, but, also managed to convince me that I could go running without inspiration of half price bargain shopping.

Must also thank wonderful friends; Amy, Derek, Gillean, Graham, Jane, Kathy, Kirstin, Lois, Lorna and Steven for gossip, dancing, parlour games, Kylie/Steps, dressing Barbies, being kind about my culinary skills and laughing about my dreadful taste in men.

Would also like to thank my mother for her consistently awful tea and her amusing penchant for department-store-coffee-shops and my sisters, Pamela and Laura for being better than me at ski-ing and cooler than me, respectively.

[1] *approximate*

Summary

This thesis is concerned with the microlensing of galactic sources and how such observations may be used to model and constrain the sources themselves. Gravitational microlensing has become a rapidly expanding field in recent years, with several hundred events having been detected, many with densely sampled high precision multi-wavelength photometry. This thesis explores how such observations could be used in order to extract information about the source, rather than the lens itself. Several aspects of extended source microlensing are discussed for both point mass lenses and fold caustic crossing events.

Chapter One introduces the theory of galactic microlensing and develops the necessary formulae needed to discuss extended source events in the subsequent Chapters. Some of the complications encountered by groups observing such events are discussed, as are a few of the more notable events themselves.

In Chapter Two an extended source model for microlensing is presented and applied to different atmosphere models, with different surface brightness profiles including simple one and two parameter limb darkening models and the more sophisticated and recently developed "Next Generation" stellar atmosphere models. It is shown that microlensing can distinguish between these different surface brightness profiles and thus, the underlying stellar atmosphere models, for realistic observational strategies.

In Chapter Three a second stellar atmosphere model is introduced. This model includes the effects of a non-radial surface brightness profile, i.e. starspots. Such effects are interesting for several reasons. Firstly, the existence or otherwise of starspots is an important indicator of stellar surface activity and would provide valuable information for the testing and development of more sophisticated stellar atmosphere models. Additionally, there has been concern that starspots could mimic planetary microlensing lightcurves making it important to consider how their observational signatures could be distinguished from those of planets. The microlensing signatures of starspots are considered for point mass lens in Chapter Three and for fold caustic crossings in Chapter Four.

In Chapter Five the extended source model used previously is applied to a source model

with a small level of radial and temperature variability, to allow examination of how such events, if observed, would compare to standard microlensing events.

In Chapter Six an investigation is made of the spectroscopic signatures of microlensing from circumstellar envelopes and the opportunities of using microlensing to diagnose bulk motion in these envelopes during caustic crossing events is examined.

In Chapter Seven the short comings of this work and suggestions for improvements and future work are considered.

The contents of this thesis represent original work carried out by the author at the University of Glasgow, in collaboration with Martin Hendry, Rico Ignace, David Valls-Gabaud and Norman Gray. Where results presented here have been previously published, this is indicated clearly in the text. In particular, Chapter Two represents research made in collaboration with Martin Hendry and Norman Gray, the research presented in Chapters Three and Four was done in collaboration with Martin Hendry and David Valls-Gabaud and Chapter Six represents research made in collaboration with Martin Hendry and Rico Ignace.

Contents

List of Tables

List of Figures

Chapter 1

Review

Gravitational microlensing has developed into a useful technique for studying stellar astrophysics over the past 15 years. Searches for microlensing events involving sources and lenses within the Local Group were initiated in an attempt to study dark matter in the galactic halo. The success of these searches – in terms of the numbers of microlensing events that have been identified – have re-inforced the status of microlensing as a technique that can allow study of stellar astrophysics on many levels; including stellar masses, binary systems and, as will be dealt with in great detail in this thesis, stellar atmospheres.

1.1 Classical microlensing

Whilst a point mass lens will produce two images of the lensed object, in the case of microlensing these images cannot currently be resolved as they are typically separated by microarcseconds (hence *micro*lensing). And, so microlensing can only be detected when the lens is moving with respect to the source. This motion provides a variation in the brightness of the source with time – as opposed to a static macrolens system.

Microlensing was suggested by Paczyński (1986) as a means of detecting the dark matter MACHOs believed to populate the Milky Way's halo. The existence of such objects is implied by the galactic rotation curve. For a spiral galaxy comprised of a thin flat disk

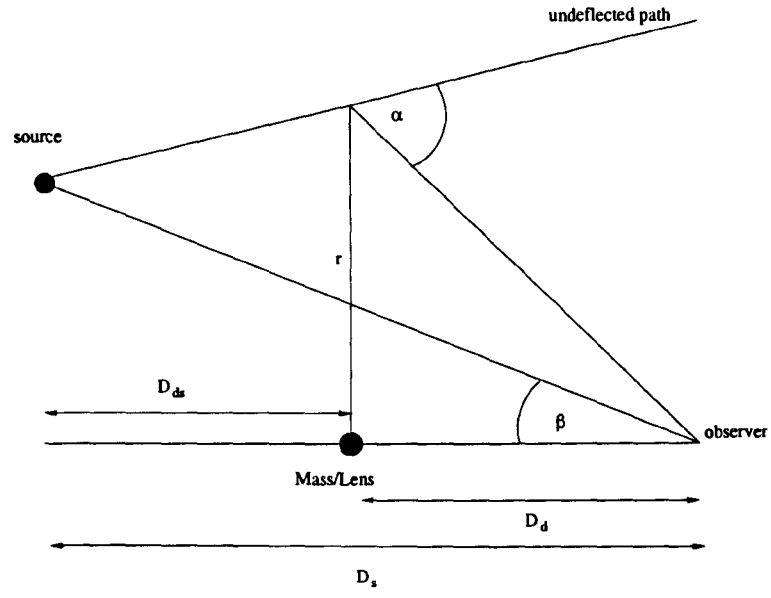

Figure 1.1: The geometry of a Schwarzschild lens

and a massive central bulge, a star at a distance, r, from the galactic centre would, from Kepler's third law, have an orbital velocity proportional to $r^{-1/2}$. In contrast, the Milky Way's rotation curve becomes flat at large distance from the centre. This flattening can be explained by the presence of a roughly sperical halo around the galaxy with a mass comparable, at least, to that of the galaxy itself. By intensive observations of a dense field of stars (such as the Large Magellanic Cloud) just outside the Milky Way's halo, one might hope to find small variations in apparent magnitude due to the lensing effects of any MACHOs. Thus the presence (or otherwise) of the MACHOs would be revealed.

The point mass lens, point source model of microlensing is described by the Schwarzschild lens, (Refsdal, 1964) the geometric optics of which are shown in Figure 1.1.

For a light ray to reach the observer it must satisfy the condition

$$\beta D_s = \frac{D_s}{D_d} r - \alpha D_{ds} \tag{1.1}$$

where the deflection angle, α, given by general relativity is

$$\alpha = \frac{4GM}{c^2 r} = \frac{2R_S}{r} \tag{1.2}$$

for a given impact parameter, r, where M is the mass of the lens and R_S is the Schwarzschild

radius of the lens. D_d, D_s and D_{ds} are the distances from observer to lens (or deflector), observer to source and lens to source respectively.

The angular distance between the lens and the observed light ray, in the lens plane, is

$$\theta = \frac{r}{D_d} \tag{1.3}$$

The angular Einstein radius (AER), the characteristic scale in gravitational lensing, is defined as,

$$\theta_0 = \sqrt{2R_s \frac{D_{ds}}{D_d D_s}} \tag{1.4}$$

For a galactic microlensing situation where the typical image seperations are of the order of *milli*arcseconds, despite the historical retention of the *mirco* nomenclature, we can rewrite this as

$$\theta_0 = 0.907 \sqrt{\frac{M}{M_\odot}} \sqrt{\frac{10\text{kpc}}{D_d}} \sqrt{1 - \frac{D_d}{D_s}} \text{ milliarcseconds} \tag{1.5}$$

In the source plane the Einstein radius becomes

$$\xi_0 = \theta_0 D_s = \sqrt{2R_s \frac{D_s D_{ds}}{D_d}} \tag{1.6}$$

The lens equation 1.1 becomes

$$\theta^2 - \beta\theta - \theta_0^2 = 0 \tag{1.7}$$

which has solutions

$$\theta_{+-} = \frac{1}{2}(\beta \pm \sqrt{4\theta_0^2 + \beta^2}) \tag{1.8}$$

corresponding to the positions of the two images of the source, with the images located on opposite sides of the lens. The *major* image is formed on the 'outside' of the Einstein ring (denoted by the subscript + in the following equations) and the *minor* image is formed 'inside' the Einstein ring (denoted by the subscript −).

As lensing conserves surface brightness, the magnification is equal to to the ratio of the image to source areas,

$$A_{+-} = \left| \frac{\theta_{+-}}{\beta} \frac{d\theta_{+-}}{d\beta} \right| = \frac{u^2 + 2}{2u(u^2 + 4)^{1/2}} \pm 0.5, \tag{1.9}$$

where,

$$u = \frac{\beta}{\theta_0}, \tag{1.10}$$

is the projected lens source separation normalised to the Einstein radius. The total magnification of the two images is therefore,

$$A = A_+ + A_- = \frac{u^2+2}{u\sqrt{u^2+4}} \tag{1.11}$$

The magnification of the source is always greater than 1, and the difference in the magnification between the two images is always constant.

$$A_+ - A_- = 1 \tag{1.12}$$

A point source at an angular distance of one Einstein radius from the lens will be amplified by a factor of $3/\sqrt{5} \equiv 1.34$. If the lens moves with uniform transverse velocity, $v_\perp$, relative to the observer-source line of sight, then the lens-source separation, u, is given by

$$u(t) = \sqrt{\frac{(t-t_0)^2}{t_E^2} + u_0^2} \tag{1.13}$$

where u_0 is the minimum impact parameter in units of the Einstein radius, t_0 is the time corresponding to this impact parameter – thus the time of maximum magnification. The lensing timescale, t_E, is defined as the time taken for the lens to cross one Einstein radius,

$$t_E = \frac{\theta_0 D_d}{v_\perp} \tag{1.14}$$

which can be rewritten as

$$t_E = 0.214\sqrt{\frac{M}{M_\odot}}\sqrt{\frac{D_d}{10\mathrm{kpc}}}\sqrt{1-\frac{D_d}{D_s}}\sqrt{\frac{200\mathrm{km\,s^{-1}}}{v_\perp}}\ \mathrm{years} \tag{1.15}$$

Thus a star in the Large Magellanic Cloud, at a distance of about 50 kpc when lensed by a $1\,M_\odot$ MACHO in the halo of the Milky Way with a proper motion of $200\,\mathrm{km\,s^{-1}}$ will have a lensing timescale of about 3 months.

It is only the timescale, t_E, that can be determined from a point lens microlensing event lightcurve, that (has a value that) is of any real interest in directly identifying MACHOs. The other parameters, the baseline and peak flux and the time of the peak flux are not

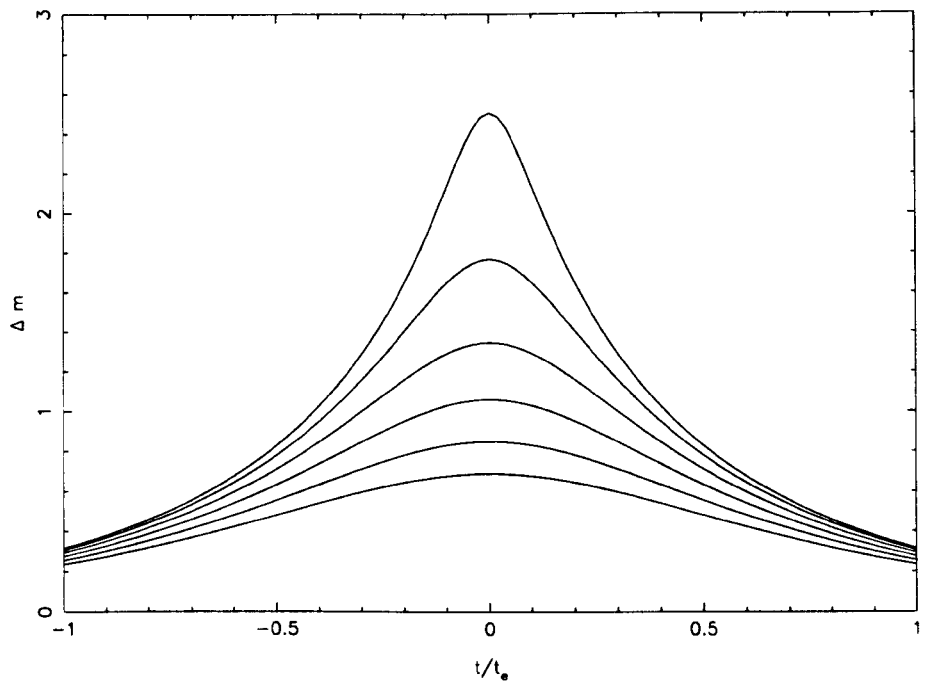

Figure 1.2: The variation of the magnification due to a point gravitational lensing event shown in magnitudes as a function of time. The lightcurves correspond to six values of minimum impact parameter $u_0 = 0.1, 0.2, 0.3, 0.4, 0.5$ and 0.6 normalised to the Einstein radius with the smallest value of the minimum impact producing the largest magnitude change.

at all dependent on the lens parameters. The timescale is a combination of the lens mass, transverse velocity and its position relative to the observer and source. Whilst microlensing can identify that a MACHO has passed within an Einstein radius of a source, it cannot determine the mass of the MACHO or its position directly.

The final major consideration that we are concerned with in setting up the most relevant equations is that of "microlensing optical depth", τ. This can be thought of as the instantaneous probability that a source star is amplified by a microlens with an amplification greater than 1.34, i.e. an amplification caused by a microlens approaching a source at a projected separation of one Einstein radius. The microlensing optical depth can also be thought of as the fraction of the solid angle of the sky, covered with the Einstein rings of all the possible microlenses. To calculate this, let us consider a thin slab of sky, of thickness ΔD_d, at a distance of D_d, where there is one lens per surface area $\pi R_M^2 = M/\rho \Delta D_d$, where ρ is the average mass density due to lenses in the volume $\pi R_M^2 \Delta D_d$ and R_M is the radius of the area of sky being considered. All the lenses have identical mass, M and so cross sections, πR_E^2 where R_E is the Einstein radius of the lens. This thin slab contributes

$\Delta\tau$ to the optical depth, where $\Delta\tau$ is found as

$$\Delta\tau = \frac{\pi R_E^2}{\pi R_M^2} = \left[\frac{4\pi G\rho}{c^2}\frac{D_d D_{ds}}{D_s}\right]\Delta D_d \tag{1.16}$$

The total optical depth to all lenses is then

$$\tau = \int_0^{D_s} \frac{4\pi G\rho}{c^2}\frac{D_d D_{ds}}{D_s}\,\mathrm{d}D_d \tag{1.17}$$

It is worth noting that the optical depth depends on the total masses of all the lenses, not on the mass distribution of the individual lenses.

It is the microlensing optical depth which gives a measure of the quantity of lensing matter in the line of sight and, thus, a measure of the quantity of dark matter. However, the optical depth to sources in the Magellanic Clouds was predicted as being very low ($< 10^{-6}$) implying that less than one star in a million will be subject to an amplification greater than 1.34 at any instant: this necessitates that only dense star fields can economically be monitored for microlensing events.

1.2 Microlensing Surveys

The ongoing microlensing surveys have now reported several hundred candidate microlensing events. Each survey is, or has been, monitoring dense star fields, such as the Large and Small Magellanic Clouds, the galactic bulge and M 31 for variability that can be attributed to microlensing. In order to identify successfully a microlensing event several checks are made using the available observations. To summarise greatly these procedures the three main conditions are.

- Symmetry: The amplification of a source due to microlensing will produce a symmetric lightcurve, whereas an intrinsic variation in the star's luminosity is unlikely to produce a perfectly symmetric lightcurve.

- Achromaticity: As the magnification function is frequency independent, the microlensing lightcurves should be the same at all wavelengths.
- Uniqueness: The probability of the same star being lensed twice is very small. Hence, sources which exhibit repeated variability are excluded.

In practice many 'real' microlensing events will not conform to these criteria. We will examine such situations in the following Section.

Three major collaborations (MACHO, (Alcock et al., 2000) OGLE, (Udalski et al., 2000) EROS, (Ansari et al., 1996)) have been surveying dense star fields in order to detect microlensing events. The MACHO project had full time use of a 1.27 m telescope for 8 years. Using two sets of criteria to select candidates 17 events were found towards the Magellanic Clouds. The majority of the events ($\sim$ 200) were found towards the galactic bulge. Both the EROS and the OGLE groups are still observing, with the OGLE group initiating an early warning system for events in progress. This allows follow-up observing programs to further examine the events as they happen. These follow-up programs include PLANET, MPS (Rhie et al. 2000) and MOA (Abe et al. 1997) and utilise a variety of telescopes at different locations and with different data reduction techniques. The motivation for intensive follow-up monitoring of events is principally the search for extra-solar planets. Planetary microlensing signatures arise due to deviations, from the point mass point source lightcurves, that can be induced by the presence of a companion of the lens. Microlensing is most sensitive to Jovian mass planets at a few AU – the so called lensing zone (Gaudi and Sackett 2000). These types of observations are also ideal for studying stellar atmospheres as the data are frequently sampled and of good photometric quality. A "pixel" microlensing technique has also been employed in the search for MACHOs (see e.g Kerins et al. 2000). This technique has been developed in order to detect events in highly crowded fields where individual sources cannot be resolved.

1.3 Beyond the Standard Model

The majority of microlensing events do indeed closely follow the equations laid out above and so have lightcurves corresponding to Figure 1.2. There are, however, several complications that will result in microlensing lightcurves that are not symmetric, achromatic and could even repeat. In this Section we will address some of these complications. As we shall see these complications have actually made the microlensing technique applicable to more than just the search for MACHOs.

1.3.1 Parallax

In Equation 1.13 we assume the relative motion of the lens is rectilinear. This assumption begins to break down if the event lasts longer than a few months. The Earth's motion around the Sun produces small changes in the relative motion of the lens and hence the lens to source separation. This, so called, "parallax" effect produces small (and predictable) asymmetries in the lightcurve. These effects have been detected during long timescale events (Alcock et al. 1995). As the effects occured as predicted it was an excellent confirmation that microlensing was responsible for the amplification rather than intrinsic stellar variability.

1.3.2 Blending

Microlensing surveys monitor dense star fields for reasons of economy, maximising the number of events that can be seen in a fixed number of observations. In such dense fields, however, it is often not possible to resolve individual source stars. This means that frequently microlensing lightcurves are contaminated by other unlensed sources. This introduces an additional baseline flux which requires the addition of an extra parameter, to the microlensing lightcurve fitting, such as

$$F = F_0 A(t) + B \tag{1.18}$$

where F is the total flux observed from the event, F_0, the unlensed flux from the source only, $A(t)$ is the amplification function and B is the flux from any unresolved background starlight, the "blend" which is constant throughout the event.

In fact a highly blended event may not actually be recognised as a microlensing event at all as it may appear not to be amplified by the threshold 1.34 value. On the other hand, blending allows events to be detected when the source star is not actually resolved, blending increases the number of sources a survey is sensitive to and hence the number of sources the survey is monitoring. DiStefano and Esin (1995) showed that blending causes systematic underestimation of A_{max} and t_E. Hence the amount of blended light is of some concern in fitting

1.3.3 Astrometric lensing

The difficulties in determining the lens mass, distance and proper motion are clearly a major handicap in using microlensing technology to detect MACHOs, with the only observable quantity relevant to those parameters being the event timescale. Microlensing statistics can be interpreted using halo models (e.g. Gyuk and Gates 1998); however, it would clearly be preferable to determine the lens parameters independent of any models. One possible solution is the prospect of astrometric observations of microlensing events. Several authors have suggested such studies (Høg, Novikov and Polnarev 1995; Walker 1995; Miyamoto and Yoshi 1995; Boden, Shao and Van Buren 1998), which would use precise measurements of the centre of light (i.e. the point between images calculated as a image size weighted average)

during microlensing events to break the degeneracy in the event timescale. In point mass lens events the centre of light from the two images traces out an ellipse and the lens parameters can be found from the shape and size of this ellipse. During a complex (i.e. non-point) lens event the centre of light motion is less straightforward, as additional images appear and then disappear during a transit through the caustic structures. However, it has been shown (Gould and Han 2000) that such observations would allow the degeneracy between lens models to, again, be broken. Astrometric microlensing events have been simulated for both dark and bright lenses which can produce additional contributions to

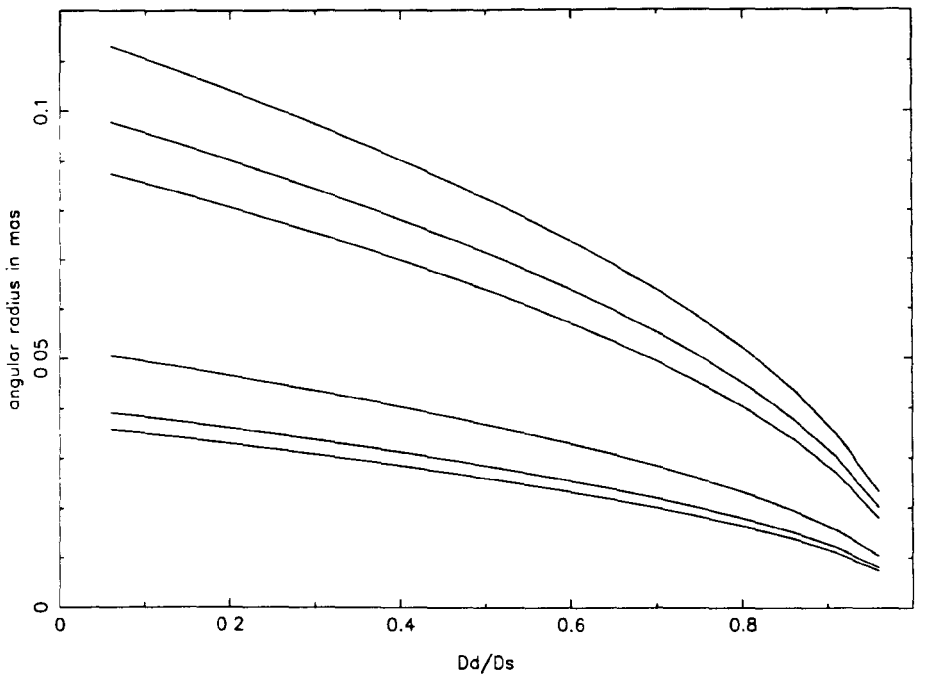

Figure 1.3: The variation of the Einstein radius in milliarcseconds of a lens of $0.1M_{\odot}$ as the ratio D_d/D_s. The curves correspond to six values of observer to lens distance D_d = 6, 8, 10, 30, 50, 60 kpc from the upper line down.

the centre of light. As the images are separated by of order a few milliarc seconds it is evident that high precision astrometry is required and so such a technique would benefit from, for example, the proposed Space Interferometry Mission [SIM] (Shao, Unwin and Boden 1997) or Global Astrometric Interferometry for Astrophysics [GAIA] (Lindegren and Perryman 1997).

1.3.4 Extended sources

The amplification function as described by Equation 1.11 breaks down in two important situations: firstly, if the impact parameter is small, i.e. $u_0 \approx 0.0$, the amplification will become very high (in fact for $u_0 = 0.0$ the amplification is formally infinite). The second situation in which the amplification function breaks down is when the source size becomes comparable to the Einstein radius of the lens. These effects occur for low mass lenses, close to the source – see Figure 1.3.

The radius of a source, in units of the Einstein radius is given by,

$$\rho = \frac{R_{source}}{\theta_0}\frac{D_d}{D_s} \tag{1.19}$$

Suppose one considers a bulge event due to a 0.3 $M_\odot$ lens, where D_d, D_s, D_{ds} are 6 kpc, 8 kpc and 2 kpc respectively giving an Einstein radius of 1.9 AU. Thus we see that late type giant stars in the galactic bulge could, indeed, have radii comparable with the Einstein radius of the lens. A 10 $R_\odot$ source would have a projected radius of $\rho = 0.02$ AER, and so an impact parameter $u_o \leq 0.02$ would imply that the lens *transits* the source.

In extended source situations it becomes necessary to calculate the amplification as an integral over the source, so the total flux $F_\nu(t)$ is given by

$$F_\nu = \int\int_{source} I_\nu(r,\theta)A(r,\theta,t)r\,\mathrm{d}r\,\mathrm{d}\theta \tag{1.20}$$

where (r,θ) are the radial coordinates in the source plane for an element of the stellar surface. As this integral contains $I_\nu(r,\theta)$ a microlensing lightcurve from an extended source event will contain information about the source surface brightness profile.

This new amplification function implies that for a source larger than about 3 AER the amplification will never reach the 1.34 threshold value. For a circular source of uniform brightness the amplification at $u_0 = 0.0$ is given by

$$A = \frac{\sqrt{\rho^2+4}}{\rho}. \tag{1.21}$$

This reduces the sensitivity of any survey to low mass lenses – which have smaller Einstein radii – typically setting a lower boundary of 10^{-7} $M_\odot$.

In recent years several authors have discussed extended source events in galactic microlensing situations. Gould (1994) considered the effects of a lens transiting the "face" of a star; such an event would allow measurement of the proper motion of the lens and thus for events towards the Magellanic Clouds would provide a means for distinguishing between self lensing in the Magellanic Clouds and MACHOs in the Milky Way's halo, as these populations would have different proper motions. By considering the magnification of an

extended source with a constant surface brightness profile, Witt and Mao (1994) demonstrated that there would be a significant variation from a point source lightcurve when the impact parameter becomes comparable to the source size. Also in 1994, Nemiroff and Wickramasinghe discussed the ability to recover the source size and then, the lens velocity; this would allow the mass of the microlens to be accurately determined. Loeb and Sasselov (1995) suggested the use of narrow-band photometry to determine the proper motion and Einstein radius of the lens, as they anticipated chromatic effects. Witt (1995) also anticipated chromatic effects and suggested that limb darkening may be detected. It was also calculated in this paper that 3% of galactic microlensing should show some effects due to stellar size. Gould and Welch (1996) considered lightcurve fitting to giant stars with limb darkening. Peng (1997) also determined the source radius from simulated data with limb darkening. These authors demonstrated that extended sources need to be considered carefully as they can provide well constrained events. Such events, however, can also yield information about the source star. Work considering recovery of information about the source includes; Simmons et al. (1995 a, b) and Newsam (1998) where the effects of limb polarisation, when differentially amplified across source, allow excellent fits to stellar radius, as the polarisation signal dominates close the to the limb. Gould (1997) suggests that microlensing lightcurves could be used to determine the rotation speed of red giants. Heyrovský and Loeb (1997) consider a uniform elliptical source, demonstrating that microlensing lightcurves can provide information about the shape of a source. Gaudi and Gould (1998), Hendry et al. (1998), Sasselov (1997) and Valls-Gabaud (1998) all considered extracting limb darkening and hence stellar atmosphere information from microlensing lightcurves. In particular, Valls-Gabaud (1998) considered the prospects for spectroscopic studies of microlensing events, allowing astronomers to study the depths at which spectral lines form in a stellar atmosphere. Extended source microlensing lightcurves produce chromatic effects as different photometric colour bands "see" a star of differing radius, due to the effects of limb darkening. These effects provide an unambiguous microlensing signature. These studies have been extended by use of more complex atmosphere models, such as in Heyrovský, Sasselov and Loeb (2000), which consider a particular red giant atmosphere model in great detail and in Heyrovský and Sasselov (2000) and Han et al. (2000) which consider non-radial surface brightness profiles (spots). Diagnosing motion in circumstellar envelopes using spectroscopic data

from microlensing events was discussed by Ignace and Hendry (1999) . Much of this work is reviewed in Gould (2001) and Sackett (2001) and also, work on the extra-galactic microlensing of extended sources such as quasars and, more recently, gamma ray bursters, is becoming applicable to this area of study.

1.3.5 Complex lenses

So far we have only considered point mass lenses; however, the presence of other types of microlens has been revealed by the existence of the lightcurves they produce. In particular, the effects of binary microlenses have been considered in great detail. Binary microlenses are of interest for two reasons: firstly, to study the lens system itself and secondly, the high amplification events that can arise due to the presence of extended caustic structures. In the point mass lens situation a "point caustic" occurs at impact parameter $u_0 = 0.0$; in complex lens situations caustics form closed structures, comprised of curved lines, folds, joined by typically three or four cusps. Caustics are the loci of points at which the amplification is formally infinite, corresponding to a new pair of images forming or disappearing

The amplification is not, in practice infinite, as it is suppressed by the finite nature of the source. Thus it becomes necessary to treat every source in the vicinity of a caustic (or cusp) as an extended source. Detailed examinations of binary systems were made by Chang and Refsdal (1979, 1984) and Schneider and Weiss (1986), with the motivation of studying binary lens situations in quasar microlensing . Of course, these treatments are now applicable to a galactic microlensing situation.

The shape and the size of the caustics formed by a binary lens depends on the separation of the lenses and the fraction of the total mass in each lens. In binary microlensing events we must consider an additional three parameters and redefine the three parameters used to express a point mass lens lightcurve. The impact parameter, u_0, is now defined as the separation between the source and the centre of mass of the binary, this occurs at time t_0. We calculate the "combined" Einstein ring radius using the combined masses of the lenses and so the third parameter t_E is now the time taken to cross the combined Einstein ring radius. The separation of the lenses, d is required, this is calculated in units of the Einstein

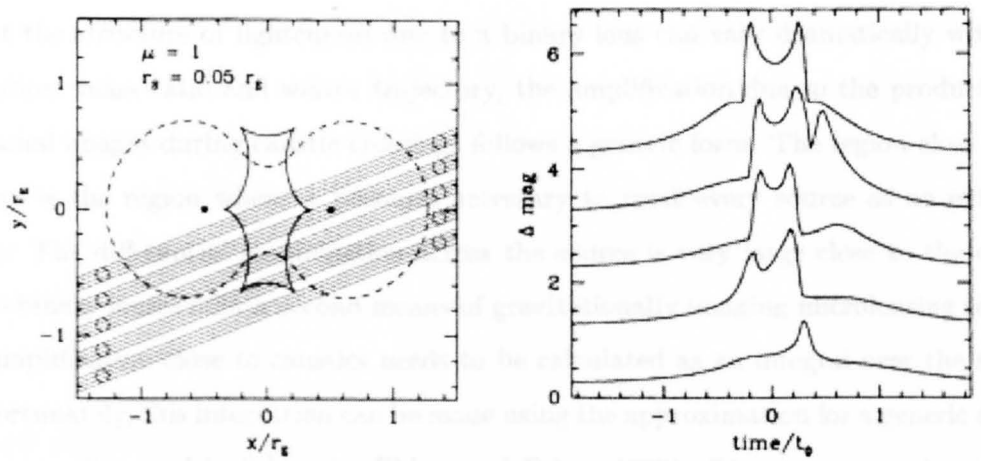

Figure 1.4: The geometry (left panel) and the resulting lightcurves(right panel) of 5 binary lens events. In the left panel the identical point masses indicated by the two points, are separated by the Einstein ring radius of the combined mass. The thick line indicates the caustic and the dashed line the critical curve. The five source trajectories are as indicated and all sources are identical and have a radius corresponding to 0.05 the combined Einstein ring radius of the lenses. The uppermost trajectory corresponds to the uppermost lightcurve – note the lightcurves are offset by one magnitude for clarity. From Paczynski (1996).

radius. We also require the mass ratio, $q = M_2/M_1$, of the lenses, where M_1 is the primary and M_2 is the secondary lens. The final parameter required describes the trajectory of the source relative to the lenses; the angle, α, is defined as the angle at which the source crosses the binary axis. The resulting lightcurves can now be calculated, but unlike the point mass lens situation there does not exist an analytic form for the amplification due to a binary lens. In order to calculate the amplification it is necessary to solve the lens equation for the correct lens parameters to find the image positions, see Dominik (1999) for a complete discussion. Further complications are introduced by the finite nature of the source, possible rotation of the lens system during the event and the effects of blending.

Despite these difficulties binary lens events have been detected with great success, indeed such events account for about 5% of the total number of microlensing events identified so far. It is worth emphasising that, whilst binary lenses are clearly different from point mass lens events due to the presence of additional peaks in the amplification producing asymmetric lightcurves, a source caustic (or cusp) crossing is not a pre-requisite for such an event and is simply the most extreme feature that may be produced by such a lens. If, however, a source does cross a caustic, it will cross a second time as caustics always form closed structures, and so producing a distinctive U-shaped lightcurve.

Whilst the structure of lightcurves due to a binary lens can vary dramatically with lens separation, mass ratio and source trajectory, the amplification due to the production of additional images during caustic crossings follows a generic form. The region close to the caustics is the region where it becomes necessary to treat every source as an extended source. The differential amplification across the source is very large close to the caustic and so binary lenses offer a second means of gravitationally imaging microlensing sources. The amplification close to caustics needs to be calculated as an integral over the source, but, fortunately, this integration can be made using the approximation for a generic caustic crossing as discussed in Schneider Ehlers and Falco (1992). This approximation takes a form such as

$$A(x) = A_0 + \frac{b_0}{\sqrt{x}}, \tag{1.22}$$

where A_0 is the magnification of the other images, which we assume to be constant during the caustic crossing. b_0 describes the form of the caustic and we can use a value of 1. The distance from the source to the caustic is given by x and is normalised to the combined Einstein radius. For negative values of x, i.e. outside the caustic structure, there are no amplification changes, as there are no additional images so $A(x) = A_0$. This approximation is only valid within a few source radii of the caustic, which is happily the region of the lightcurve sensitive to the source surface brightness profile. Furthermore, this approximation is not valid within a few source radii of a cusp and it also assumes the curvature of the caustics is very small. Use of this approximation has allowed modelling of source resolution (see e.g. Gaudi and Gould 1999) and has been applied to the analysis of several events to determine the source surface brightness profiles (see the following Section). Rhie and Bennett (2001) also investigated the feasibility of measuring limb darkening parameters from fold caustic crossings.

1.4 Results from microlensing

Over 500 microlensing events have been recorded so far, the majority of these events being classic point-source-point-lens events towards the galactic bulge (Alcock et al., 2000; Lasserre et al., 2000; Udalski et al., 2000). There are several events that are worthy of discussion here as the results they have provided are applicable to much of the information

conveyed by the body of this thesis. In particular many of the binary events discussed in Albrow et al. (1999a) are of great interest. Each event is discussed in turn, with the best fitting lens parameters being found; in some cases there are, however, multiple solutions due to degeneracy in the lens equations, see Dominik (1999). For several of these events there was intensive follow-up monitoring of the event in progress, often the caustics are well sampled, it is this type of follow-up observation that will allow stellar atmospheres to be studied by microlensing .

The first microlensing detection of an extended source was made by Alcock et al. (1997) using the point mass event MACHO 95–BLG–30, so called as it was the 30^{th} event detected towards the galactic bulge in the observing season 1995. The source was a M4 giant ($R \sim 60R_{\odot}$), although limb darkening parameters were included in the lightcurve fitting procedure they did not convincingly improve the fit. Despite the lack of limb darkening measurements this event was an early and tantalising indication of the ability of transit events to examine stellar atmospheres.

There has been considerably more success in determining limb darkening parameters, using observations from binary lens lightcurves. This is possibly due to observing limitations. It is difficult to "alert" a point mass lens transit before the event actually starts to transit, in contrast caustic crossing are considerably more observationally friendly. Typically there is a large and sudden rise in amplification (which is certainly very hard to alert). However, the amplification then decreases as the source moves away from the caustic, producing the lowest segment of the U-shaped lightcurve, this allows preparation of a period of intensive observing to be made as source the exits the caustic.

The event MACHO 97–BLG–28 provided a much more convincing limb darkening measurement. Albrow et al. (1999) found the source to be a K2 giant. This event was found to be a cusp crossing, which is actually very unlikely, in comparison to a fold caustic crossing. The event was intensively monitored by the PLANET collaboration immediately after being alerted. As the PLANET collaboration monitors from several sites it was possible for them to continue intensive observations throughout the duration of the event. The observations were of excellent photometric quality and made in two colour bands, V and I. This allowed a two parameter limb darkening model to be fitted to the lightcurves.

The limb darkening coefficients found were in agreement with the relevant models in van Hamme (1993) and Dias-Cordovas, Claret and Giménez (1995).

Intensive observations were also made during the event MACHO 98–SMC–1(Afonso et al. 2000). It was hoped that binary events could be used to determine the lens population, and the lens responsible for MACHO 98–SMC–1 was found to be within the Small Magellanic Cloud. Observations were made in the V, R and I colour bands allowed a one parameter limb darkening law to be fitted. As the source was a metal-poor A dwarf it was not possible to compare these coefficients to those computed for a suitable model.

One parameter limb darkening measurements have been made for two other stars using microlensing. The event MACHO 97–BLG–41 was an extremely complicated caustic crossing: the source met two sets of crossings. The event itself is of great interest as rotation of the binary lens system was detected, however the caustic crossings were not well enough sampled to provide a more confident limb darkening measurement. Analysies of the event OGLE 99–BUL–23 allowed one parameter limb darkening in the V and$I$ bands to be found (Albrow 2001). This work also included a treatment of the errors in determining the limb darkening parameters due to uncertainties in the lens model.

Until recently spectroscopic observations of microlensing events have not been of great success, see eg Alcock et al. (1997) and Lennon et al. (1996). The high magnification during event MACHO 97–BLG–45 allowed the lithium abundance of the source star to be found (Minniti et al. 1998). The event EROS BLG–2000–5 was, however, resolved spectroscopically. Spectra taken from the VLT (Albrow et al. 2001) and Keck (Castro et al. 2001) telescopes, showed that the equivalent width of $H\alpha$ varied across the source. The equivalent width was larger as the hotter (more central) parts of the photosphere were transiting the observation. At the time of writing it is clear that further analysis of this event will provide more information on the source photospheres.

Chapter 2

Microlensing and stellar atmospheres

Extended source effects in microlensing are valuable; however, they are also rare, so in order for the monitoring of these events to be successful to any degree it is necessary to have a clear motivation, such as recovering the source size and/or limb darkening parameters, and also to know whether this is observationally achievable within the timescale of an event. In this Chapter, two classes of extended source events will be considered: firstly, low-impact-parameter-point-mass-lens events and secondly fold caustic crossing events.

2.1 Introduction

It is the high gradient of magnification across the source during an extended source event that allows, in principle, the source to be resolved. This means that a careful treatment of the astrophysics of the source is needed in order calculate the lensed flux, as discussed in Section 1.3.4. As the source size relative to the Einstein radius of the lens can be estimated from lightcurve fitting, and the linear source size can be estimated from a dereddened colour magnitude diagram, such events allow a useful means of determining the Einstein radius of the lens for point mass lens events.This in turn allows (or at least partially allows) the degeneracy between the event parameters to be broken.

Extended source events can be modelled for a uniform disk, i.e. where the surface brightness profile is taken to be constant over the source. However, if one is to introduce a varying surface brightness profile, due to, e.g. limb darkening, as will be considered in this Chapter, this has a significant effect on the microlensing lightcurves.

One of the most distinctive observational consequences is the presence of a chromatic signature; i.e. the lightcurves will be slightly different in different colour bands. This signature arises because the radius of the source star is effectively a function of wavelength, due to the presence of limb darkening. Thus, during a transit, or close to transit, event the lens will *see* a source star of different radius in different colour bands.

Lightcurve fitting would predict different source radii in different colour bands, with longer wavebands predicting larger sources than shorter wavebands. Thus, if one were to neglect chromatic effects in parameter fitting to a real extended source event, then different timescales and impact parameters would, in principle, be fitted in different colour bands.

This chromatic difference would not be entirely alarming as it could be viewed, in fact, as a unique microlensing signature. For example, Valls-Gabaud (1998) argues that this chromatic effect provides a useful means for discriminating microlensing events from intrinsic stellar variability.

Of interest in this work, however, is how these chromatic extended source effects can be used to explore and constrain the surface brightness profile of the source.

As point mass lens transits and caustic crossing type events typically take place over just a few hours, it is vital to know how much information can realistically be extracted from the microlensing data, and in particular, what is the most effective way of observing the event in order to achieve this.

2.2 Traditional limb darkening models

Computations of stellar surface brightness profiles have been carried out for several decades – most usually in the case of modelling eclipsing binary lightcurves. These calculations

were based on an approximated treatment where the Planck function was used to compute central intensities, I_0, for different wavebands and the intensity I_μ, as a function of the (cosine of the) emergent angle, μ, was then given by a simple linear model, i.e.,

$$I(\mu) = I_0 [1 - c(1 - \mu)] \tag{2.1}$$

Here the coefficient c is dependent on the source temperature, gravity and chemical composition and the wavelength of observation.

This linear limb darkening law can be improved upon by the introduction of a two parameter model, such as the "square root" limb darkening law, given by,

$$I(\mu) = I_0 [1 - c_1(1 - \mu) - c_2(1 - \sqrt{\mu})] \tag{2.2}$$

where c_1 and c_2 depend on the source parameters and wavelength. Another two parameter limb darkening law commonly used in binary lightcurve synthesis is a "logarithmic" law, ie,

$$I(\mu) = I_0 [1 - c_1(1 - \mu) - c_2 \mu \ln \mu] \tag{2.3}$$

These limb darkening coefficients have been calculated for a range of stellar effective temperatures and surface gravities by, for example, van Hamme (1993). However these models are still overly simplistic, particularly for late type stars which are anticipated to have complex extended outer atmospheres with many molecular lines.

2.3 Next Generation limb darkening

The recent "Next Generation" (NextGen) stellar atmosphere models as computed by Hauschildt and collaborators (see Hauschildt et al. 1999 a, b and Orosz and Hauschildt 2000) considerably improve the parameterised models in several respects. The calculations used to determine the surface brightness profile in the NextGen models assume spherical geometry for giant stars, rather than the usual plane-parallel treatment. The intensities are computed directly rather than assuming a Planck law. The intensity calculations themselves are based on a library of atomic and molecular lines – about 2×10^8 lines contribute to a typical giant atmosphere model.

The dramatic difference in the dependence of limb darkening on emergent angle between the traditional models and NextGen models is illustrated in Figure 2.1. This figure shows the intensity profiles for a giant star of $T_{\rm eff} = 4250$K and $\log g = 0.5$, in four Johnson colour bands: V, R, I and K. The solid curve shows the NextGen profiles, while the dashed, dash-dotted and dotted curves denote the linear, logarithmic and square root models respectively. It is immediately clear that there is a sudden and dramatic decrease in the intensity of the NextGen models as one approaches the limb of the star – i.e. at $\mu \simeq 0.2$. This feature arises from the improved modelling of molecular scattering in the outer atmosphere of the star, and is clearly an effect which one would expect to be highly relevant to the cool giant stellar atmospheres probed by extended source microlensing, but is completely absent from the other parametric models which predict significant intensity all the way to $\mu = 0$. The question then arises: is microlensing sufficiently sensitive to detect this striking limb feature in the atmospheres of extended sources, and thus to test the NextGen models against real observations?

Microlensing has, so far, had some success in determining limb darkening parameters, during caustic crossing events, as was seen in Section 1.4. In this Chapter, point mass lens events as a probe of atmosphere models will be discussed, before consideration of the prospects for discriminating between between atmosphere models using observations of caustic crossings.

2.4 Point mass lens microlensing events

One can construct a extended source microlensing lightcurve – similar to that shown in Figure 2.2 – by integrating over the source using Equation 1.20 and the amplification function in 1.11. In this first example the lightcurve is calculated for a uniform source, so, $I_\nu(r, \theta) = I_0$ and I_0 is constant.

The lightcurve illustrated in Figure 2.2 is for a source of radius, $0.1AER$ with an impact parameter, $u_0 = 0.0$. The lightcurve has been calculated for the period during which the source crosses one Einstein diameter. In Figure 2.2, τ is defined as the Einstein *radius* crossing time, i.e. the time taken for the lens to cross one angular Einstein radius. It can

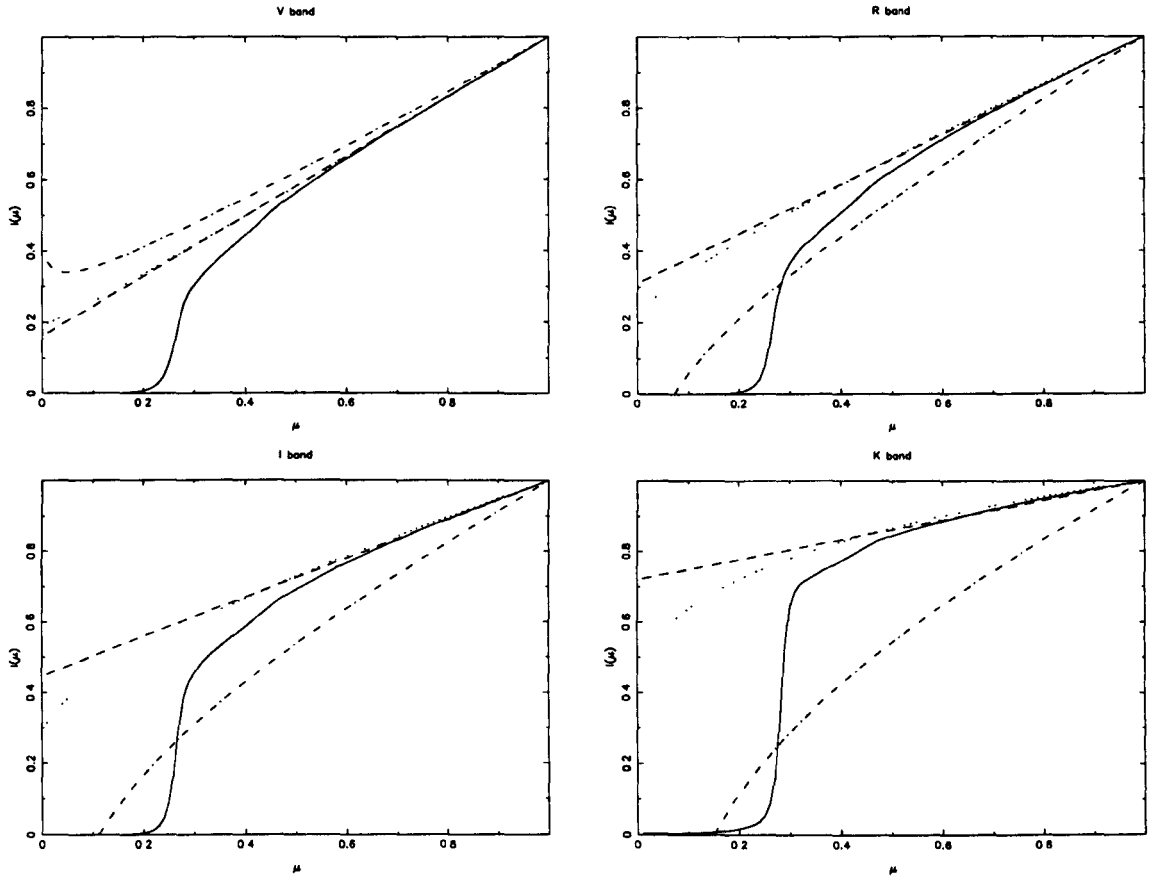

Figure 2.1: The surface brightness profiles as a function of emergent angle in V (upper left), R (upper right), I (lower left) and K (lower right) bands. The models presented are for a $T_{\rm eff} = 4250K$ with $\log g = 0.5$ star, with a NextGen model atmosphere, linear, logarithmic and square root limb darkening law represented as a continuous, dashed, dash-dotted and dotted line respectively. These profiles were calculated using the appropriate limb darkening law coefficients and data from Hauschildt et al. (1999a,b). The bands V, R, I and K correspond to 5500, 7000, 9000 and 22000 Årespectively.

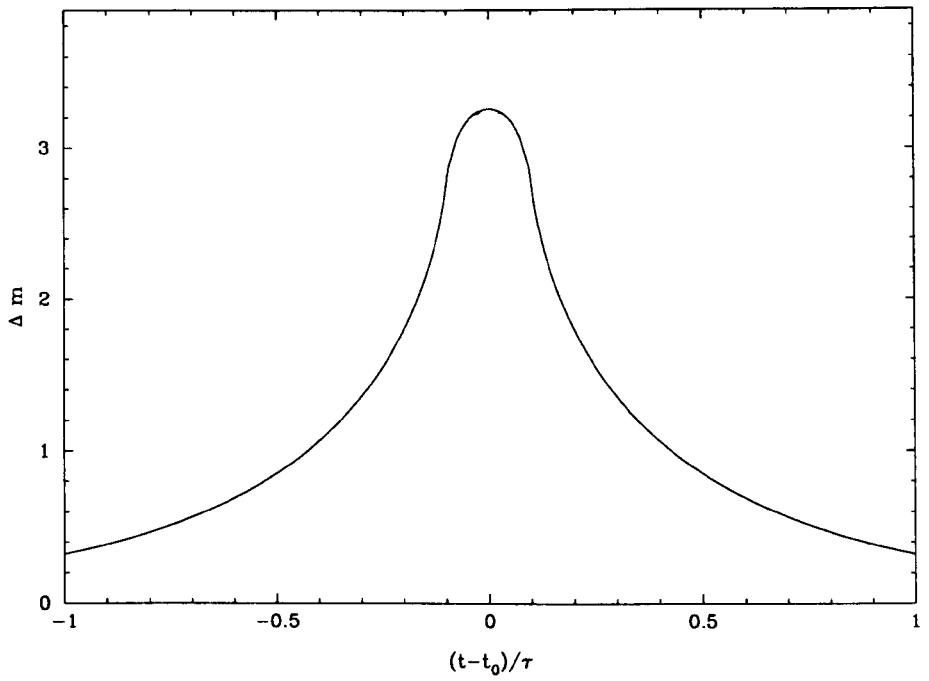

Figure 2.2: A microlensing lightcurve produced by a uniform 0.1 AER source, with impact parameter $u_0 = 0.0$.

be seen from Figure 2.2 that the main effect of comparing an extended source with a point source, is that the amplification is suppressed.

In practice, however, a uniform source model may not adequately model the lightcurves produced by a "real" microlensing source star. We can construct lightcurves in the same manner as Figure 2.2 but also incorporate a variable surface brightness, so that $I_\nu(r, \theta)$ is not constant over the source surface.

Figure 2.3 does exactly this; here a linear limb darkening law is employed, with the limb darkening coefficients from van Hamme (1993). In this case the microlensing lightcurves are now dependent on the stellar parameters of the source, since these determine the limb darkening coefficients. In Figure 2.3 we are modelling a star with effective temperature of 4000 K and $\log g = 1.0$. Recall that the surface gravity for a spherically symmetric star of mass, M and radius, R, is given by,

$$g = \frac{GM}{R^2}. \tag{2.4}$$

As was noted in Chapter 1, Alcock et al. (1997) estimated a value of $\log g = 1.0 \pm 0.2$ for the source (an M4 giant) in event MACHO–95–30.

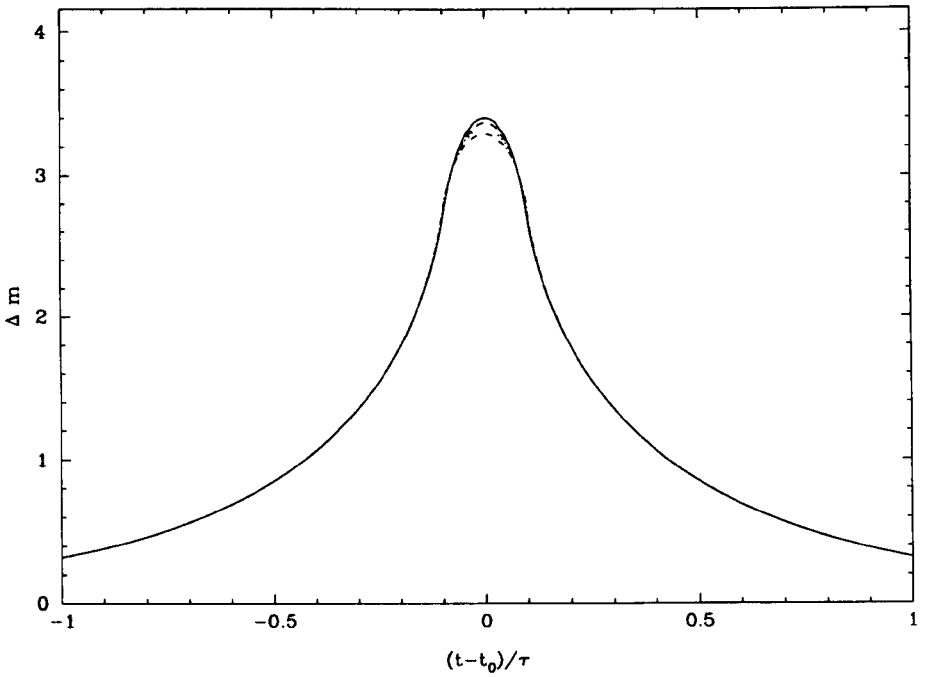

Figure 2.3: A microlensing lightcurve produced by a linearly limb darkenned 0.1 AER source, with impact parameter $u_0 = 0.0$.

Figure 2.3 shows 4 colour bands: Johnson V, R, I and K represented by continuous, dashed, dotted and dash-dotted lines, respectively. One can see the chromatic difference due to the effects of limb darkening close to minimum impact parameter. The differences between a uniform and a linear limb darkening model are highlighted in Figure 2.4.

The magnitude differences that are illustrated by Figure 2.4 indicate that such a microlensing event could be an excellent discriminant between the two models. The chromatic differences are also clear from Figure 2.4 with the most substantial changes present in the V band data. One can see large downward spikes (of ~ 0.08 magnitudes) just as the lens begins to transit the source, due to the larger flux from the limb of the source in the uniform model as compared with the limb darkened model.

This comparison can also be carried to microlensing lightcurves calculated using the NextGen stellar atmosphere models rather than the traditional parameterised limb darkening laws. As shown in Figure 2.5 the differences between these stellar atmosphere models would be clearly observable and follow a very similar pattern to those of Figure 2.4. In this case, the NextGen limb darkening has been calculated for an effective temperature of $4000K$ and $\log g = 1.0$ and for a source of radius 0.1 AER. This choosen radius is slightly

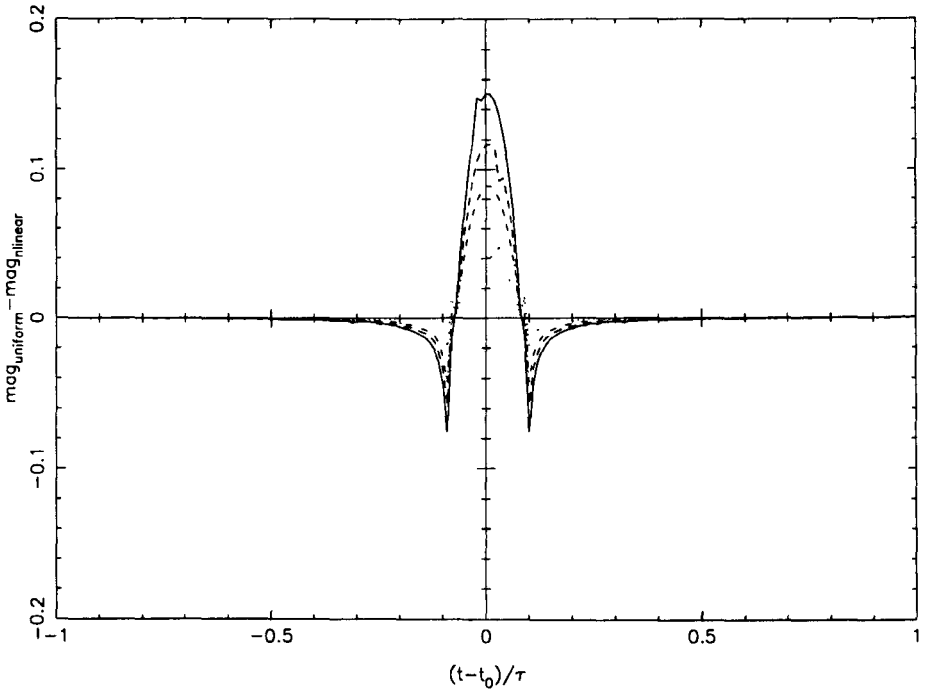

Figure 2.4: Comparison between a uniform and a linear limb darkened source as presented in the previous Figures. There is some small structure in this Figure due to the numerical tolerance of 0.001.

larger than a typical source radius of about 0.03 AER for bulge events, however, smaller sources are examined in the following Section.

To confirm that a source is exhibiting a NextGen model atmosphere rather than a traditional limb darkening law, one would hope to see significant photometric differences between the two models. A comparison between the lightcurves produced by the microlensing of a linear limb darkened and a NextGen source is shown in Figure 2.6 for identical stellar parameters of 4000K, $\log g = 1.0$ and radius 0.1 AER.

In Figure 2.6 the y-axis represents the difference in magnitudes between these two models. This is defined as

$$m_{\text{linear}} - m_{\text{nextgen}} = (-2.5\log(\frac{F_{LL}}{F_{UL}})) - (-2.5\log(\frac{F_{LN}}{F_{UN}})) \tag{2.5}$$

where F_{LL}, F_{UL}, F_{LN} and F_{UN} represent the integrated surface brightness for the case of the lensed linear limb darkening, the unlensed linear limb darkening, the lensed next generation and the unlensed NextGen fluxes respectively. This allows us to examine the differences in magnitude between the magnification of the two sources.

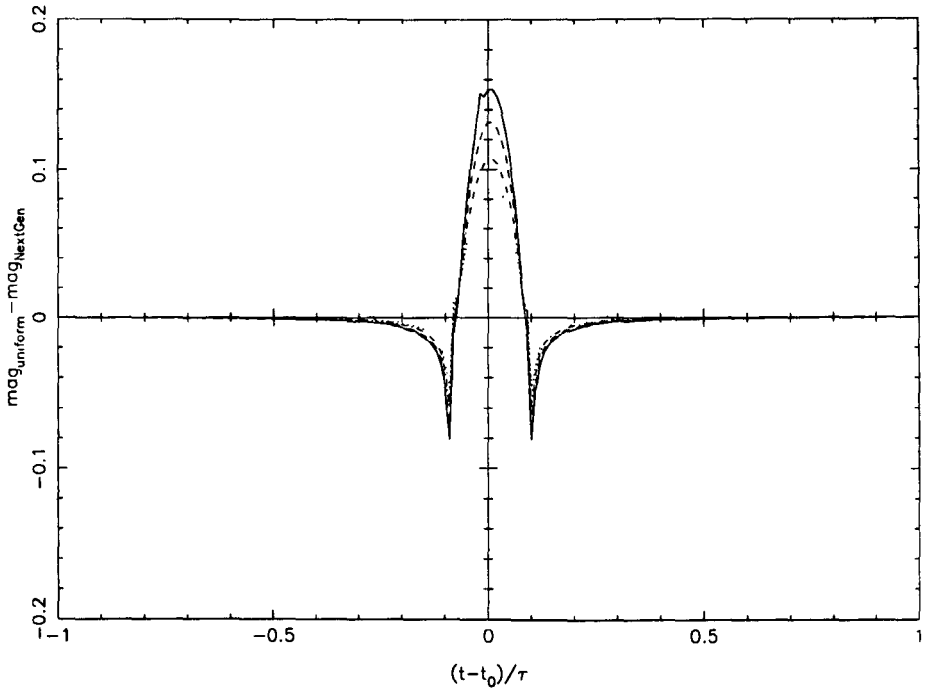

Figure 2.5: Comparison between a uniform and a NextGen limb darkened source both of T_{eff} = 4000 K, $\log g = 1.0$ $\rho = 0.1$ AER and $u_0 = 0.0$.

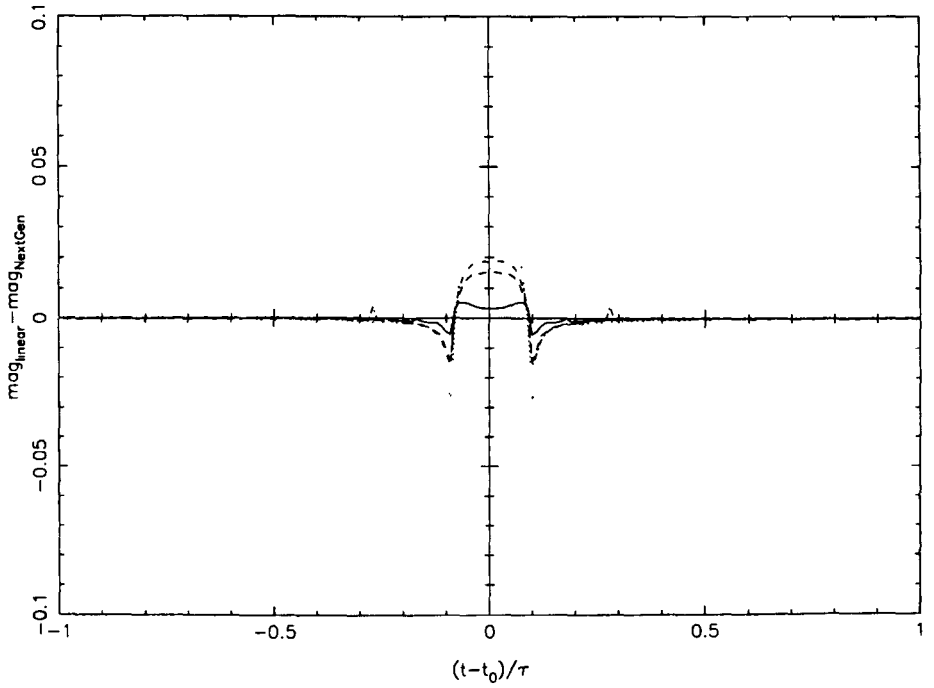

Figure 2.6: Comparison between linear and NextGen limb darkened source both of $T_{eff} = 4000$ K, $\log g = 1.0$ $\rho = 0.1$ AER and $u_0 = 0.0$.

Figure 2.6 shows that with 'good' photometric data (i.e. with typical errors of order 0.01 magnitudes) and with dense temporal coverage, a source with a NextGen atmosphere should be distinguishable from a model with a linear limb darkening law. A fit to a linear limb darkening law would be particularly poor just before and just afer the lens transits the source – there are negative "spikes" in Figure 2.6 at these points. These features occur as the NextGen model is considerably more limb darkened than the linear model, so there is a significantly larger contribution to the flux from the linear model.

The second feature is the broad peak during the actual transit – which again occurs as a consequence of the strong limb darkening of the NextGen model, which has the effect of making the source appear smaller, producing positive residuals in Figure 2.6.

The chromatic effects also change in a interesting way in Figure 2.6. We can see that it is now the longer wavelength colour bands that display the greatest differences between the models. If one considers again Figure 2.1, one can see why this is the case. The NextGen model shows a larger deviation from the parameterised limb darkening laws at longer wavelengths; this is not surprising considering the treatment of molecular opacity used in the NextGen model which dominates at longer wavelengths. This underlines the importance of multi wavelength observations in this context: for the event shown in Figure 2.6, observations in the V band only – even with excellent temporal sampling and typical magnitude errors of 0.01 – would give only a marginal detection of the presence of the NextGen atmosphere.

As a two parameter law could be more appropriate than a linear law for modelling these events, it is also important to consider whether a NextGen atmosphere would provide sufficient flux in the centre of the source as opposed to the limb, in order to distinguish it from a source with a two-parameter limb darkening law. Such a comparison is shown in Figure 2.7, presented in the same way as Figure 2.6. Again it can be seen that good photometric data could allow one to favour a NextGen atmosphere model over a square root limb darkening. Similar remarks apply to logarithmic limb darkening – again excellent data would be required, but in principle a NextGen atmosphere could be discriminated from a logarithmic limb darkened atmosphere.

From these Figures it is evident that the limb of the source must be probed by the lens

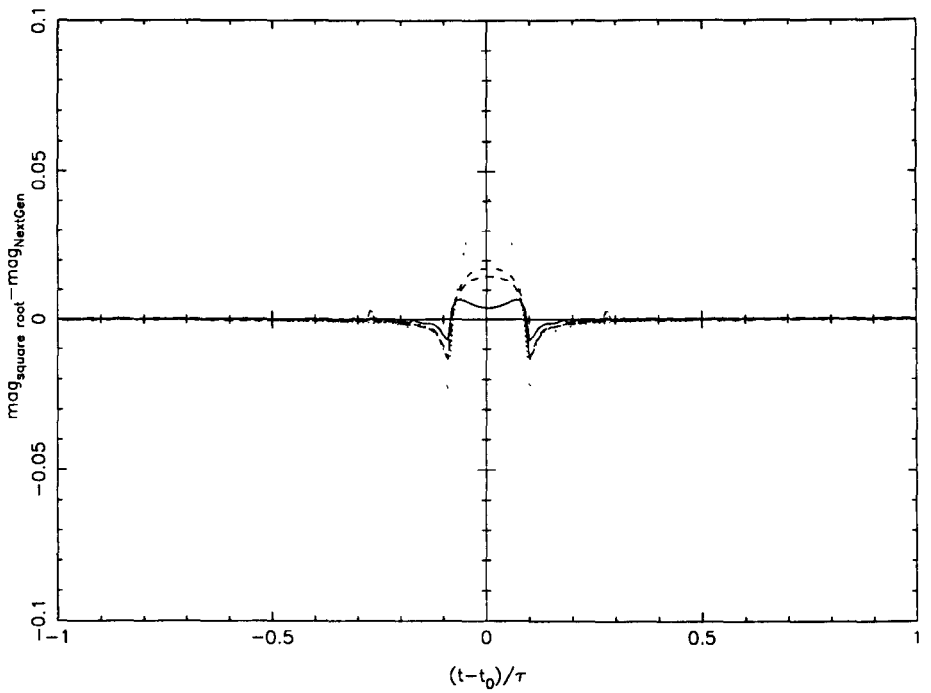

Figure 2.7: Comparison between square root and NextGen limb darkened source both of T_{eff} = 4000 K, $\log g = 1.0$ $\rho = 0.1$ AER and $u_0 = 0.0$.

for significant residuals due to the excessive limb darkening to become evident. If the lightcurve is poorly sampled during this vital region then the signature of intense limb darkening will be lost. It is the downward spikes that one would hope to resolve rather than the bump feature. This suggests that intensive photometric monitoring would be more effective than less frequent but more accurate (e.g. spectroscopic) data. We will return to this issue in Section 2.6.

The preceding figures were all for microlensing events with impact parameter, $u_0 = 0.0$. In practice, of course, transit type events (with impact parameter less than the source radius) will occur with a range of impact parameters. An event with impact parameter equal to zero will provide a significant extended source signature, as the lens passes over much more of the photosphere. However, larger impact parameters can also be considered, such as that illustrated by Figure 2.8. In this case with $u_0 = 0.08$, the lens effectively only probes the outermost parts of the photosphere, namely the heavily limb darkened region. Again, however, one can see residual "spikes" as the linear limb darkened and the NextGen models vary significantly (at least at longer wavelengths) over this region. One can also comment that the signature occurs over a smaller timescale: however, provided

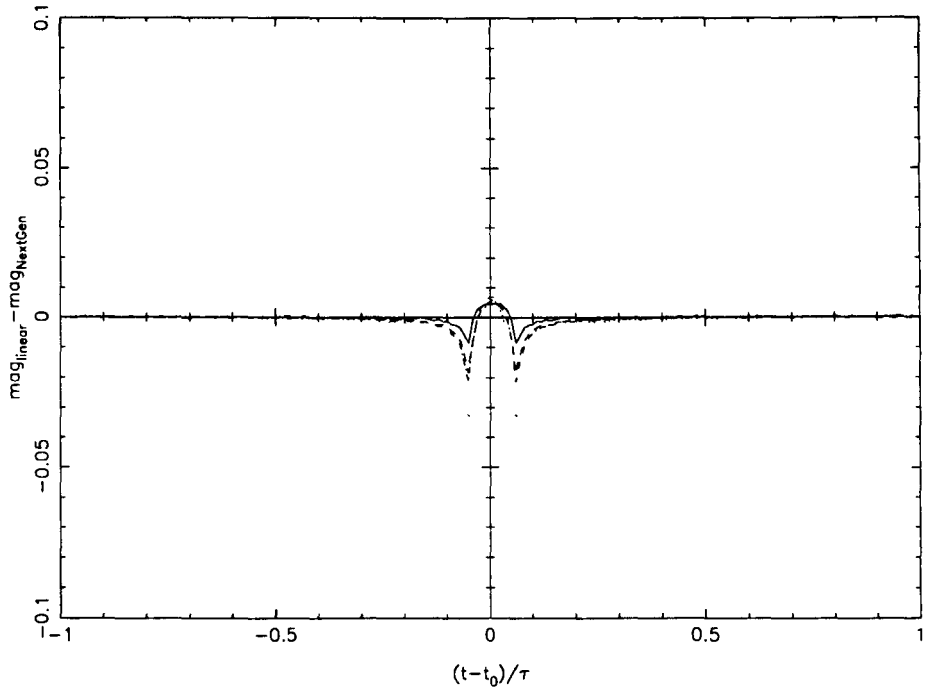

Figure 2.8: Comparison between linear and NextGen limb darkened source, both of $T_{eff} = 4000$ K, $\log g = 1.0$ $\rho = 0.1$ AER and event impact parameter, $u_0 = 0.08$

the sampling is sufficiently dense to detect the feature at all, the magnitude differences between the models should still be sufficient to indicate the presence (or otherwise) of a NextGen type atmosphere – subject again to the caveat that observations at wavelength longer than the V band would be required.

In Figures 2.9 and 2.10 slightly larger impact parameters are illustrated. In Figure 2.9 the minimum impact parameter equals the source radius. In this example, we can see one downward spike; however the magnitude changes are possibly not substantial enough to convincingly determine the limb darkening.

In Figure 2.10 the lens does not transit the source, and hence the depression produced by the differences in the atmosphere models could not be detected using current technology. Although non-transit events can provide a significant deviation from the classic microlensing point source lightcurve, at an impact parameter of approximately less than to equal to two source radii, their chromatic signature is not sensitive enough to constrain the surface brightness profile.

The potential for extended source microlensing to probe stellar atmospheres decreases with

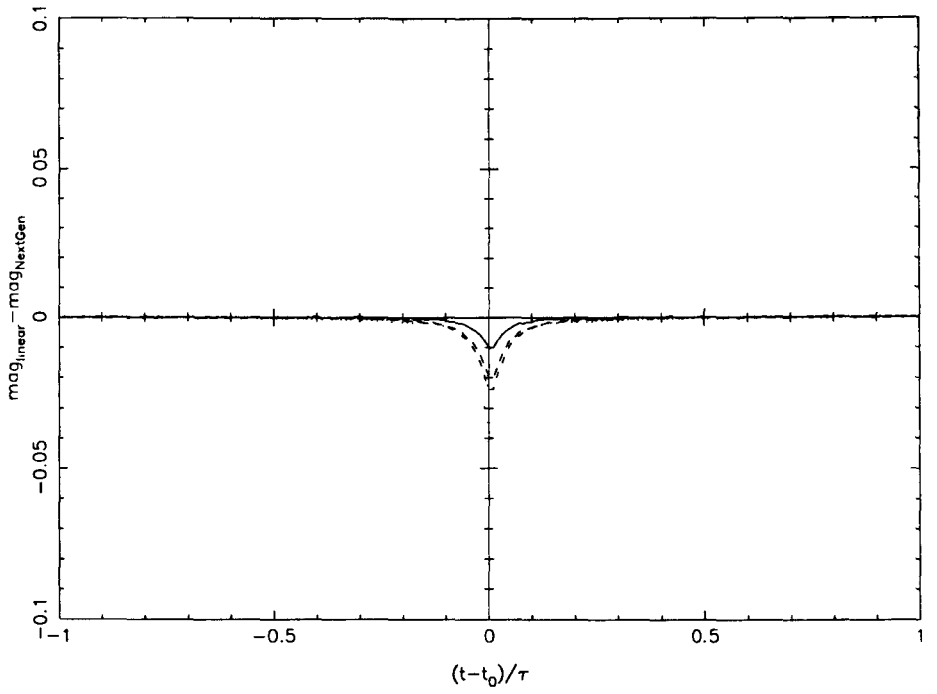

Figure 2.9: Comparison between linear and NextGen limb darkened source, both of $T_{eff} = 4000$ K, $\log g = 1.0$ $\rho = 0.1$ AER and event impact parameter, $u_0 = 0.10$

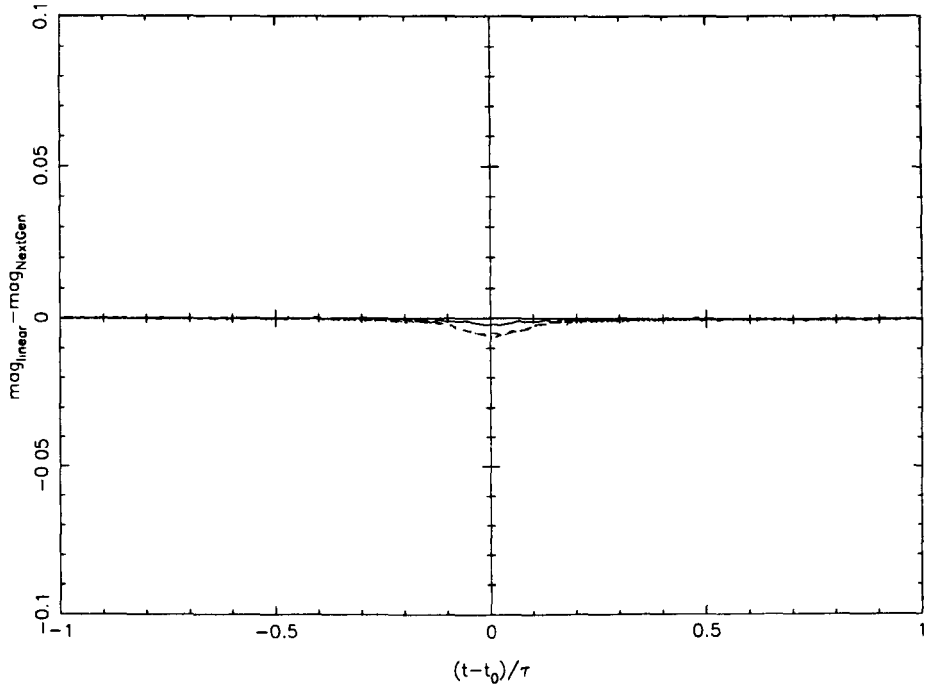

Figure 2.10: Comparison between linear and NextGen limb darkened source both of $T_{eff} = 4000$ K, $\log g = 1.0$ $\rho = 0.1$ AER and event impact parameter, $u_0 = 0.12$

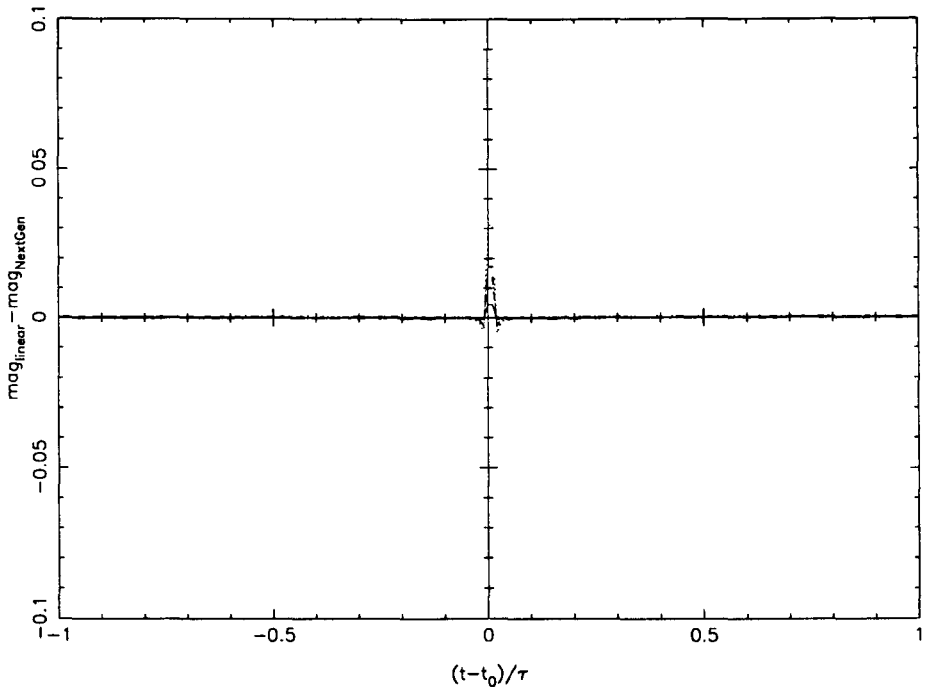

Figure 2.11: Comparison between linear and NextGen limb darkened source both of $T_{eff} = 4000$ K, $\log g = 1.0$, $u_0 = 0.0$ and for a source radius of 0.01 AER.

source radius: smaller sources are less likely to be involved in transit-type events, and the transit times themselves will be much shorter, making adequate sampling throughout the transit more difficult to achieve. Likewise the ability of even zero impact parameter microlensing events to distinguish between atmosphere models is seriously reduced because the chromatic signature is suppressed. We can see this in Figure 2.11 which shows a comparison between the lightcurves produced by a linear limb darkened and a NextGen source, presented in the usual manner. However in this example, the differences are not at all clear, due to the fact that the source being considered has a radius of $0.01AER$, rather than the radius $0.1AER$ used in the previous examples. The amplification in such an event would be higher than the amplification of a larger source, but the chromatic signature would not be higher.

Thus, for studies of stellar atmospheres one must attempt to examine microlensing events with large source radii relative to the Einstein radius. This implies that both "self lensing" type situations, (i.e. where the lens lies close to the source) and intrinsically "large" sources are required, and so it is the galactic bulge rather than the Magellanic Clouds that are most likely to produce suitable events for a study of this kind.

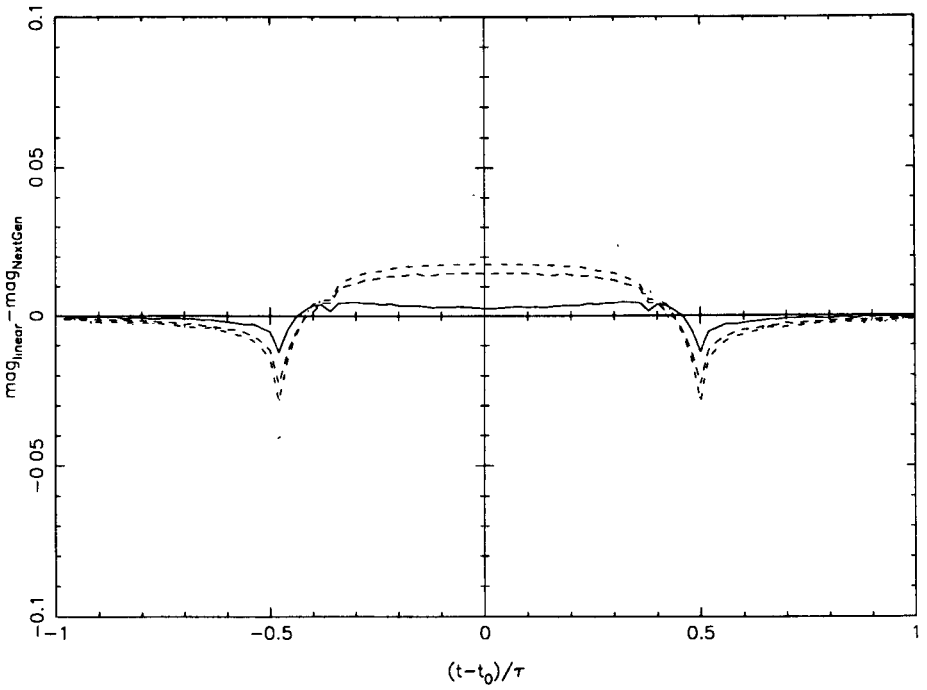

Figure 2.12: Comparison between linear and NextGen limb darkened source, both of $T_{eff} = 4000$ K, $\log g = 1.0$, $u_0 = 0.0$ and for a source radius of 0.5 AER.

The exaggerrated effects of a (possibly implausibly) large source are illustrated in the usual manner in Figure 2.12. In this example the source radius is $0.5AER$, for an impact parameter of $u_0 = 0.0$. The downward spikes are again present; however the it is the central part of the photosphere that dominates the magnitude change. In such a case the central region of the lightcurve would in fact be a better discriminant between source models rather than relying on data points around those times when the lens is probing the limbs of the star.

Whilst such "stellar tomography" can, in principle, be acheived by dense temporal sampling throughout the duration of an extended source microlensing event, the technique could be vulnerable if the event parameters are themselves poorly determined. Indeed even a small change in, for example, the stellar radius could have a significant impact on the chromatic signature.

In the previous figures we have seen that an extreme limb darkening (in our case the NextGen model) has the effect of making the source appear *smaller* relative to a linear limb darkened (or indeed a uniformly bright) source of the same radius. As extended source signatures allow determination of the lens Einstein radius, a systematic overestimation of

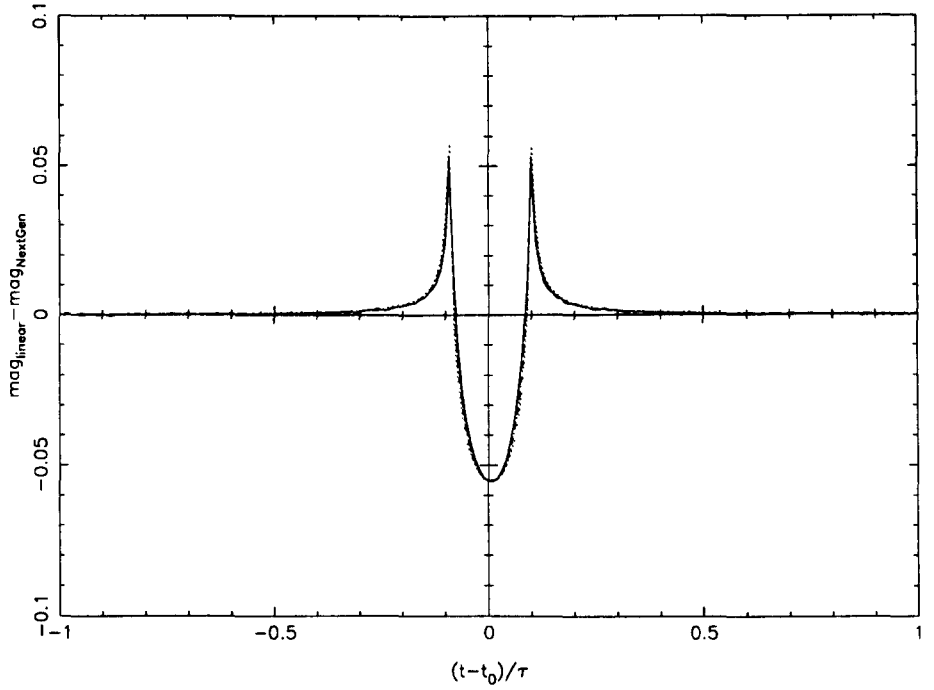

Figure 2.13: Comparison between linear 0.1 AER source and NextGen limb darkened 0.095 AER source both with $T_{eff} = 4000$ K $\log g = 1.0$ and $u_0 = 0.0$.

the Einstein radius could result if limb darkening effects were ignored, although of course, one would hope that the presence of a chromatic signature would indicate not only that a more complex model atmosphere was required but also that the source radius had been underestimated. We can now illustrate this point.

In Figure 2.13 a source with linear limb darkening is compared to a source with a NextGen atmosphere, both with minimum impact parameter equal to 0.0. However in this instance the linear limb darkened source has a slightly smaller radius of $0.095AER$, compared with the NextGen source, which has a radius of $0.1AER$.

This difference in source size is modest and so are the differences between the models. This suggests firstly that it is crucial to fit lightcurves to a fine grid of source radii, in order to find the most appropriate parameter set. Note, however, that in Figure 2.13 the spikes are now upwards, as the NextGen model (with radius equal to 0.1 AER) provides more flux at its limb than the slightly smaller linearly limb darkened source. Likewise the central bump is, in this example, downwards. This illustrates that by carefully examining the pattern of the residuals it is possible to conclude whether the stellar radius has been systematically underestimated – provided we have some prior understanding of how the

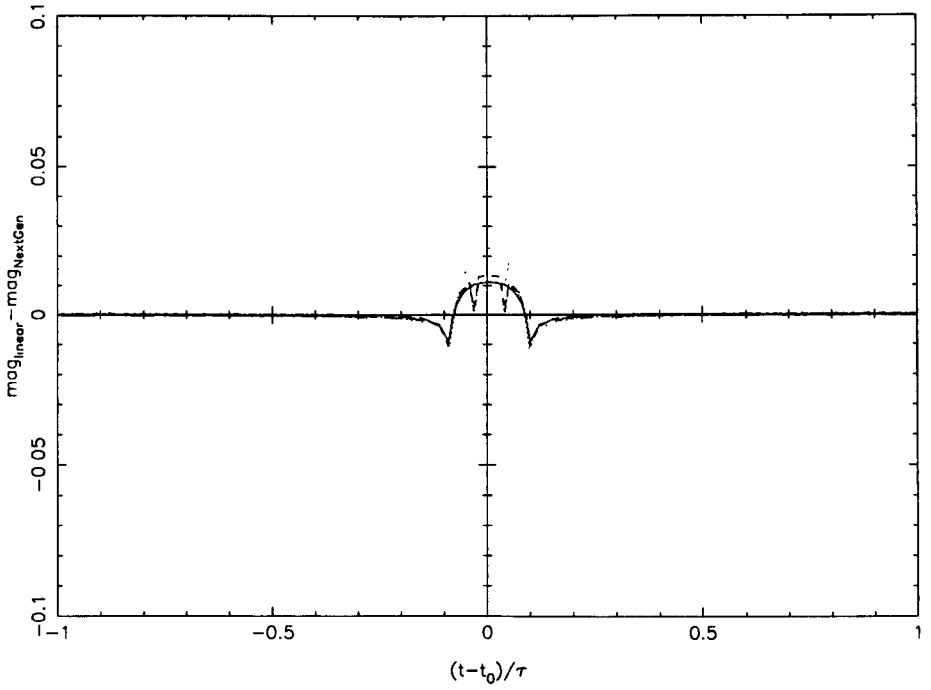

Figure 2.14: Comparison between linear and NextGen limb darkened source both with $T_{eff} = 6000K$, $\log g = 3.0$, $\rho = 0.1$ AER and $u_0 = 0.0$.

'true' stellar atmosphere model is likely to be different from e.g. the simple linear case. In other words, if our 'true' stellar atmosphere model provides less flux at the limb than the linear case, then the upward spikes in Figure 2.13 are a clear indication of a negative bias in determination of the source radius.

The NextGen model atmosphere is particularly well suited to cool giants where unsurprisingly there are large numbers of molecular lines produced, and so the surface brightness profile varies drastically from the traditional parameterised limb darkening laws. As one examines sources with higher effective temperatures and higher values of $\log g$, the differences between the models become less clear. Consequently the ability of microlensing to distinguish between atmosphere models would be reduced as one considers sources with higher effective temperatures and surface gravities.

This situation is illustrated by Figure 2.14, where sources with $T_{eff} = 6000$K and $\log g = 3.0$ are compared in the usual manner for a zero minimum impact parameter and a source radius of 0.1 AER.

The downward spikes are not significant in this plot as the limb darkening does not vary

significantly enough for microlensing to effectively distinguish a NextGen atmosphere from a linear limb darkened atmosphere in this case.

2.5 Fold caustic crossing microlensing events

As the only confident measurements of limb darkening achieved by microlensing so far have been made by observations of caustic crossing events, it is natural that we also consider them here.

The amplification produced during a fold caustic crossing using the inverse square root approximation is described by Equation 1.22. For an extended source the amplification is, again, an integral over the source function.

The case of a uniform source crossing a fold caustic is illustrated by the lightcurve in Figure 2.15. In this example the lightcurve is presented from the point where the centre of the source is 3 source radii from the fold, on the outside of the caustic structure; after undergoing a large change in amplification as the source enters the caustic, the lightcurve continues until the centre of the source is 3 source radii from the caustic. In this region the inverse square root approximation is perfectly acceptable – as long as the crossing point is far from any cusps and the source size is small in comparison with the fold curvature, since we assume that the caustic is a straight line. In Figure 2.15 the source size is $0.01AER$ and the centre of the source crosses the caustic at $(t - t_0)/\tau = 0.0$. It is only when a source element has crossed the caustic that it experiences the amplification and so the peak amplification actually occurs after the timestep at which the centre of the source coincides with the caustic. It is only the amplification from the additional images which is being considered in these examples as the other images are assumed not to alter significantly during this period.

Of course this high degree of differential amplification allows different parts of the source to be probed at different stages of the event.

Figure 2.16 presents the V, R, I and K lightcurves denoted by continuous, dashed, dotted and dash-dotted lines, respectively, from a source with $T_{eff} = 4000$ K and $\log g = 1.0$ in

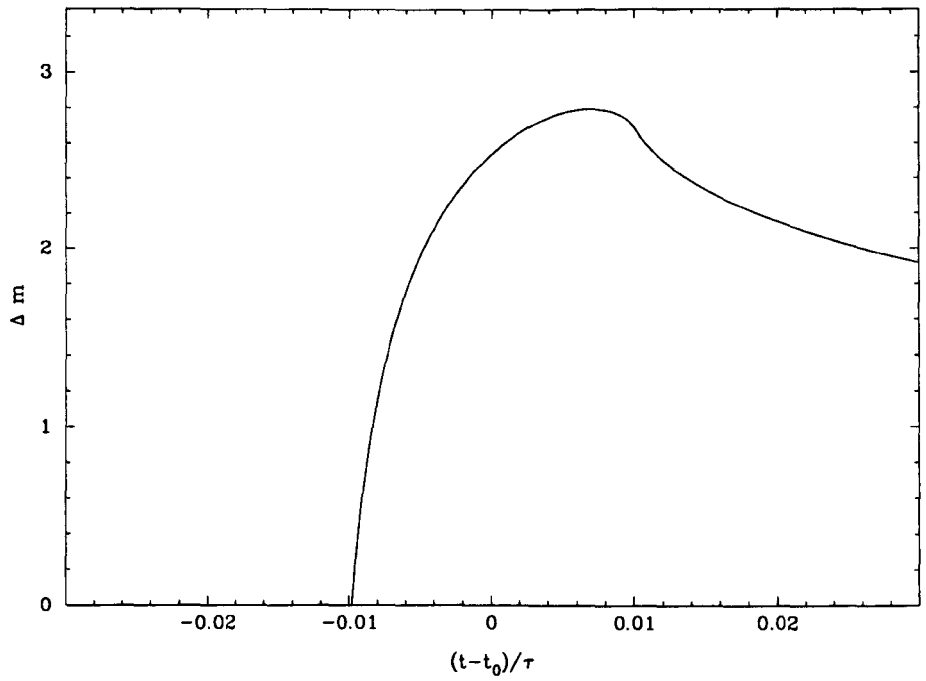

Figure 2.15: A uniform source with $\rho = 0.01$ AER undergoing a fold caustic crossing.

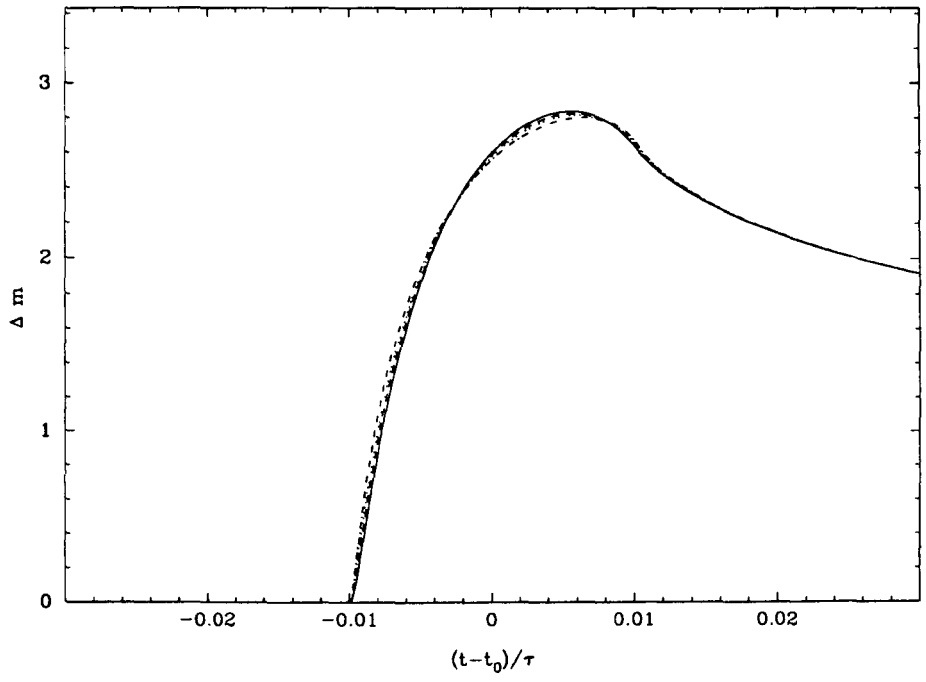

Figure 2.16: A linear limb darkened source with $\rho = 0.01$ AER, $T_{eff} = 4000K$ and $\log g = 1.0$ undergoing a fold caustic crossing.

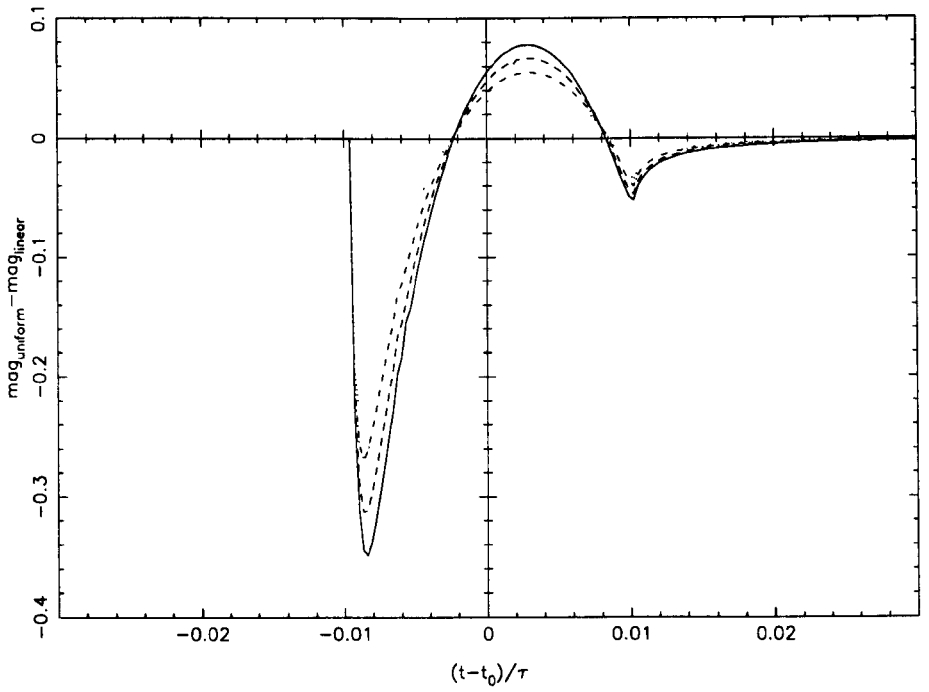

Figure 2.17: Comparison between the uniform and a linear limb darkened source described by Figures 2.15 and 2.16.

the same fashion as Figure 2.15. One can clearly see from these lightcurves that there are small chromatic effects produced by the limb darkening. These are highlighted by Figure 2.17, which is a comparison of uniform to linear limb darkening, in the same manner as the comparisons in the previous section of this Chapter. The chromatic effects are particularly large as the source begins to move into the caustic. The amplified flux in this region is dominated by the small region of the photosphere underneath the caustic – this region is subject to limb darkening, which itself is wavelength dependent. Limb darkening parameters have already been successfully determined from similar events for both one and two parameters limb darkening laws, as we have seen in Section 1.4.

We can now apply the NextGen atmosphere models to fold caustic crossing events. In Figure 2.18 we present a comparison of a NextGen atmosphere of a $T_{eff} = 4000$ K and $\log g = 1.0$ source against an otherwise identical source but with a linear limb darkening model. There is again a chromatic dip as the source enters the caustic (peaking at 0.06 magnitudes in the V band) – although it is not as substantial as the comparison with a uniform model (a 0.34 magnitude change in the V band) it is, nevertheless, certainly within current observational limits.

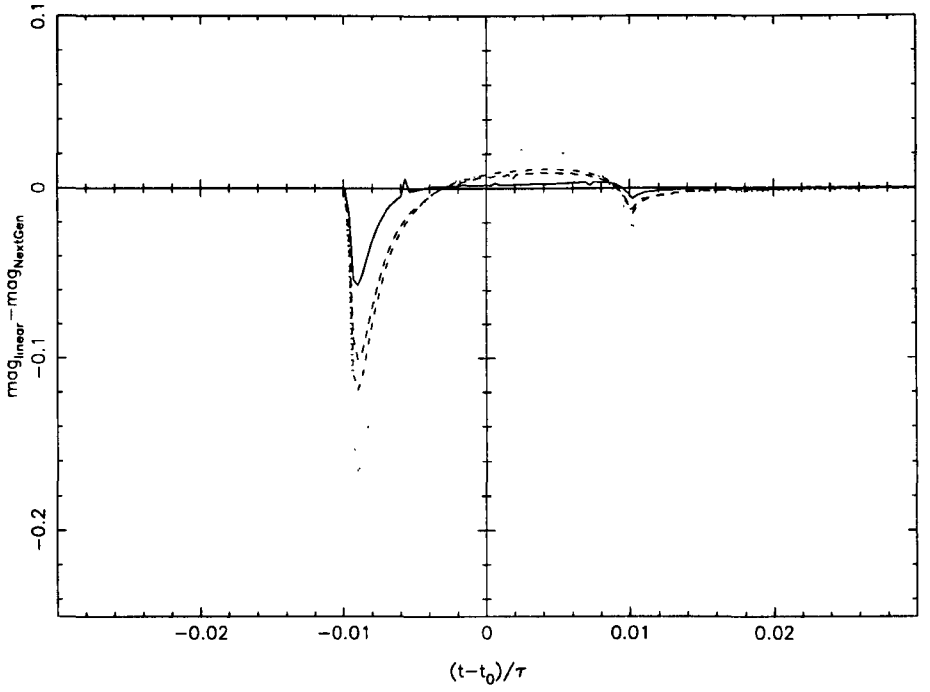

Figure 2.18: Comparison between a NextGen and a linear limb darkened source both with T_{eff} = 4000 K, $\log g = 1.0$ and $\rho = 0.01$ AER.

Of course the most effective way of monitoring caustic crossing events is when the source actually exits the caustic structure, as the first caustic crossing acts as a warning, and the second crossing is relatively easy to predict. In this case, the source would be exiting and so it would be the trailing limb (the last part of the photosphere to exit) that would provide the greatest change in flux between atmosphere models.

As with the point lens transits, the NextGen model also provides a significantly different lightcurve to two-parameter limb darkening laws. Again a substantial dip occurs when only the limb of the source is being amplified – emphasising the need for intensive sampling just after the peak of the lightcurve, as a source is exiting the caustic.

It has been noted in recent analyses of caustic crossing events (Albrow et al. 1999) that without accurate determination of the lens parameters – i.e. the mass ratio, lens separation, the combined Einstein radius and the trajectory of the source itself – determining the source parameters can be hazardous as they may correlate with the lens model. If the lens parameters are used to deduce the source atmosphere model, then uncertainty in the lens model will introduce errors in the atmosphere model. Conversely, as was discussed above, an incorrect atmosphere model may lead to biased determination of the event parameters.

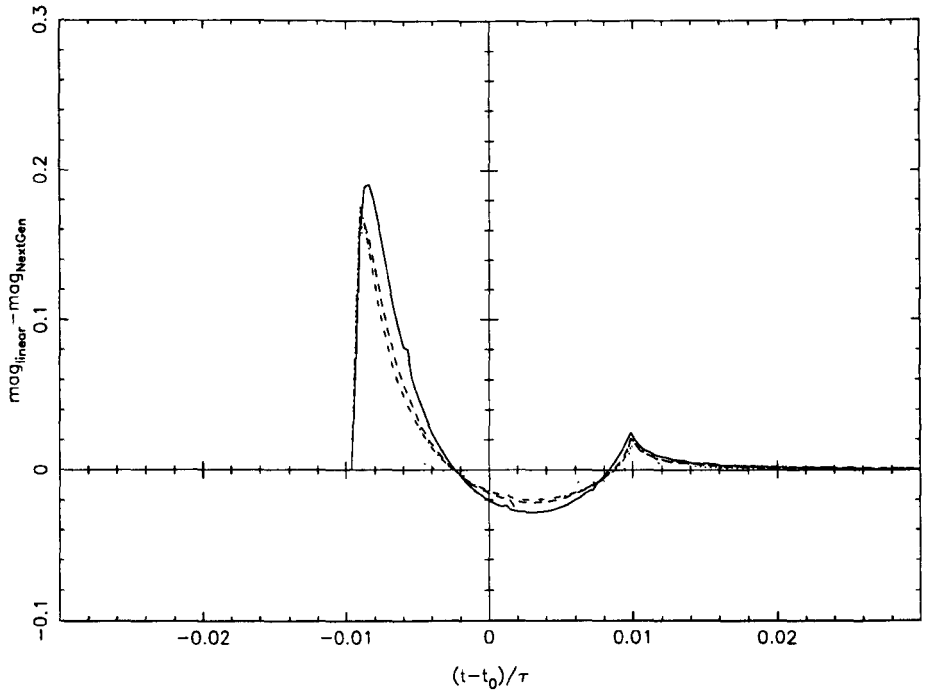

Figure 2.19: Comparison between linear 0.01 AER and NextGen limb darkened source with 0.0095 AER.

In Figure 2.19 a comparison is made between a slightly smaller – in this case 0.0095 AER – linearly limb darkened source and a NextGen atmosphere source (of radius 0.01 AER) in a similar manner to Figure 2.13. Again, careful examination of the residuals can provide additional information on the possible presence of bias in the event parameters induced by the use of an incorrect stellar atmosphere model – given some prior understanding of the expected size, location and sign of the residuals. For example, the excess flux at the "wing" of the caustic crossing lightcurves shown in Figure 2.19 may indicate that the source is actually subject to stronger limb darkening than the linear model, but is slightly larger than the best fit linear model radius would suggest.

As with Figure 2.14, the NextGen model does not vary enough at higher effective temperature and for higher surface gravities, to be obviously distinguishable from a linearly limb darkened source. This fact is illustrated by Figure 2.20, for a source of $T_{eff} = 6000$ K and $\log g = 3.0$.

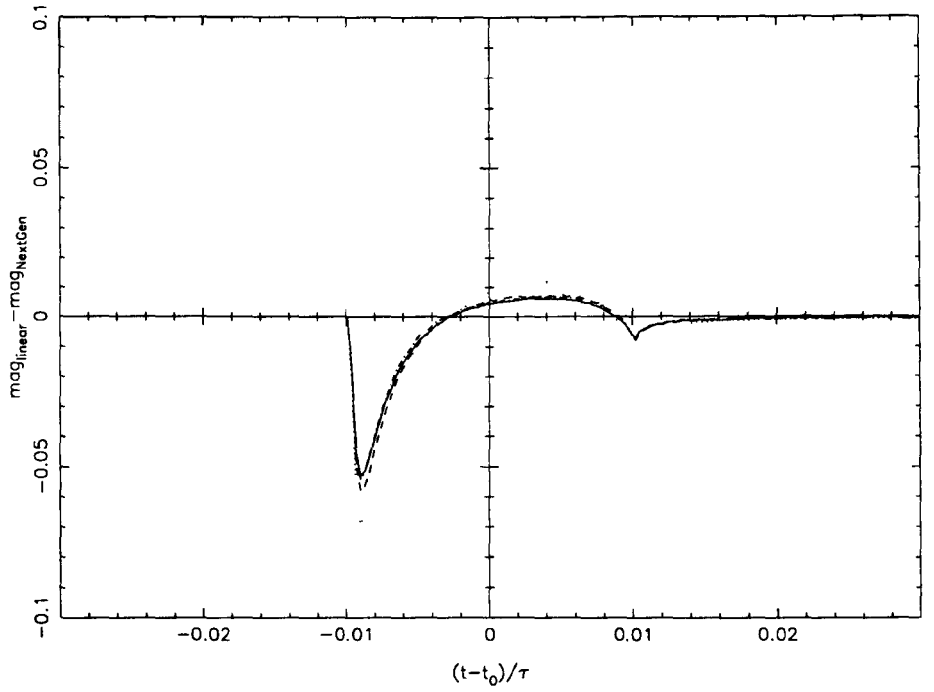

Figure 2.20: Comparison between linear and NextGen limb darkened source both with T_{eff} = 6000 K and $\log g = 3.0$

2.6 Applying the Backus Gilbert method

Whilst, we have shown that microlensing lightcurves due to a source with a NextGen atmosphere can produce appreciable magnitude changes when compared with traditional parameterised limb darkening laws, it would also be of interest to demonstrate that microlensing could be used to discriminate between surface brightness profiles in a model independent way. We will apply a well known inverse problem technique, the Backus Gilbert method, to allow us to invert a series of microlensing lightcurves, so that we can explore how well varying sampling strategies allow us to recover the surface brightness profile of a source. In Coleman (1998) and Hendry et al. (1998) the Backus Gilbert method was applied to analyse the impact of smoothing kernels on the reconstruction of source surface brightness profiles from microlensing lightcurves. In these treatments only linear limb darkening laws were considered [1]. Here we apply the existing Backus Gilbert machinery to examine the reconstruction of the NextGen atmosphere models.

[1]Note that the Backus Gilbert method itself allows a model independent determination of the variance of a reconstruction, but this variance does depend on the noise on the data itself – which of course will be related to the model in some way.

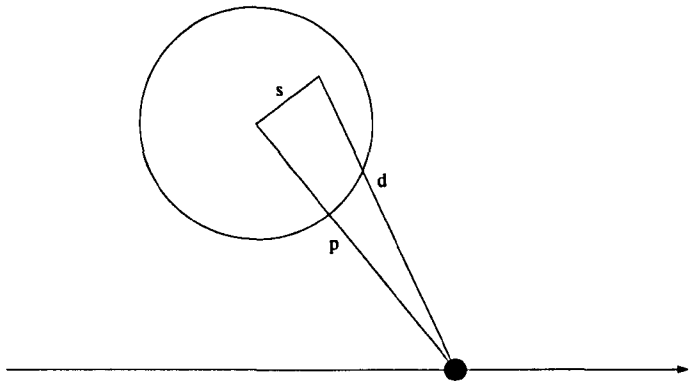

Figure 2.21: Source and lens geometry as used in Backus Gilbert method. The source is shown as the large unfilled circle and the lens as the small filled circle; clearly this diagram is not to scale.

2.6.1 The Backus Gilbert method

First we briefly summarise the mathematical details of the Backus Gilbert method, before applying it to our simulated data. We follow closely the treatment and notation given in Coleman (1998). The geometry of the lensing event is shown in Figure 2.21. As we have seen previously the observed microlensing lightcurves are given by an integral equation. This means that the relationship between lightcurve data, g, and the surface brightness profile, f, can be written as

$$Kf = g \tag{2.6}$$

where the integral operator, K, has a smoothing effect. The Backus Gilbert method allows recovery of the source function, $f(s)$, over the disk of the star; this can only be measured through the data, $G(p)$, which is itself an integral of the source function – just as in the situation we are considering here.

$$G(p) = \int_0^{R_*} f(s)K(s;p)\,\mathrm{d}s, \tag{2.7}$$

where the kernel, $K(s;p)$, is the integral of the lens amplification over angle, for a ring at fixed radius s, and can be calculated and R_* is the source radius. So a set of N observations, i.e. $g_i \equiv G(p_i)$, can be written as

$$g_i = \int_0^{R_*} f(s)K_i(s)\,\mathrm{d}s + n_i \tag{2.8}$$

where $K_i(s) \equiv K(s;p_i)$ and n_i is noise. With these assumptions it is possible to calculate the estimator $\hat{f}(s)$. The Backus Gilbert method assumes that the true source function is

related to the mean of its estimator by

$$E(\hat{f}(s)) = \int_0^{R_*} \Delta(s, s\prime) f(s\prime)\, \mathrm{d}s\prime \tag{2.9}$$

where $\Delta(s, s\prime)$ is known as the averaging kernel. We define the estimator through a set of response kernels, $q_i(s)$, as

$$\hat{f}(s) = \sum_i q_i(s) g_i \tag{2.10}$$

Using Equation 2.8 and assuming the weighted noise has zero mean, i.e. $E(\sum_i q_i(s) n_i) = 0$, the averaging kernel becomes

$$\Delta(s, s\prime) = \sum_i q_i(s) K_i(s\prime) \tag{2.11}$$

We can then measure the width of $\Delta(s, s\prime)$ using

$$A \equiv \int_0^{R_*} (s - s\prime)^2 [\Delta(s, s\prime)]^2\, \mathrm{d}s\prime = \sum_{ij} q_i(s) W_{ij}(s) q_j(s) = q(s)^T W(s) q(s) \tag{2.12}$$

where $W_{ij} \equiv \int_0^{R_*} (s\prime - s)^2 K_i(s\prime) K_j(s\prime)\, \mathrm{d}s\prime$ and $q(s) = (q_1(s), ..., q_N(s))^T$. Again assuming the weighted noise has zero mean, the variance of $\hat{f}$ is

$$B = var\hat{f}(s) = q(s)^T S q(s) \tag{2.13}$$

where we have defined the noise covariance matrix as $S_{ij} \equiv E(n_i n_j)$. Taking the n_i to be independent and with a Gaussian standard deviation, σ then $S_{ij} = \delta_{ij}\sigma^2$.

Essentially we wish to minimise the dependence of $\hat{f}(s)$ on the underlying function and the noise. However, we cannot do both simultaneously. By increasing the width of $\Delta(s, s\prime)$ we smooth the recovered value, making it less sensitive to the noise, but we do also need to maintain adequate resolution if we are to identify features in the source surface brightness profile such as the strong limb feature in the NextGen model. We therefore need to strike a careful balance between the competing needs of resolution and stability.

The Backus Gilbert method addresses this problem by finding the "response kernels",$q_i(s)$, which minimise $A + \lambda B$, – where λ is known as the smoothing parameter – and subject to the constraint that $G.R = 1$, where $R = [R_1, ..., R_N]^T$ and $R_i = \int_0^{R_*} K_i(s)\mathrm{d}s$. Thus, by careful choice of smoothing parameter we can control the 'trade-off' between resolution and stability. The optimal response kernels have analytic solution

$$q_\lambda(s) = \frac{[W(s) + \lambda S]^{-1}.R}{R[W(s) + \lambda S]^{-1}.R}. \tag{2.14}$$

Then using Equation 2.10 we can obtain $\hat{f}_\lambda(s)$.

Numerical experiments (see e.g. Gray 2001) show that a smoothing parameter of order unity is the most suitable choice. Although we are free to adopt a different smoothing parameter for each value of s, in the following section for simplicity we adopt $\lambda = 1$ throughout.

2.6.2 Recovered surface brightness profiles

In this Section, we compare the recovered surface brightness profiles from an identical source but using differently sampled observations. We do this in an attempt to convey the most effective observational strategies for recovering surface brightness profiles in a realistic way. Three temporal sampling strategies are considered and we also consider the effects of reduced photometric accuracy that could well be the result of an intensive sampling strategy. The recovery is only presented using V band data.

In Figure 2.22 we illustrate the sampling strategies. The modelled event, from which the recovery is made, uses a NextGen atmosphere. In this situation the 4000 K, $\log g = 1.0$, $\rho = 0.1$ AER source is being lensed with impact parameter $u_0 = 0.0$. The small circles represent the most densely sampled data, which uses 85 points and particularly dense sampling during the portion of the lightcurve that crosses the stellar limb. The larger squares and triangles represent two less dense sampling strategies; the 'square' data is more favourable as it includes 2 extra observations during the vital transit.

In Figures 2.23, 2.24, 2.25, 2.26 and 2.27 the recovery via the Backus Gilbert method for our chosen sampling strategies and NextGen source is presented. In these Figures $I(s)/I_0$ is the intensity at distance, s, from the centre of the source normalised by the central intensity. The solid line indicates the surface brightness profile of a NextGen source, i.e. the correct atmosphere model for the simulated data. The dotted, dashed and dash-dotted lines indicate the linear, logarithmic and square root limb darkening laws for a source of the correct effective temperature and surface gravity. The recovery and its errors (calculated as the square root of the variance as given by Equation 2.13) are indicated by the filled circles with error bars. The recovery is shown for 100 equally spaced values of

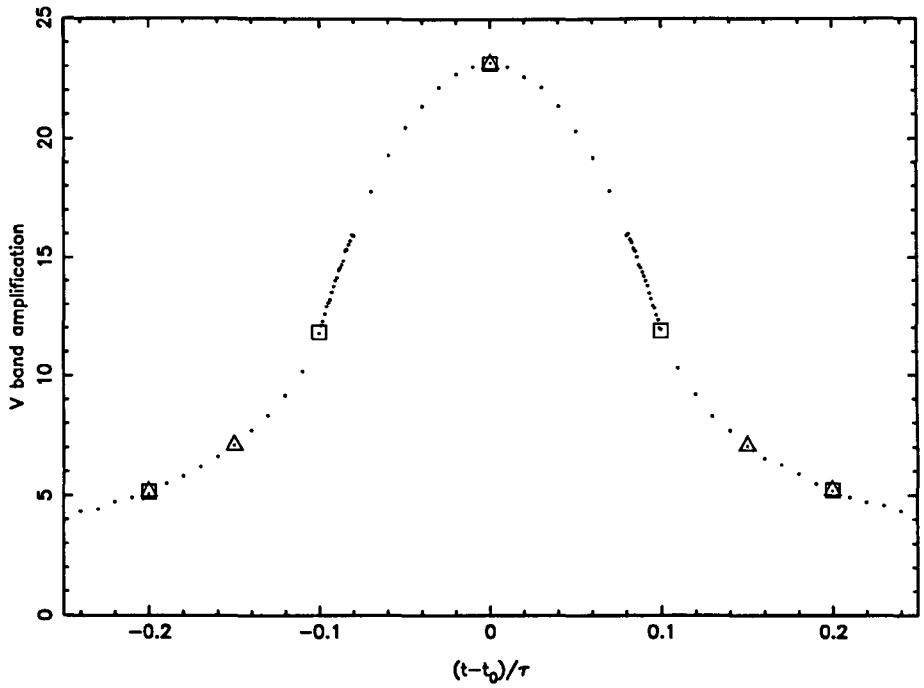

Figure 2.22: V band lightcurve of a microlensing event, being observed with three strategies, as indicated by the circles, squares and triangles. The 4000 K, $\log g = 1.0$, $\rho = 0.1$ AER source is being lensed with impact parameter $u_0 = 0.0$.

s, normalised by the stellar radius.

Figure 2.23 shows the reconstruction for the "triangle" sampling strategy with photometric errors assumed to be 2% of the unlensed V band flux. We can see that the recovered solution gives a poor reconstruction of the source surface brightness profile, and certainly would not allow us to distinguish between the surface brightness models. This is unsurprising considering that there is only one observation during the vital transit stage of the lightcurve, so clearly the resolution of recovery is severely limited by the lack of information in the microlensing lightcurve. Note that the formal error on the recovery as given by Equation 2.13 varies with s; this reflects the non-trivial interplay between the spacing of the observations and the smoothing action of the microlensing kernel across the stellar disk, and it does not necessarily follow at positions directly below the lens. Similar remarks apply to the following reconstructions.

Figure 2.24 shows the reconstruction for the "square" sampling strategy, again with 2% flux errors. There are now 3 observations during the transit: a central observation and one on both limbs. This allows a greatly improved recovery of the surface brightness

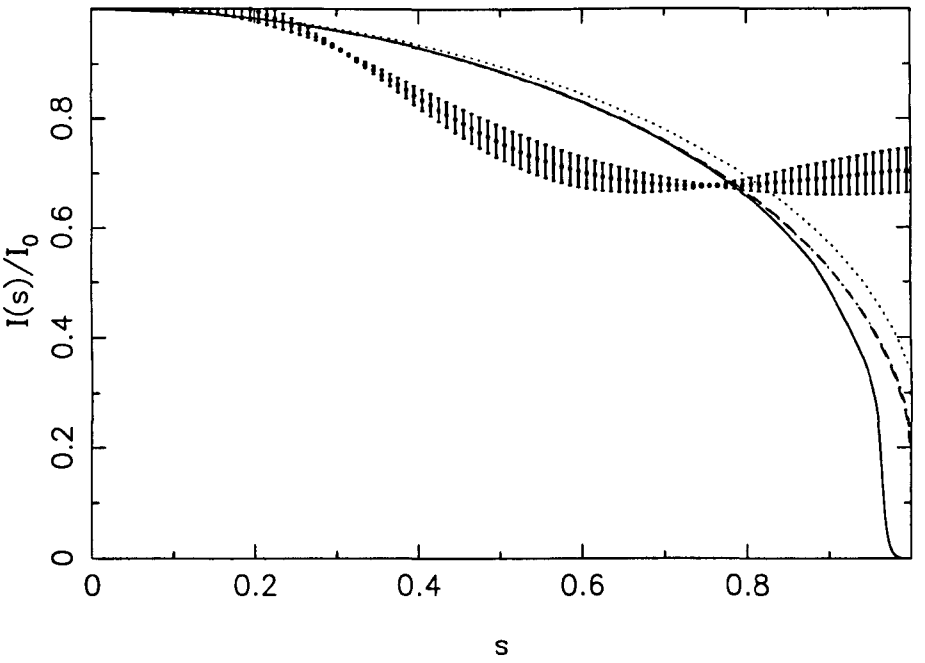

Figure 2.23: The recovery of a surface brightness using the data points indicated by the triangles in Figure 2.22.

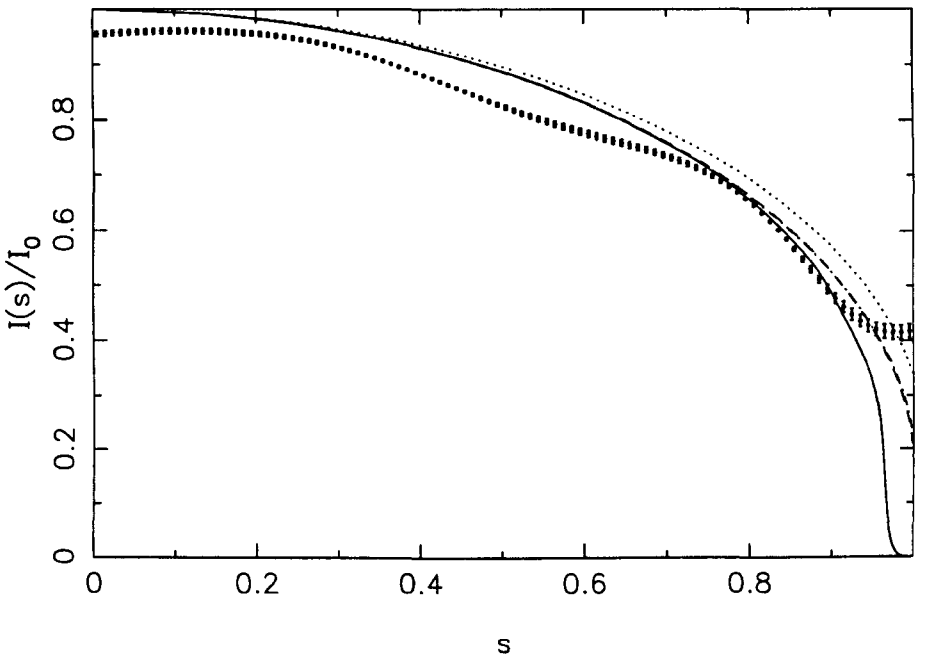

Figure 2.24: The recovery of a surface brightness using the data points indicated by the squares in Figure 2.22.

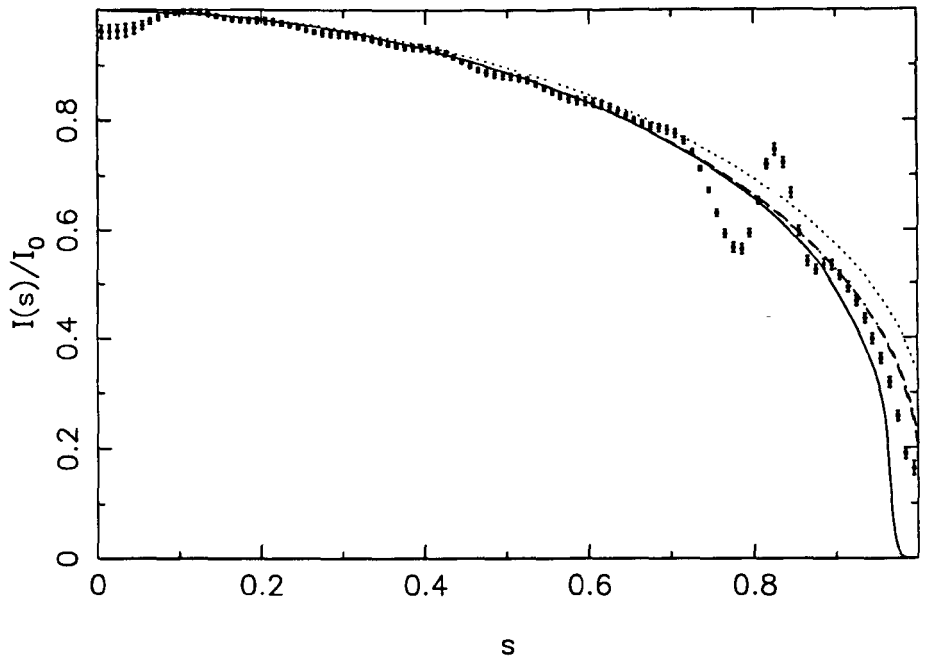

Figure 2.25: The recovery of a surface brightness using the data points indicated by the circles in Figure 2.22, with 2% errors on the unlensed flux.

profile as compared with Figure 2.23, despite the fact that each recovery was produced using the same photometric error. Note that the smoothing properties of the microlensing kernel result in a small but significant bias for $s < 0.7$ (remember that we are making no assumptions in our reconstruction about the form of the surface brightness profile, so there is nothing other than the observed data to "force" the solution to agree with a particular profile). However, for $0.7 < s < 0.9$ the recovered surface brightness profile shows excellent agreement with the NextGen model, with very small formal errors, and in particular appears able to discriminate the NextGen model from the traditional limb darkening models. It is interesting to note that the Backus Gilbert recovery is "best" during the region where the models begin to deviate. The recovery, however, becomes biased for $s > 0.9$ due to the lack of information in this region resulting from the smoothing.

In Figure 2.25 we can see the effect on increasing the number of observations, using the "small circle" strategy, but with the same photometric error of 2%. The additional observations allow an improved recovery of the surface brightness profile in the region $s > 0.9$, and again it is seen that the traditional models are not well fitted by the recovery. There is, however, an oscillation in the recovery at about $s \sim 0.8$. This feature may be a result of a non-optimal choice of smoothing parameter over this region, since for

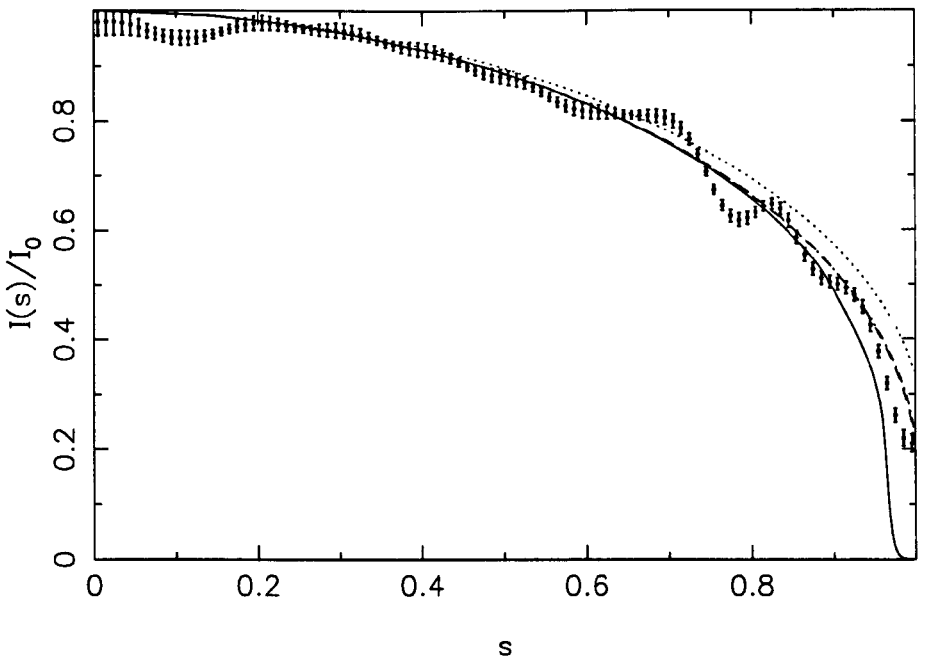

Figure 2.26: The recovery of a surface brightness using the data points indicated by the circles in Figure 2.22, with 5% errors on the unlensed flux.

expediency we have adopted the same value of the smoothing parameter for all values of s. If the smoothing parameter is too small then the recovery will have high resolution but may only be resolving features in the noise. One way to address this might be to e.g. constrain the derivatives of the recovery which would have the effect of damping out oscillatory solutions. This approach is adopted in e.g. regularisation methods of solving inverse problems Craig & Brown (1986) but we do not attempt such a treatment here.

Figure 2.26 again shows the "small circle" sampling strategy recovery, but where the photometric error has been increased to 5%. Despite this increase, it is important to note that the recovery of the surface brightness profile would still allow discrimination between source atmosphere models. The oscillatory feature is less pronounced in this case, which may indicate that the solution with $\lambda = 1$ is more heavily smoothed than in the case with 2% flux errors.

In Figure 2.27 we again see the recovery from the "small circle" sampling strategy, but now with a comparatively poor photometric error of 10% of the unlensed flux. Interestingly, despite these larger error values, the recovered profile is still broadly similar to that of Figure 2.26, and whilst it would be difficult to say that the NextGen model is favoured in

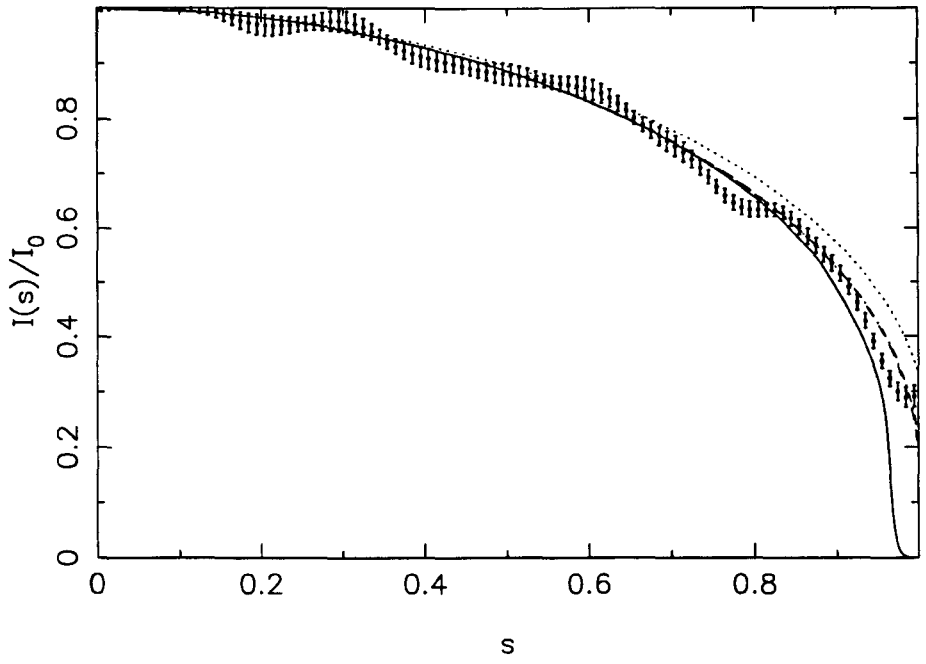

Figure 2.27: The recovery of a surface brightness using the data points indicated by the circles in Figure 2.22, with 10% errors on the unlensed flux.

the outer portion of the source photosphere, the linear limb darkening law could certainly be ruled out. This result reconfirms that dense sampling, even at the expense of photometric precison, will allow better determination of the source model than sparsely sampled but accurate observations. The feature that we are hoping to image is of course the large reduction of flux towards the stellar limb due to the improved atmosphere model; to image this it is vital that observations are made as the source transits the feature. It is, however, difficult to predict when the source limb will be crossed in order to make observations at that instant, so it is greatly reassuring that poor but densely sampled data would be able to image a source with similar resolution to a small number of accurate and serendipitous observations.

Chapter 3

Imaging stellar photospheres in point mass lens events

If microlensing can distinguish between radial surface brightness profiles, i.e. differing stellar atmosphere models, can it then be used to indicate the presence or otherwise of non-radial surface brightness features, as might be produced by the presence of spots? The possibility for 'gravitational imaging' of star spots is becoming increasingly tantalising with improving follow-up observing capabilities.

In this Chapter the microlensing signatures of star spots are presented for the point lens case, followed by discussion on the detectability of these features for varying source, lens and spot parameters. Also considered are some of the complications arising in modelling microlensing spot signatures; it will be demonstrated that these complications may prevent a complete set of spot parameters being extracted from a particular microlensing event.

3.1 Background

The potential for 2–d imaging of stellar photospheres was highlighted by Heyrovský and Sasselov (2000), who initially considered the prospects for detecting stellar spots by microlensing . Imaging photospheres by other methods is only possible for particular populations of star. Imaging is currently possible by three techniques. Firstly there is direct imaging, which is of course possible for the Sun and more recently has been carried out in the optical for e.g. α Orionis using HST (Gilliland and Dupree 1996). Indirect imaging is possible from either Doppler Imaging or, more straightforwardly, observations of photometric modulation (see e.g. Strassmeier and Linsky 1996 for details). However these techniques are still limited to suitable candidate stars, in particular with regard to their rotation periods, spectral type and intrinsic brightness and (in the case of Doppler Imaging at least) are strongly model dependent.

Clearly, therefore, there is a wide range of stellar spectral classes for which we know only a very little of their surface brightness activity, through current observational techniques. Evidence, or otherwise, of the presence of star spots can place valuable constraints on theoretical models of stellar surface activity. For example,the semi-regular variability of α Orionis has been attributed to intermittent appearance of convection cells on the photosphere. The brightness changes detected have been of the order of one-half magnitude over a timescale of years. Whilst the HST observations of Gilliland and Dupree revealed a bright area on the photosphere, later spectroscopic observations suggested that it was due to "an outwardly propagating shock wave" rather than convection – Uitenbroek, Dupree and Gilliland (1998). Of course, α Orionis is a very close supergiant (hence the opportunity for direct imaging) and may in any case not be indicative of the general population of late type star.

Using microlensing to study stellar surface activity is particularly attractive for several important reasons. Imaging via microlensing can be used to study more distant sources than the other techniques, as well as being able, at least in principle, to probe any population of stars.

Microlensing provides an increased flux, making it easier to study the source as a whole.

But it is the high gradient of magnification over the source during transit events that can be used to image any star spots. High amplification microlensing events are already intensively monitored with the motivation of detecting extra-solar planets. As the microlensing technique has already been successful in constraining stellar limb darkening, which is manifested by a radial surface brightness profile, it seems a natural progression to establish whether microlensing could also be applied in constraining non radial surface brightness profiles.

The transit portion of a microlensing event takes place over a short timescale, so intensive monitoring during the transit periods is a prerequisite to image the source. This approach has the advantage that the source can be imaged quickly without extensive use of expensive resources. However it must also be taken into account exactly how much information can be provided by the transit and the best means of extracting this information. As will be shown in this Chapter, modelling the microlensing signatures which one might expect to find from reasonable star spot models can lead to useful conclusions on the best observing strategies for detecting and identifying the star spots themselves.

Another motivation for the study of star spot imaging by microlensing is the concern that star spots may mimic planetary microlensing signatures. The distinctive spikes produced by planetary caustics may be smeared out by the finite nature of the source (Vermaak 2000). This effect not only suppresses the planetary signature but also has the effect of producing a bump or depression in the lightcurve that is close in appearance to a star spot signature. The time of the feature, i.e. whether it occurs during the transit portion of the lightcurve or not, and the chromatic nature of the signature should provide a suitable means of discriminating between star spots and planets. Detecting star spots could, in fact, be an exciting 'by product' of planetary microlensing search, because the observational strategies and resources required are very similar – as shown in this Chapter.

3.2 Applying microlensing

To calculate the microlensing lightcurves produced by spotted sources it is necessary to integrate the amplification over the stellar disk. Recall that for an unspotted source this

is given by

$$f = \int_{s=0}^{R} \int_{\theta=0}^{2\pi} I_*(s,\theta) A(d) s \, \mathrm{d}s \, \mathrm{d}\theta \tag{3.1}$$

where the source angular radius, R, and the angular separation, d, are measured in units of the angular Einstein radius. For the background unspotted source the surface brightness profile is taken to be radially symmetric, i.e., $I_*(s,\theta) = I_*(s)$. The values of $I_*(s)$ can then be found from the stellar atmosphere model for the effective temperature and $\log g$ of the source being modelled.

Inclusion of star spots essentially means that the surface temperature and hence surface brightness is now a function of the polar angle, θ, on the projected disk. It is then possible to evaluate the contribution from a spot as

$$\Delta F = \int_{\mathcal{A}} \left[I_{\mathrm{sp}}(s,\theta) - I_*(s) \right] A(d) \, s \, ds d\theta \tag{3.2}$$

where $\mathcal{A}$ is the projected area of the disk covered by the spot. The correct model for the surface brightness of the spot then needs to be found, incorporating limb darkening if appropriate. Additional star spots can also be modelled by adding up the contribution, using Equation 3.2, from each spot in turn providing the spots do not overlap. The (s,θ) coordinates marking the boundary of each spot at any given time are then calculated using the method described in Appendix A.

Heyrovský and Sasselov used this approach to evaluate the the percentage change in flux that could be anticipated from extended sources with starspots. We have adopted many features of their model, but have added several important improvements.

- Incorporation of "Next Generation" stellar atmospheres.
- Inclusion of limb darkening within spots.
- Fully geometric spot treatment, i.e. allowing for the foreshortening of the spot as it approaches the limb.
- Inclusion of more complex spot configurations

3.3 Example lightcurves

In this section several illustrative lightcurves are presented in order to acquaint the reader with typical microlensing spot signatures that could be produced by a range of spots. Various spot, source and lens parameters are examined and their *spot signatures* are compared in terms of the magnitude changes introduced by the features and the timescales of these changes.

In Figure 3.1 the V, R, I and K lightcurves, produced by a microlens transiting the disk of a spotted source of radius $\rho = 0.1$ AER, are presented. Three panels are shown in Figure 3.1. In the left hand panel the stellar disk is shown, indicating the position and size of the spot feature in cross-hatching. The trajectory of the lens is indicated by the arrow. The middle panel indicates the change, Δm, in apparent magnitude as a function of time, given by the formula

$$\Delta m = 2.5 \log_{10}(\frac{F_{LSP}}{F_{USP}}) \tag{3.3}$$

where F_{LSP} and F_{USP} denote the flux from the lensed, spotted source and unlensed, spotted source respectively.

The final panel on Figure 3.1 shows the change in apparent magnitude, Δm_S, due to the spot, given by the formula

$$\Delta m_S = 2.5 \log_{10}(\frac{F_{LSP}}{F_{LSF}}) \tag{3.4}$$

where F_{LSF} is the lensed flux from the spot-free source. The third panel allows the reader to identify the contribution from the spot feature compared to the overall microlensing lightcurve. Δm_S is not, however, an observable flux, but the residual magnitude change that would be observed when a spotted source was compared to an unspotted source with identical lens and source parameters.

Note that Δm_S as defined by Equation 3.3 will give a wavelength dependent non-zero

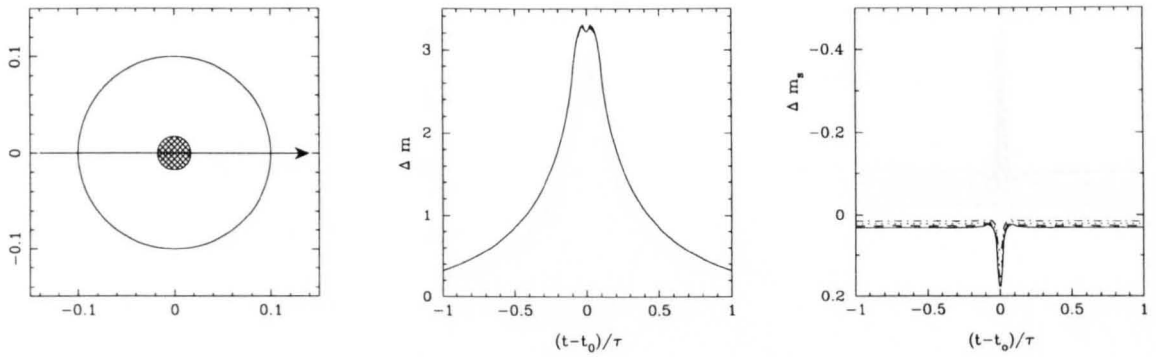

Figure 3.1: The V, R, I and K microlensing light curves produced by the transit of a lens, with minimum impact parameter $u_0 = 0.0AER$, across the disk of a $5000K$ star, of radius $0.1AER$, with $\log g = 4.0$, with a $4200K$ starspot (as shown in the left hand panel) of radius 10°. The magnitude changes, Δm and Δm_s are as defined in Equations 3.3 and 3.4.

offset, even in the absence of lensing. This arises because the integrated unlensed flux from the spotted star will, in any case, introduce a magnitude change when compared to the unspotted star. Thus we can write Δm_S as the sum of two contributions;

$$\Delta m_S = \Delta m_{SL} + 2.5 \log_{10}(\frac{F_{USP}}{F_{USF}}) \tag{3.5}$$

where F_{USF} denotes the unlensed flux from the spot-free star. Hence Δm_{SL} can be regarded as the magnitude change due to the *lensing* of the spots, while the second term represents the non-zero offset discussed above. Although we are, of course, primarily interested in Δm_{SL}, it is useful to include the non-zero offset in the right hand panels of Figure 3.1 as it adds to the clarity of the lightcurve deviations.

The lightcurves shown in Figure 3.1 are plotted as continuous, dashed, dotted and dash dotted lines for V, R, I and K bands respectively.

The cool spot as shown in the first panel of Figure 3.1 produces a small dip in the overall amplification towards the peak of the lightcurve. It can be seen from the final panel of Figure 3.1 that as the lens is transiting the spot there is an imaging effect as the difference between the unspotted and spotted sources produces a change in magnitude. The greatest change occurs at minimum impact parameter when the lens is directly over the spot. At this point the change in magnitude, Δm_{max} induced by the spot can be found as,

$$\Delta m_{max} = \left| 2.5 \log_{10}(\frac{F_{LSP}}{F_{USP}}) - 2.5 \log_{10}(\frac{F_{LSF}}{F_{USF}}) \right|. \tag{3.6}$$

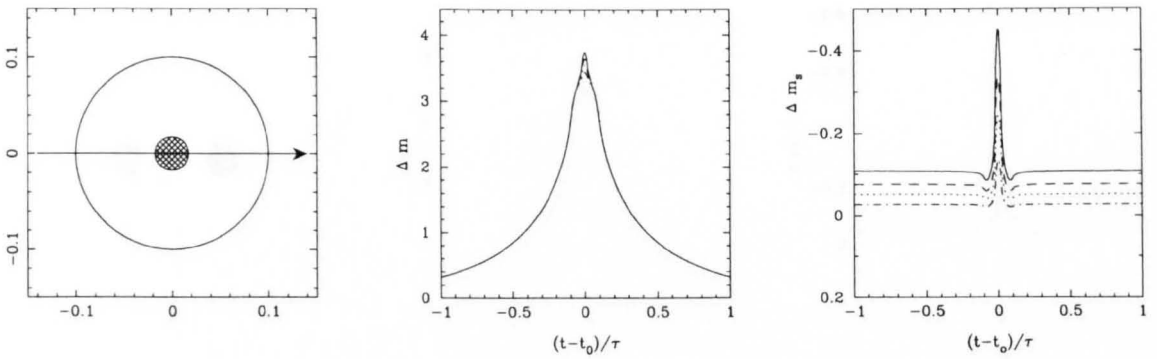

Figure 3.2: The V, R, I and K microlensing light curves produced by the transit of a lens, with minimum impact parameter $u_0 = 0.0AER$, across the disk of a $4000K$ star, of radius $0.1AER$, with $\log g = 1.0$, with a $4800K$ starspot (as shown in the left hand panel) of radius 10°. The magnitude changes, Δm and Δm_s are as defined in Equations 3.3 and 3.4.

In the V band the greatest change in magnitude, Δm_{max} is 0.144 and there are 8 data points, out of the 200 sampled during the Einstein diameter crossing time, where $\Delta m_{max} >$ 0.01mag. These data points correspond to region of the lightcurve when the lens is directly over the spot – during this phase of the lightcurve it is possible to say that lens is imaging the spot.

The effect of the presence of the spot diminishes sharply at longer wavelengths, as could be anticipated from the fact that the contrast in surface brightness between an atmosphere at $5000K$ and $4200K$ diminishes at longer wavelengths.

In contrast, Figure 3.2 presents the lightcurves due to the presence of a *hot spot* on a stellar photosphere with different source parameters of $T_{eff} = 4000K$ and $\log g = 1.0$.

Figure 3.2 is constructed in the same fashion as Figure 3.1 and one can immediately make several useful comparisons about the microlensing spot signatures from hot and cool spots. The effective temperature difference between the two models is the same – $800K$ – yet as can be seen from the final panels the hot spot produces a significantly larger signal. The hot spot provides a peak in the amplification rather than a dip as is the case for the cool spot. Also the *offset* magnitude – as would be seen if a spotted and an unspotted source could be compared directly in the absence of microlensing – is considerably larger as the flux is proportional to T_{eff}^4 . The peak magnitude change, $\Delta m_{max} = 0.34$ in the V band, which is larger than the corresponding change for the cool spot of Figure 3.1. The timescale

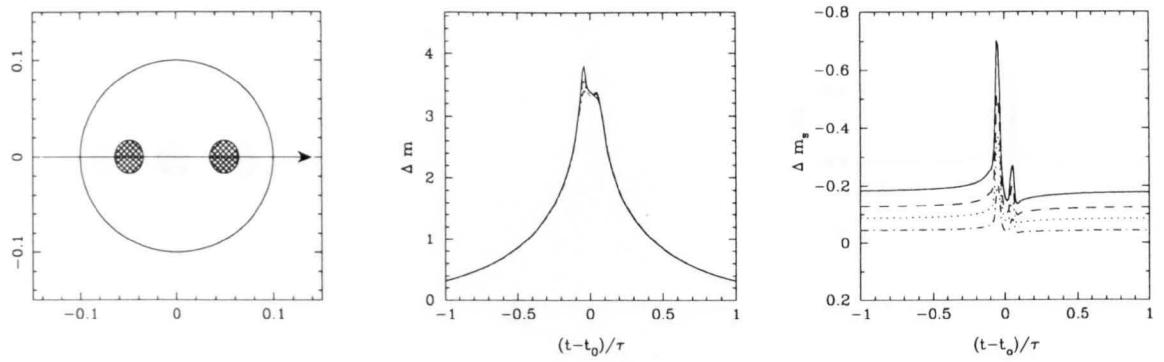

Figure 3.3: The V, R, I and K microlensing light curves produced by the transit of a lens, with minimum impact parameter $u_0 = 0.0AER$, across the disk of a $4000K$ star, of radius $0.1AER$, with $\log g = 1.0$, with two starspots (as shown in the left hand panel) of radius 10° and with $T_{eff} = 4400K$ for the right hand spot and $T_{eff} = 5200K$ for the left hand spot. The magnitude changes, Δm and Δm_s are as defined in Equations 3.3 and 3.4.

of this signature is also longer; 18 data points out of 200 produce $\Delta m_{max} \geq 0.01$mag.

The spot parameters choosen in these examples as well as throughout this Chapter is difficult to discuss in comparison with known astrophysical sources as so little is known about starspots. It is hoped that most of the spot models chosen will seem relevant to the reader, although there are several examples such as the following Figure in which the situation is clearly contrived. The majority of the spot models for which detectability is considered err on the conservative, i.e. small spots with modest temperature differences.

The temperature dependence of spot signatures is further examined in Figure 3.3 – which shows the light curves due to the situation of a source with two spots of different temperatures.

As can be seen from the final panel of Figure 3.3 the spot with the higher effective temperature produces a higher V band magnitude change, $\Delta m_{max} = 0.51$ compared to a value of 0.10 for the cooler spot. This prompts the question: can one constrain a spot temperature directly from a microlensing lightcurve? Whilst one can confidently conclude that a spot signature is due to positive or a negative temperature difference as compared to the stellar photosphere, it is difficult to convincingly conclude one particular spot solution that would account for the signature. These issues shall be considered further in Section 3.5.

In Figure 3.4 the lightcurves due to three spots are presented. In this situation the spots are of identical sizes and temperatures, yet are positioned with varying longitude across

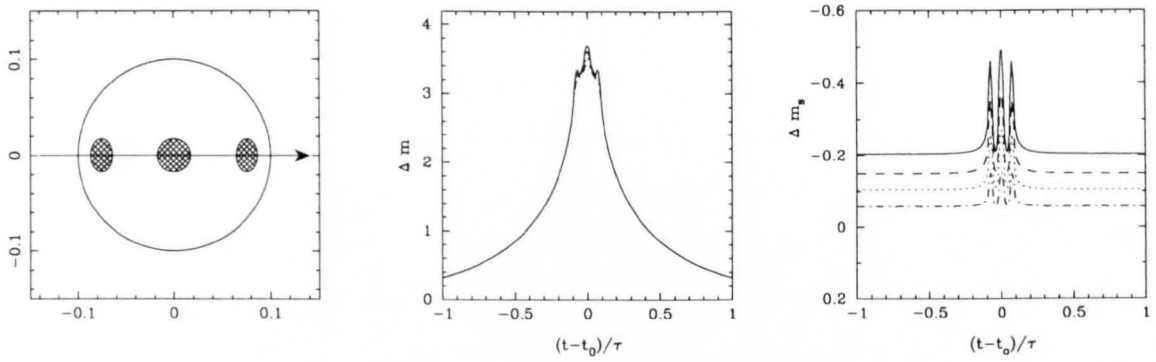

Figure 3.4: The V, R, I and K microlensing light curves produced by the transit of a lens, with minimum impact parameter $u_0 = 0.0AER$, across the disk of a $4000K$ star, of radius $0.1AER$, with $\log g = 1.0$, with three starspots (as shown in the left hand panel). The magnitude changes, Δm and Δm_s are as defined in Equations 3.3 and 3.4.

the photosphere.

We can clearly see that as the spot moves towards the limb its effective size is reduced due to the geometric foreshortening. Furthermore limb darkening effects now have influence on the spot signature; our model incorporates limb darkening within the spot, so a spot close to the limb is darkened with respect to a spot of the same temperature contrast at the centre of the photosphere. As is indicated in the final panel of Figure 3.4, it is the most central spot that produces the most substantial magnitude change with $\Delta m_{max} = 0.29$, the spots closer to the limb suffer the "double whammy" of foreshortening and a reduced intensity, giving maximum magnitude changes of 0.26 for the spot on the left hand limb and 0.26 for the spot on the right hand limb – despite all three spots being of the same temperature.

Figure 3.5 introduces a comparison between spot sizes. Two spots of identical temperature contrast but of different radii produce spot signatures that vary in both peak magnitude change and in the timescale of the signature itself. The larger 12° spot produces a magnitude change according to Equation 3.6 of 0.38 in the V band and the signature is detectable for 41 data points out of the 200 modelled, i.e. 41 points with a value of $\Delta m_{max} > 0.01$. The smaller spot produces a greatest magnitude change of 0.23 mag, with only 20 data points producing an above threshold magnitude change. Thus changing the spot size not only changes the duration of the signature but also its peak value.

In the microlensing lightcurves illustrated so far in this Section, the impact parameter, u_0

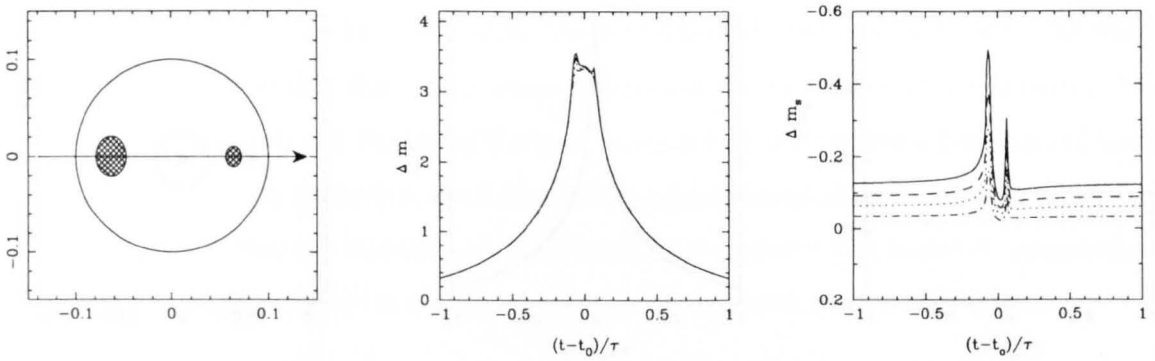

Figure 3.5: The V, R, I and K microlensing light curves produced by the transit of a lens, with minimum impact parameter $u_0 = 0.0AER$, across the disk of a $4000K$ star, of radius $0.1AER$, with $\log g = 1.0$, with two starspots (as shown in the left hand panel) of radius 6° for the right hand spot and 12° for the left hand spot. The magnitude changes, Δm and Δm_s are as defined in Equations 3.3 and 3.4.

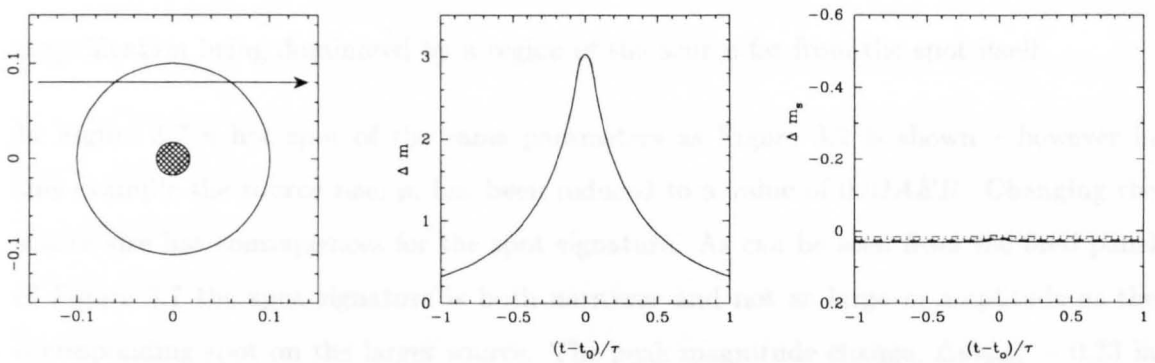

Figure 3.6: The V, R, I and K microlensing light curves produced by the transit of a lens, with impact parameter $u_0 = 0.08AER$, across the disk of a $5000K$ star, of radius $0.1AER$, with $\log g = 4.0$, with a $4200K$ starspot (as shown in the left hand panel). The magnitude changes, Δm and Δm_s are as defined in Equations 3.3 and 3.4.

has been fixed at a value of 0.0 which means that the lens transits directly over the spot. By contrast, in Figure 3.6 a microlensing event is shown in which the lens transits the star, with $u_0 = 0.08$, but does not transit the star spot. Otherwise the source is identical to that of Figure 3.1.

In Figure 3.6 the spot signature is "lost". In the final panel one can see a small chromatic offset between the colour bands but no imaging dip as one would expect from a cool spot. The amplified flux is dominated by the region directly underneath the lens and so the contribution from the spot is not amplified sufficiently to produce a signature. The detectability of a particular spot depends not only on its temperature, position and size but also its position relative to the lens trajectory. There is a small bump due to peak

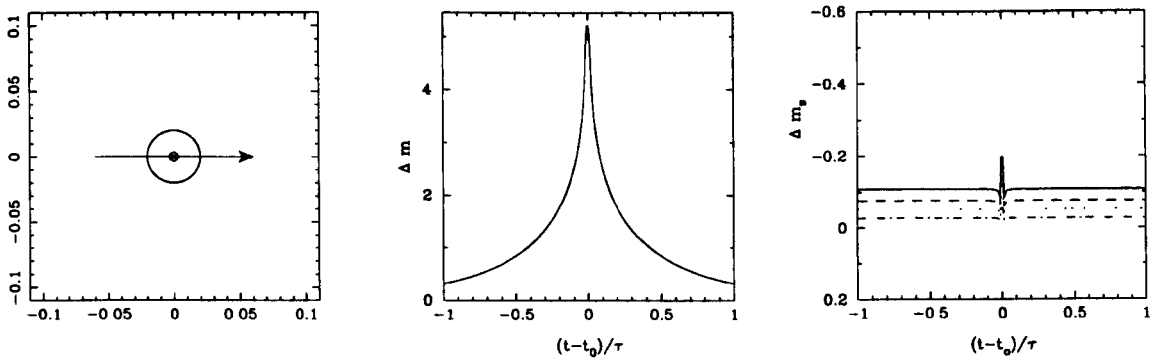

Figure 3.7: The V, R, I and K microlensing light curves produced by the transit of a lens, with minimum impact parameter $u_0 = 0.0AER$, across the disk of a $4000K$ star, of radius $0.02AER$, with $\log g = 1.0$, with a $4800K$ starspot (as shown in the left hand panel) of radius 10°. The magnitude changes, Δm and Δm_s are as defined in Equations 3.3 and 3.4.

magnification being dominated by a region of the source far from the spot itself.

In Figure 3.7 a hot spot of the same parameters as Figure 3.2 is shown – however in this example the source size, ρ, has been reduced to a value of $0.02AER$. Changing the source size has consequences for the spot signature. As can be seen from the final panel of Figure 3.7 the spot signature is both narrower and not as large in amplitude as the corresponding spot on the larger source. The peak magnitude change, $\Delta m_{max} = 0.23$ in the V band. It is the fact that the peak is narrower which would have more significant consequences for detecting the feature. Such a small source is a much less likely candidate for good observational data during the transit portion of the event simply because it will only occur over a few hours. Accordingly the spot signature itself will only be present for a small portion of the transit lightcurve. In Figure 3.7 only about 1% of the data points during the Einstein diameter crossing provide $\Delta m_{max} > 0.1$ mag.

3.4 Spot detectability

A signature from a spot depends on not only its temperature and radius but also its position on the source and that position relative to the lens trajectory. Heyrovský and Sasselov (2000) produced maps of spot detectability using the following detection criteria. A spot signature was regarded as detectable if it produced a 2% change in flux at any one point during the event. The fully geometric treatment of this work allows these detection

maps to be extended to the stellar limb. As is illustrated below spots close to the limb can provide a detectable flux. The other significant improvements are, of course, the atmosphere modelling and the use of 6 colour bands and a more extended analysis of spot parameters. The fully geometric treatment allows a fairer comparison of the spot signature at differing positions: the circular disk treatment, of Heyrovský and Sasselov, means that spots at, e.g. higher, latitudes will have a greater overall area than central spots.

3.4.1 Construction of maps

Maps of spot detectability were constructed by calculating the contribution from a spot at a range of positions on the source. The maps therefore indicate how detectable a spot is at any position on the photosphere for a fixed lens impact parameter, source size and spot parameter. In order to do this it was necessary to calculate lightcurves due to a source with a spot at each position on the source, in turn, and then compare these spotted lightcurves to those from an identical source but without the spot feature. The effects of varying the spot size, lens impact parameter and spot temperature are examined. The maps presented are in 6 colour bands, in order to illustrate the diminishing signature from the spot at longer wavelengths.

3.4.2 Criteria of detectability

Detectability is defined here as a change in magnitude, Δm_{max} greater than a threshold value at any one point during the event. Three threshold values were chosen in this study. A more statistically convincing detection might require several consecutive observations with Δm_s greater than a threshold value. This would clearly limit not only the size but the temperature of detectable spots unless such a strict criteria was adopted using very densely sampled data. In the following Section 3.4.3, we present a series of contour maps, which are calculated from a large number of microlensing lightcurves. In each case the lightcurves model the transit and close to transit portion of the event, beginning when the centre of the source is at a distance of $-0.2AER$ from the lens through minimum projected separation, to $0.2AER$ from the lens. Each lightcurve used to compose the contour plots consisted of 40 equally spaced observations. For zero impact parameter, $u_0 = 0.0$, this

corresponds to 20 data points during the source transit. This is similar to a rapid sampling rate, although not an unachievable one, e.g. if one considers a transit occuring over, for example, 48 hours. As the impact parameter increases throughout the sample of contour maps presented here, there are fewer data points during the crucial transit. In fact, non-transit event maps are also presented as a star spot present on certain regions of the photosphere can still achieve the threshold magnitude change, by which we define spot detectability, in this case.

3.4.3 Results

Figure 3.8 presents the regions of a 4000 K, $0.1AER$ source that provide at least one data point with a magnitude change of 0.01 for the lightest shade of grey, 0.05 for the mid-grey and 0.1 for the darkest grey. The spot being considered has radius 3° and has effective temperature of 4800 K. The spot and the star have a constant $\log g = 1.0$. The zero impact parameter considered in Figure 3.8 allows spots occurring in a central band across the photosphere to produce magnitude changes and thus be imaged. However spots on a great deal of the photosphere can not produce detectable signatures. As one considers longer wavelengths, not only does the detectable region contract but also the magnitude of the signature is reduced. In the top-right panel the effects of the sampling strategy can be seen. Spots lying very close to the lens at the point of observation can be detected more readily than spots slightly further away. This effect is particularly evident for the very small spots being considered in Figure 3.8; as one considers spots of a slightly larger area this 'pixelation' is greatly smoothed. It could also, of course, be smoothed by denser sampling.

The spot parameters presented in Figure 3.8 and throughout this Section are intended to demonstrate that microlensing could be sensitive to a conservative range of possible spot parameters, in particular spot parameters not too far removed from typical sunspots.

Figure 3.8 demonstrates that small spots even close to the limb can be imaged as long as the lens passes very close to them. However identical spots close to the centre will provide a greater signal.

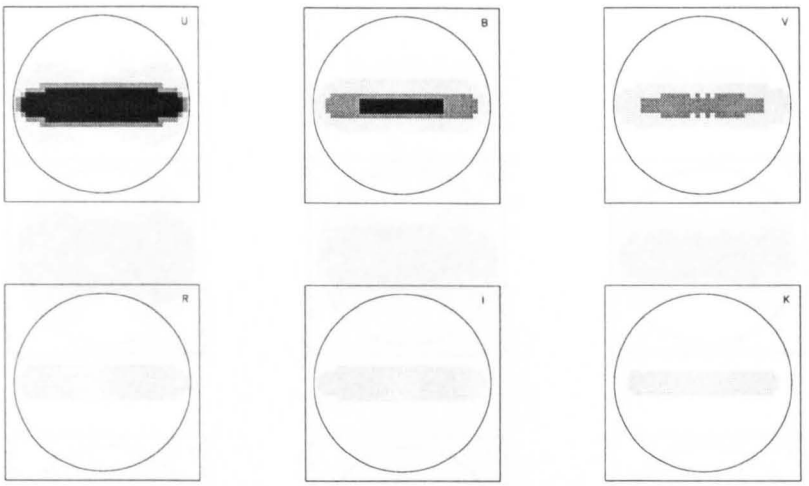

Figure 3.8: The regions of the source photosphere where a 3° radius spot would provide a 0.01, 0.05 and 0.1 magnitude signature during a microlensing event with impact parameter, $u_0 = 0.0$.

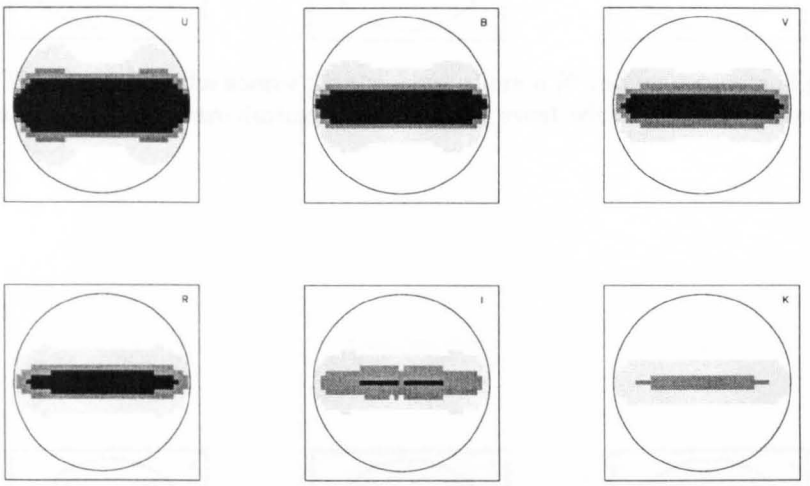

Figure 3.9: The regions of the source photosphere where a 6° radius spot would provide a 0.01, 0.05 and 0.1 magnitude signature during a microlensing event with impact parameter, $u_0 = 0.0$.

The peak magnitude changes typically occur at the data point where the lens to spot projected distance is at its minimum, as would be expected.

In Figures 3.9, 3.10 and 3.11 spot detectability maps are presented in the same manner as Figure 3.8. However in these cases the radius of the spot is increased: values of 6°, 9° and 12° are considered on a photosphere otherwise identical to Figure 3.8 (again these are hot spots of 4800 K).

As one might expect the larger spots provide a larger detectable region on the photosphere. Furthermore the magnitude changes become larger with increasing spot signature. Whilst these maps only plot the peak magnitude change many regions, particularly central ones,

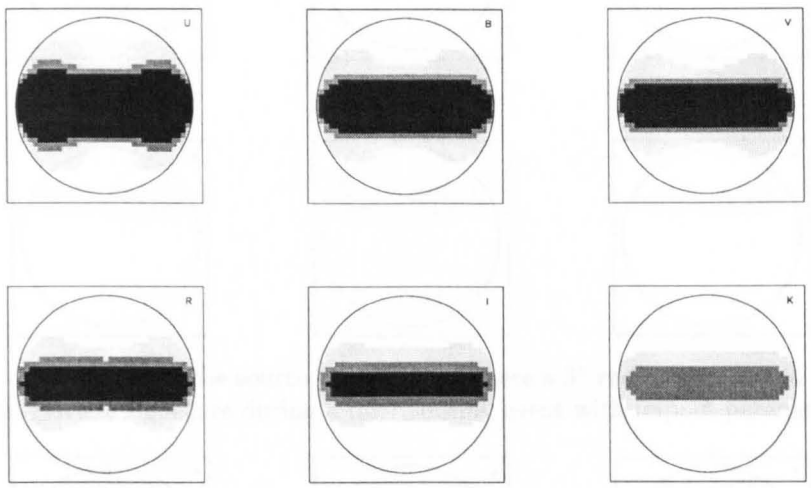

Figure 3.10: The regions of the source photosphere where a 9° radius spot would provide a 0.01, 0.05 and 0.1 magnitude signature during a microlensing event with impact parameter, $u_0 = 0.0$.

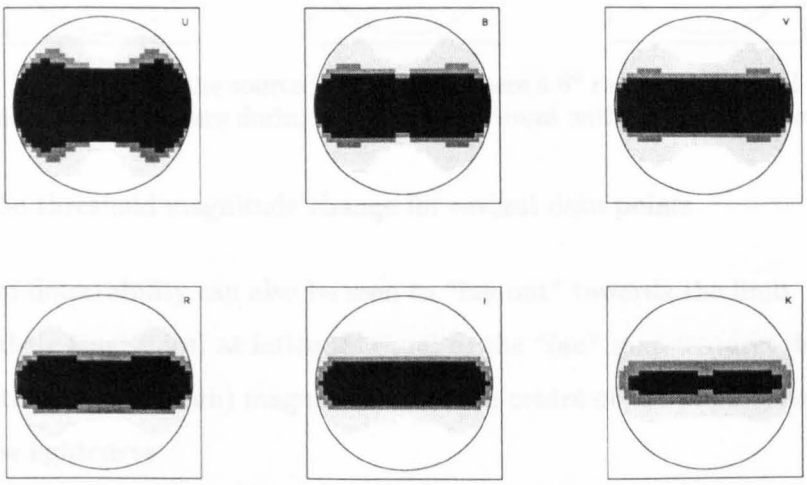

Figure 3.11: The regions of the source photosphere where a 12° radius spot would provide a 0.01, 0.05 and 0.1 magnitude signature during a microlensing event with impact parameter, $u_0 = 0.0$.

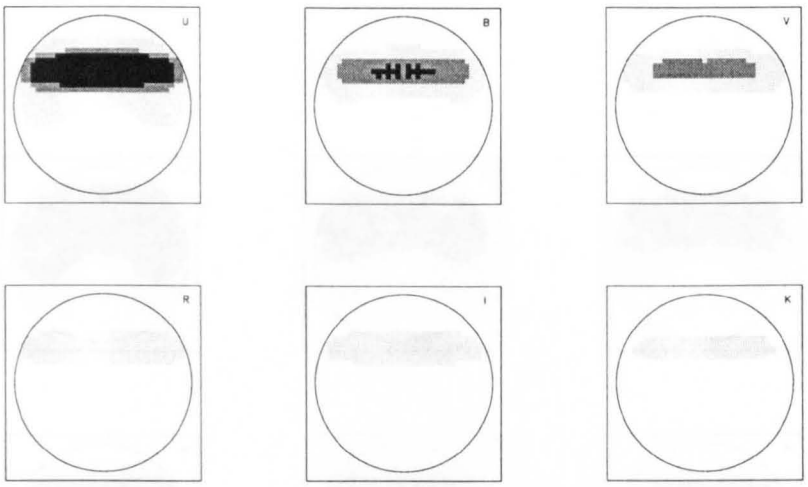

Figure 3.12: The regions of the source photosphere where a 3° radius spot would provide a 0.01, 0.05 and 0.1 magnitude signature during a microlensing event with impact parameter, $u_0 = 0.04$

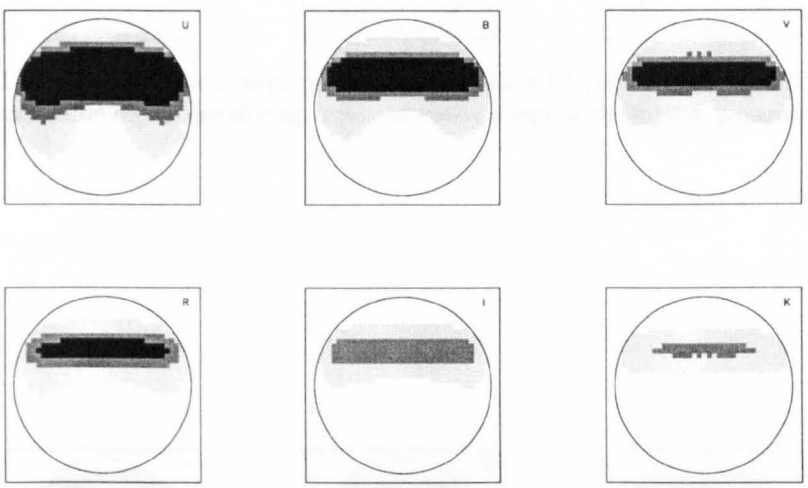

Figure 3.13: The regions of the source photosphere where a 6° radius spot would provide a 0.01, 0.05 and 0.1 magnitude signature during a microlensing event with impact parameter, $u_0 = 0.04$

will exceed the threshold magnitude change for several data points.

The regions of detectability can also be seen to "fan out" towards the limb. Central spots (in terms of their longitudes) at latitudes equal to the "fan" map features do not produce similar signatures as the (high) magnification in the centre of the photosphere completely dominates the lightcurve.

In Figures 3.12, 3.13, 3.14 and 3.15 detectability maps are presented for 3°, 6°, 9° and 12° radius spots; on this occasion the impact parameter is increased to $0.04AER$. The lens is clearly still transiting the $0.1AER$ source but the zones of detectability are moved up on the projected photophere and so now the detectable spots generally occur closer to the

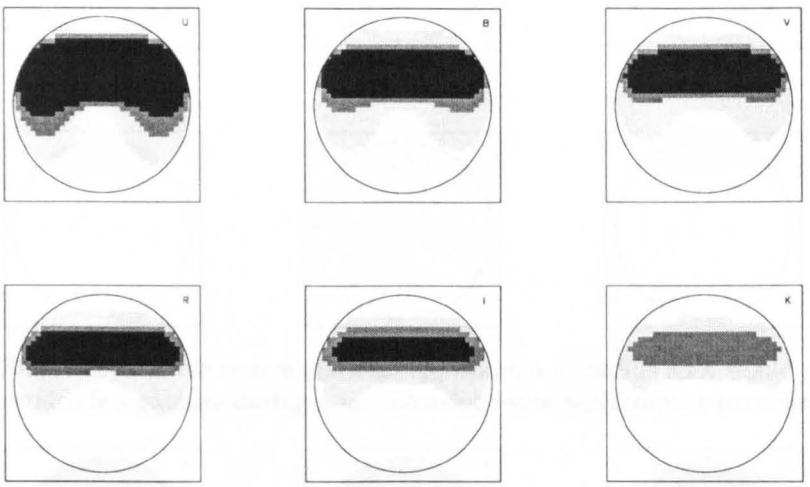

Figure 3.14: The regions of the source photosphere where a 9° radius spot would provide a 0.01, 0.05 and 0.1 magnitude signature during a microlensing event with impact parameter, $u_0 = 0.04$

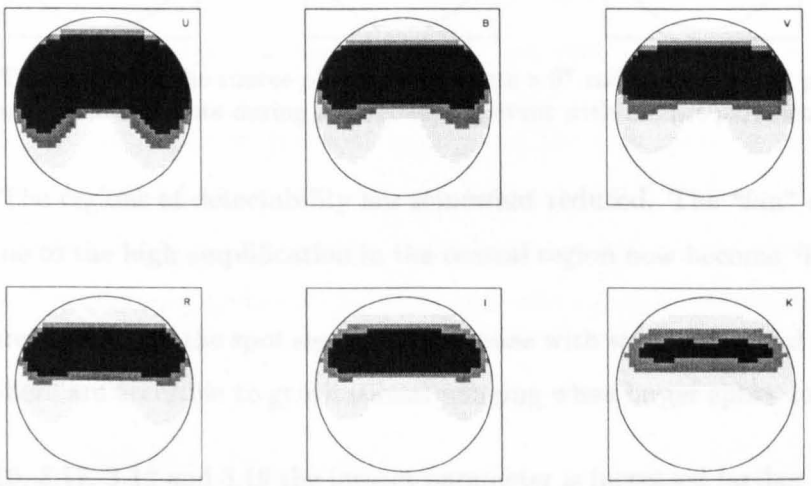

Figure 3.15: The regions of the source photosphere where a 12° radius spot would provide a 0.01, 0.05 and 0.1 magnitude signature during a microlensing event with impact parameter, $u_0 = 0.04$

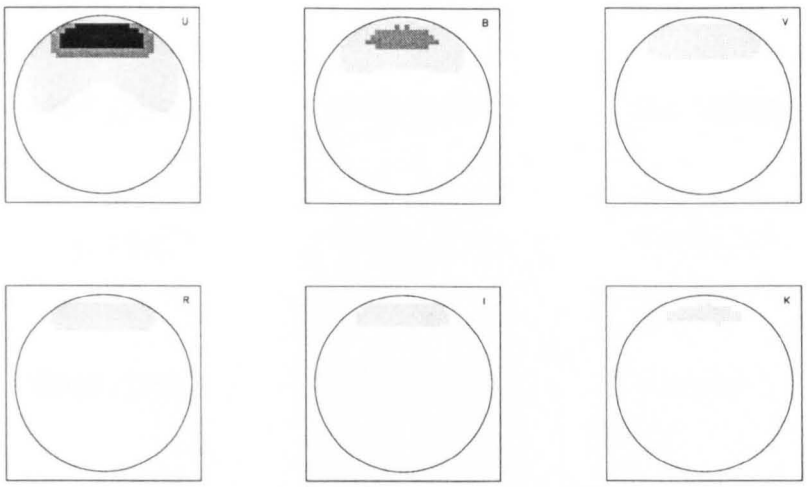

Figure 3.16: The regions of the source photosphere where a 3° radius spot would provide a 0.01, 0.05 and 0.1 magnitude signature during a microlensing event with impact parameter, $u_0 = 0.08$

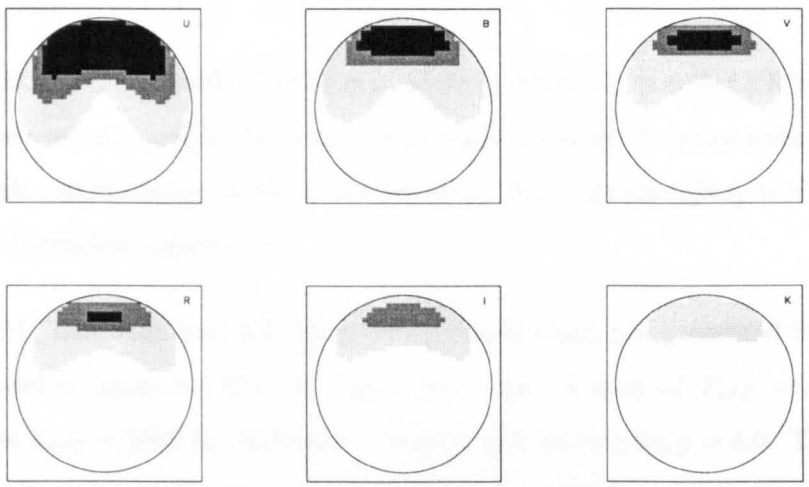

Figure 3.17: The regions of the source photosphere where a 6° radius spot would provide a 0.01, 0.05 and 0.1 magnitude signature during a microlensing event with impact parameter, $u_0 = 0.08$

stellar limb. The regions of detectability are somewhat reduced. The "fan" effects at the stellar limb due to the high amplification in the central region now become "lung" shapes.

As with the previous maps, the spot signatures decrease with wavelength and greater areas of the photophere are accesible to gravitational imaging when larger spots are considered.

In Figures 3.16, 3.17, 3.18 and 3.19 the impact parameter is increased further to $0.08AER$. This exaggerates the "lung" features, where much of the photosphere still presents detectable spot signatures. These "lung" shapes are particularly evident for the larger radius spots when the projected distance to the lens from the spot is decreased by the larger spot.

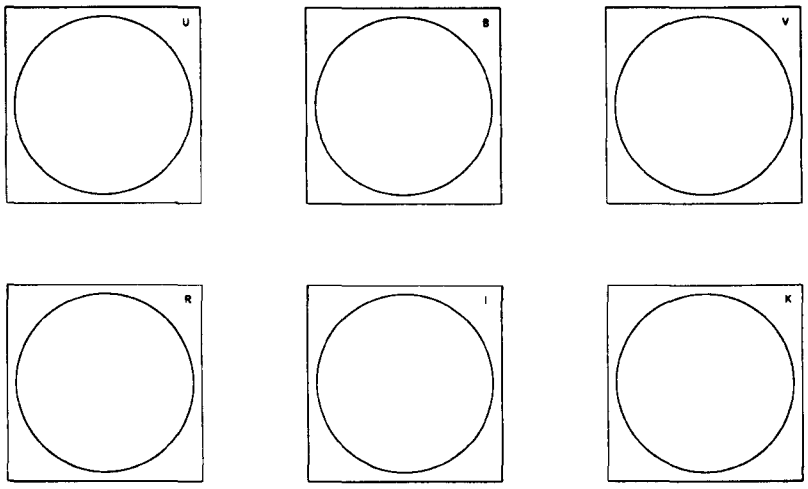

Figure 3.24: The regions of the source photosphere where a 3° radius *cool* spot would provide a 0.01, 0.05 and 0.1 magnitude signature during a microlensing event with impact parameter, $u_0 = 0.0$

In Figures 3.20, 3.21, 3.22 and 3.23 the lens impact parameter is $0.12AER$ corresponding to a non-transit event. Despite the lens not actually crossing the photosphere it can still provide enough magnification to allow the detection of a large enough spot if located close to the point of smallest separation.

In Figures 3.24, 3.25, 3.26 and 3.27 spot detectability maps are presented for cool spots. The spot model is based on that of Figure 3.1 - i.e. a spot of $T_{eff} = 4200$ K on a photosphere of $T_{eff} = 5000$ K, with both star and spot having $\log g = 4.0$. The four maps presented are for transits of zero impact parameter but with varying spot size.

It can be seen, in comparison to previous maps, that the cool spots do provide smaller magnitude changes than hot spots as seen for individual cases. This has the direct consequence that microlensing is not as sensitive to cool spots as hot spots and that less of the photosphere will provide a detectable spot signature, other than in the case of the largest spots.

3.4.4 Spot timescales

The peak magnitude change maps presented above allow the regions of the source photosphere to be identified on which a spot signature can exceed a threshold magnitude change, thus rendering the spot detectable. The duration of these magnitude changes is

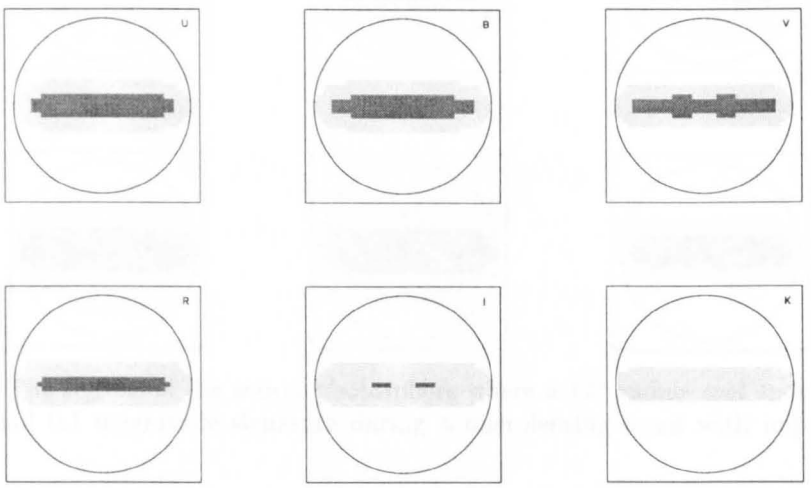

Figure 3.25: The regions of the source photosphere where a 6° radius *cool* spot would provide a 0.01, 0.05 and 0.1 magnitude signature during a microlensing event with impact parameter, $u_0 = 0.0$

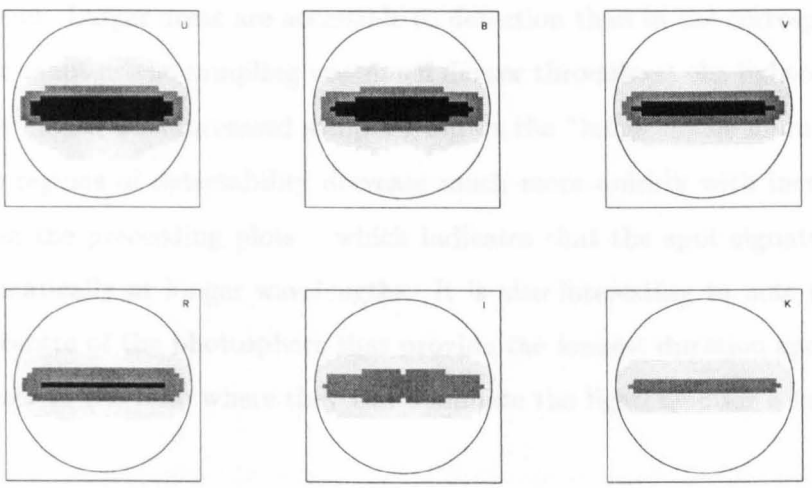

Figure 3.26: The regions of the source photosphere where a 9° radius *cool* spot would provide a 0.01, 0.05 and 0.1 magnitude signature during a microlensing event with impact parameter, $u_0 = 0.0$

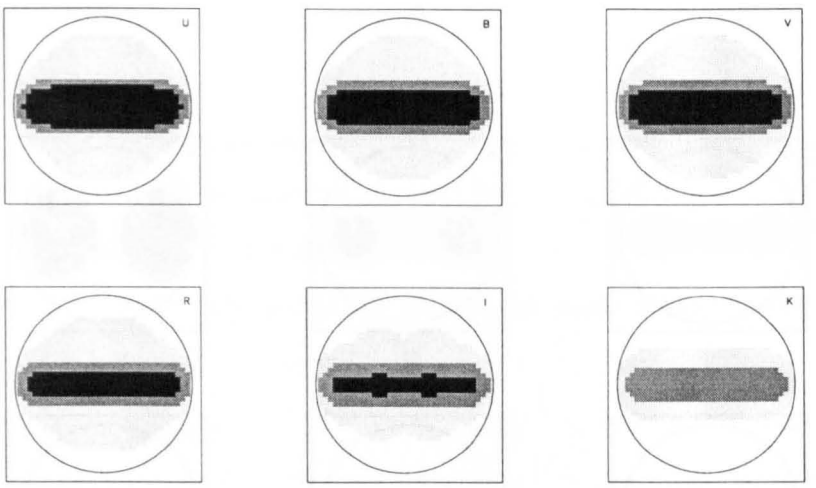

Figure 3.27: The regions of the source photosphere where a 12° radius *cool* spot would provide a 0.01, 0.05 and 0.1 magnitude signature during a microlensing event with impact parameter, $u_0 = 0.0$

also of some interest however. Quite simply, the longer a spot signature is higher than the threshold magnitude value, the easier it will become to detect.

Figures 3.28 and 3.29 were produced from a series of microlensing lightcurves, each consisting of 100 equally spaced observations, rather than in the previous examples where 40 observations were considered. Figures 3.28 and 3.29 present the regions of a source photosphere where a threshold magnitude change would be exceeded for a specified percentage of the overall event. Larger areas are accessible to detection than in the corresponding magnitude change maps as the sampling was much denser throughout the lightcurves used to produce these maps. This increased sampling allows the "lungs" to be more convincingly imaged. The regions of detectability decrease much more quickly with increasing wavelength than in the preceeding plots – which indicates that the spot signature decreases in width dramatically at longer wavelengths. It is also interesting to note that it is not spots at the centre of the photosphere that provide the longest duration spot signatures, but spots closer to the limb where they can dominate the lightcurve for a longer fraction of the event.

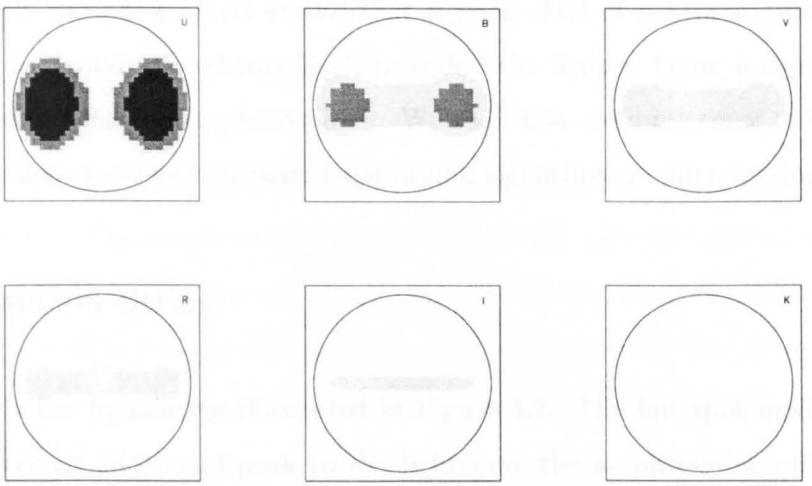

Figure 3.28: The regions of the source photosphere where a 6° radius *hot* spot would provide a 0.02 magnitude signature during a microlensing event with impact parameter, $u_0 = 0.0$ for 2%, 5% and 10% of the Einstein diameter crossing time

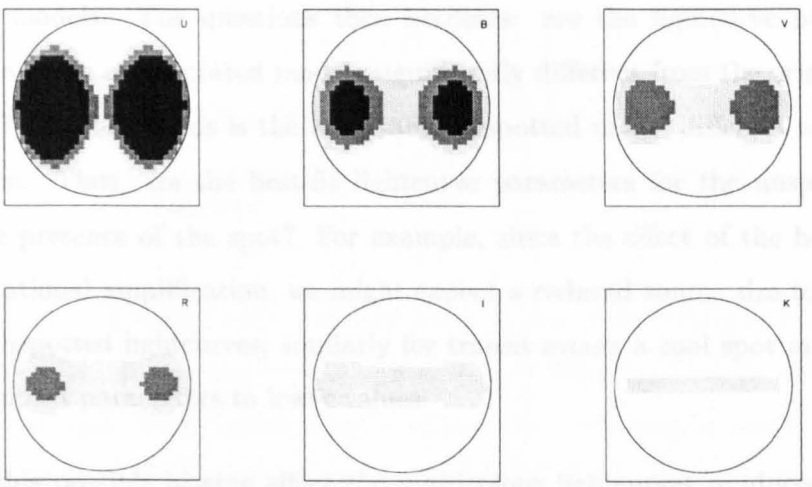

Figure 3.29: The regions of the source photosphere where a 6° radius *hot* spot would provide a 0.01 magnitude signature during a microlensing event with impact parameter, $u_0 = 0.0$ for 2%, 5% and 10% of the Einstein diameter crossing time

3.5 Complications

In the previous section we have shown that a great deal of a source photosphere can be accessible to "gravitational imaging", provided the feature being imaged lies within a certain region of the source photosphere. We shall now examine some of the potential complications that could be anticipated due to spot signatures on microlensing lightcurves.

3.5.1 Parameter fitting

Consider again the lightcurves illustrated in Figure 3.2. The hot spot modelled in that Figure produces an additional peak to the lightcurve the amplitude of which decreases with increasing wavelength. If we were to ignore the effects of the spot and attempt to fit an unspotted lightcurve to this event, would our fit yield the correct event parameters? Clearly there are several issues to address here. On the one hand we might expect (or at least hope) that *no* unspotted model would give an acceptable goodness-of-fit to the spotted lightcurves – indeed this must be the case as we approach the limit of perfect photometric data and infinitely dense sampling. For realistic data errors and sampling, however, we might find that our spotted lightcurves can be fitted acceptably by a range of unspotted models. The questions then becomes: are the lightcurve parameters of the acceptable range of unspotted models significantly different from the original spotted source model? In other words is the acceptable unspotted model different to that of the spotted source. Thus, are the best-fit lightcurve parameters for the unspotted model biased by the presence of the spot? For example, since the effect of the hot spot is to provide additational amplification, we might expect a reduced source size to provide the best fitting unspotted lightcurves; similarly for transit events a cool spot might bias the best fitting impact parameters to lower values.

To examine this possible biasing effect the multicolour lightcurves produced by spotted sources were fitted to a grid of unspotted extended source events with the same effective temperature and $\log g$ and hence, the same limb darkening. The grid of unspotted models was produced for a range of values of source radius and impact parameter.

Initially a cool spot on a stellar photosphere was considered – akin to Figure 3.1. This case was then fitted to the unspotted source grid by means of a χ^2 minimisation in order to find the most appropriate unspotted source model. The χ^2 was calculated as

$$\chi^2 = \frac{\sum |\frac{\Delta m_{max}}{\sigma}|^2}{n} \tag{3.7}$$

where Δm_{max} is defined in Equation 3.6, n is the number of observations and σ is the photometric error. The source of 5000 K and $\log g = 4.0$ with the spot of 4200 K. This was then repeated for a hot spot of 4800 K on a 4000 K and $\log g = 1.0$ source. In both cases the source radius was $0.1AER$ and the spot radius was 10° and positioned at the centre of the source. Results of such fitting over the Einstein diameter crossing time are presented in Table 3.1.

			U	B	V	R	I	K
hot spot	$u_0 = 0.0$	χ^2	85.98	21.04	10.88	6.84	3.66	2.07
		ρ	0.08	0.08	0.088	0.09	0.092	0.094
		u_0	0.005	0.005	0.00	0.00	0.00	0.00
	$u_0 = 0.05$	χ^2	1.63	1.33	1.15	1.18	1.05	1.09
		ρ	0.10	0.10	0.10	0.098	0.098	0.098
		u_0	0.055	0.055	0.05	0.05	0.05	0.05
cool spot	$u_0 = 0.0$	χ^2	5.10	4.24	3.65	3.02	2.32	1.77
		ρ	0.108	0.106	0.104	0.10	0.10	0.10
		u_0	0.00	0.005	0.00	0.01	0.01	0.00
	$u_0 = 0.05$	χ^2	1.14	1.18	1.15	1.13	1.13	1.13
		ρ	0.102	0.102	0.10	0.10	0.10	0.098
		u_0	0.05	0.05	0.05	0.05	0.05	0.05

Table 3.1: The best fitting parameters, u_0 and ρ and the reduced χ^2 statistic, of unspotted sources in 6 colour bands to spotted sources.

As can be seen from 3.1 cool spots are very hard to detect in comparison to hot spots. Neglecting possibility of hot spots could lead to poorly fitted lightcurves with the source radius underestimated. The possible biasing effects are less strong at longer wavelengths and so, hopefully, a spot signature would be identified by its chromatic signature. The biasing of the event parameters only appears to be significant when a large spot signature is present, i.e. a direct transit of a hot spot and it is highly likely that in such a situation the spot would be identified at some stage of the analysis.

The underestimation of source radius could, however, be avoided completely by the use

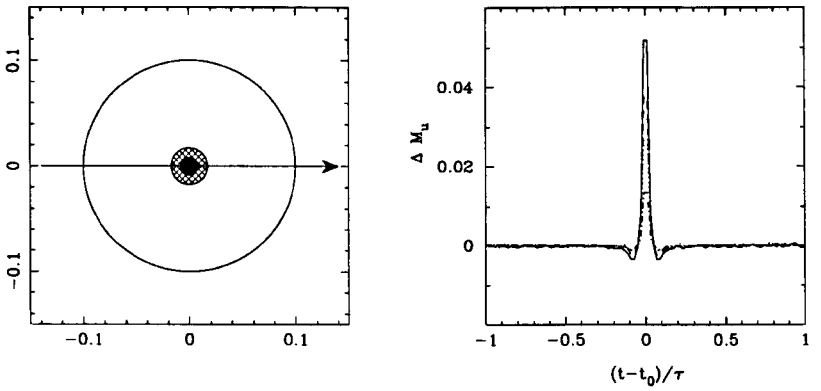

Figure 3.30: The V, R, I and K microlensing light curves produced by the transit of a lens, with minimum impact parameter $u_0 = 0.0AER$, across the disk of a 4000 K star, of radius $0.1AER$, with $\log g = 1.0$, with a 4800 K starspot of radius 10° with additional central temperature structure of 5200 K of 5° (as shown in the left hand panel). Δm_u is as defined in Equation 3.8.

of polarisation. Polarisation observations allow the source radius to be found accurately during a transit event, as the polarisation increases towards the limb (see Simmons et al. 1995a, b and Newsam et al. 1998).

3.5.2 More complex spot model

We have seen in the previous section that high time resolution observations during a transit event can place useful constraints on the existence or otherwise of spots on particular regions of the photosphere. The question remains as to whether one can constrain the detailed structure of spot features from such observations.

Figure 3.30 shows a comparison between the light curves produced by the event illustrated in Figure 3.2 and a similar event, with the same stellar and lens parameters, but in which the spot has additional temperature structure – specifically a central 'umbra' of temperature 5200 K and radius 5° surrounded by a cooler 'penumbra' of temperature 4800 K (the same temperature as the uniform spot of Figure 3.2). The right hand panel of Figure 3.30 shows the difference, in the magnification in terms of magnitude between the two scenarios, given by

$$\Delta m_u = 2.5 \log_{10} \left(\frac{F_{\rm LSP}}{F_{\rm USP}} \right)_{struc} - 2.5 \log_{10} \left(\frac{F_{\rm LSP}}{F_{\rm USP}} \right)_{no-struc} \tag{3.8}$$

It is evident from Figure 3.30 that the effect of the spot structure is small, with a peak deviation from the uniform temperature case of only $\Delta M_u = 0.05$ mag. Clearly, then the

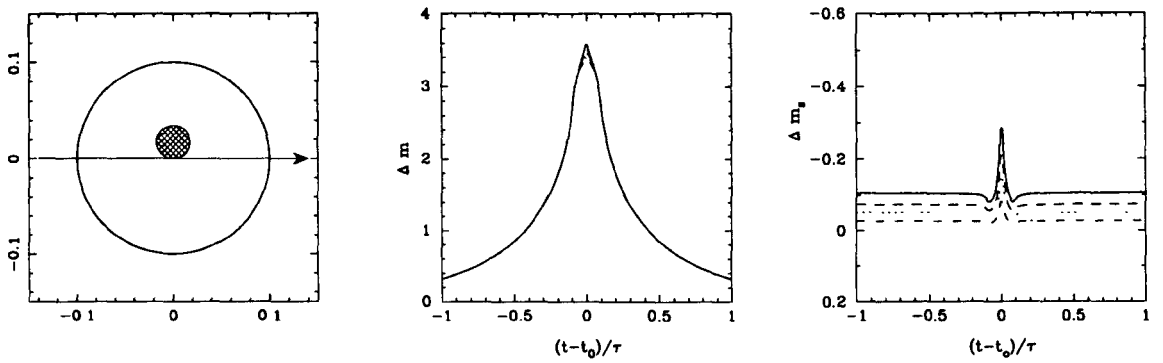

Figure 3.31: The V, R, I and K microlensing light curves produced by the transit of a lens, with minimum impact parameter $u_0 = 0.0AER$, across the disk of a $4000K$ star, of radius $0.1AER$, with $\log g = 1.0$. The star features a 4800 K spot of radius 10°. which is centred on a latitude of 10° (as shown in the left hand panel). The magnitude changes, Δm and Δm_s are as defined in Equations 3.3 and 3.4.

detection of temperature structure, given the accuracy of current photometry, would be very difficult. A more serious difficulty, however, is presented by the severe ill-posedness of the problem: since spots need not in general be circular it is likely that the specific photometric signature of temperature structure within a circular spot could be closely approximated by a non-circular spot of uniform temperature.

3.5.3 Degeneracy between models

For a particular lightcurve signature one can expect to find a large number of spot configurations that would result in approximately the same magnitude change and number of observations above the threshold. Of course, for a given set of stellar and lens parameters, the lightcurves are only sensitive to spots within the detectability regions discussed in Section 3.4.3, so there may in any case be *outlying* spots that are impossible to constrain.

To illustrate this degeneracy, consider a 10° radius spot of $T_{eff} = 4800$ K positioned slightly off-centre on a $0.1AER$, 4000 K, $\log g = 1.0$ source being microlensed with $u_0 = 0.0$ as illustrated in Figure 3.31

In the V colour band the spot indicated in Figure 3.31 produces a peak magnitude change of 0.151 with the threshold magnitude of 0.01 mags being exceeded for 9% of the event. We can compare this to a hotter yet smaller spot centred at the same position as illustrated

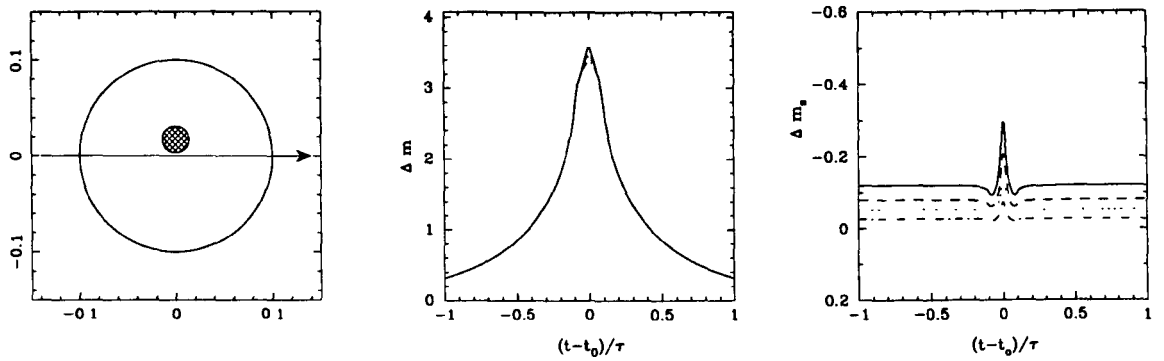

Figure 3.32: The V, R, I and K microlensing light curves produced by the transit of a lens, with minimum impact parameter $u_0 = 0.0AER$, across the disk of a $4000K$ star, of radius $0.1AER$, with $\log g = 1.0$. The star features a 5200 K spot of radius 8°. which is centred on a latitude of 10° (as shown in the left hand panel). The magnitude changes, Δm and Δm_s are as defined in Equations 3.3 and 3.4.

by Figure 3.32

It can be seen immediately that the spot signature due to the spot in Figure 3.32 is very similar to that of Figure 3.31. The V band threshold magnitude change is achieved for 10% of the event and the peak magnitude change is 0.146. This mirroring of spot signatures is repeated throughout the colour bands modelled as shown by Figure 3.33

Figure 3.33 presents the differences in magnitude between the V, R, I and K lightcurves as continuous, dashed, dotted and dash dotted lines respectively. The x-axis of Figure 3.33 can be written as

$$\Delta m_{larger} - \Delta m_{hotter} = 2.5 \log_{10} \left(\frac{F_{\rm LSP}}{F_{\rm USP}} \right)_{hotter} - 2.5 \log_{10} \left(\frac{F_{\rm LSP}}{F_{\rm USP}} \right)_{cooler} \tag{3.9}$$

where the "hotter" starspot is illustrated by Figure 3.32 and the "cooler" by Figure 3.31. The magnitude differences between the models are small and it would require exceptional photometry to discriminate between the models, despite the 400 K and 2° radius difference between the spots.

The spot signature could be additionally constrained by prudent use of the varying magnitude differences through the sequence of colour bands – of course this would require excellent data in multiple colour bands – as the differences vary across the colour bands.

In Figures 3.34, 3.35 and 3.36, three sets of spot configurations and their lightcurves are

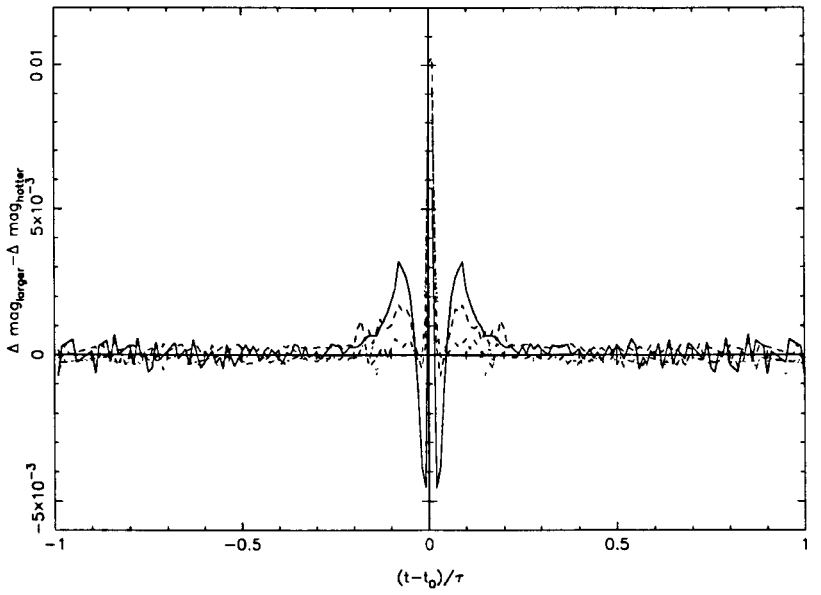

Figure 3.33: A comparison (as defined by Equation 3.9 of the V, R, I and K microlensing lightcurves produced by Figures 3.31 and 3.32.

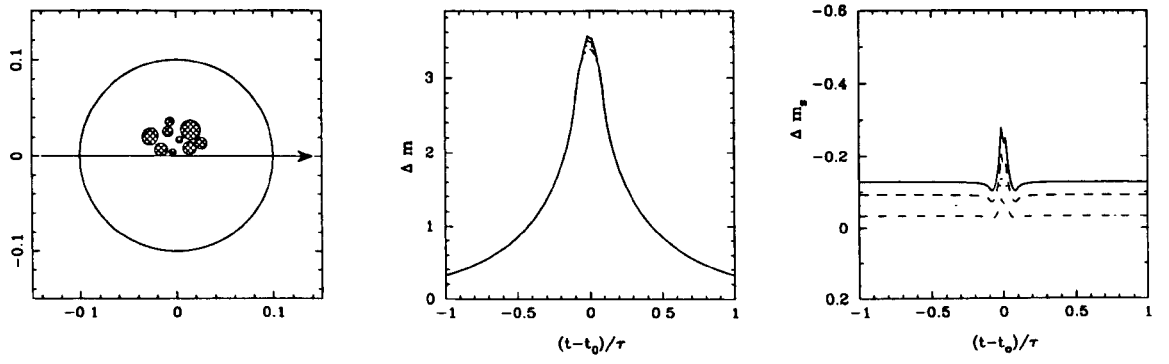

Figure 3.34: The V, R, I and K microlensing light curves produced by the transit of a lens, with minimum impact parameter $u_0 = 0.0AER$, across the disk of a $4000K$ star, of radius $0.1AER$, with $\log g = 1.0$, with $4800K$ starspots (as shown in the left hand panel) of assorted radii. The magnitude changes, Δm and Δm_s are as defined in Equations 3.3 and 3.4.

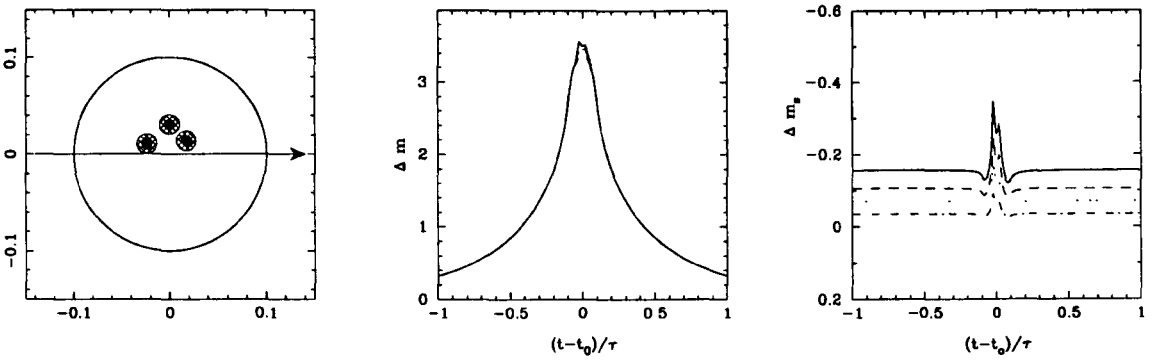

Figure 3.35: The V, R, I and K microlensing light curves produced by the transit of a lens, with minimum impact parameter $u_0 = 0.0AER$, across the disk of a $4000K$ star, of radius $0.1AER$, with $\log g = 1.0$, with three $4800K$ starspot of radius 6° with additional central temperature structure of 5600 K of 3° (as shown in the left hand panel) . The magnitude changes, Δm and Δm_s are as defined in Equations 3.3 and 3.4.

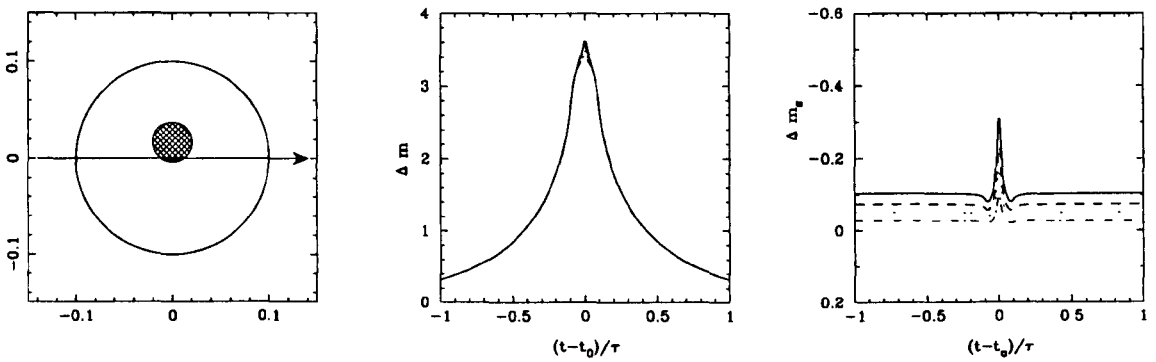

Figure 3.36: The V, R, I and K microlensing light curves produced by the transit of a lens, with minimum impact parameter $u_0 = 0.0AER$, across the disk of a $4000K$ star, of radius $0.1AER$, with $\log g = 1.0$, with a $4600K$ starspot of radius 12° (as shown in the left hand panel). The magnitude changes, Δm and Δm_s are as defined in Equations 3.3 and 3.4.

presented. These Figures are intended to demonstrate how quite different spot configurations can produce very similar microlensing signatures.

The spot signatures from Figures 3.31, 3.32, 3.34, 3.35 and 3.36 are compared in Table 3.2 in terms of the peak magnitude change due to the presence of the spot(s) and the percentage, t_s, of the Einstein diameter crossing time for which the spot signature is higher than a threshold value of 0.01 magnitudes.

		U	B	V	R	I	K
Figure 3.31	Δm_s	0.280	0.211	0.151	0.106	0.074	0.024
	t_s	13%	12%	9%	7%	4%	2%
Figure 3.32	Δm_s	0.300	0.216	0.146	0.097	0.066	0.011
	t_s	15%	13%	10%	8%	3%	2%
Figure 3.34	Δm_s	0.230	0.175	0.126	0.090	0.064	0.022
	t_s	14%	13%	9%	7%	4%	3%
Figure 3.35	Δm_s	0.327	0.243	0.170	0.117	0.081	0.026
	t_s	16.5%	14%	11.5%	9%	7%	3%
Figure 3.36	Δm_s	0.298	0.231	0.170	0.123	0.088	0.031
	t_s	13%	11%	9%	7%	4%	2%

Table 3.2: Comparison of 5 similar microlensing lightcurves produced by differing spot models as illustrated in indicated Figures, in terms of the magnitude and duration of the spot signature, in 6 colour bands.

The magnitude changes and their durations, illustrated by Table 3.2, are indeed very similar and display strongly correlated chromatic effects. Moreover, it is possible to invent many other maculations that would produce similar results. This illustrates the difficulty in attributing a spot signature to just one solution; in particular, the inverse proplem nature of Equation 3.2 and the difficulties in obtaining the correct spot solution, $I_{\rm sp}(s,\theta)$, when the are many possible solutions that would provide the same flux.

Figure 3.37 shows the 99%, 90% and 68.3% confidence regions one would find when fitting a particular spot signature in the V colour band to a grid of lightcurves. In this example only the size and temperature contrast are examined and a photometric error of 0.02 magnitudes was used. All the spots are central and appear on a source of identical radius, temperature and surface gravity. The correct spot solution of 4800 K and 10° radius is found. The "banana" shape of the confidence regions illustrate that slightly smaller but hotter spots *or* slightly larger but cooler spots would also provide a reasonable goodness

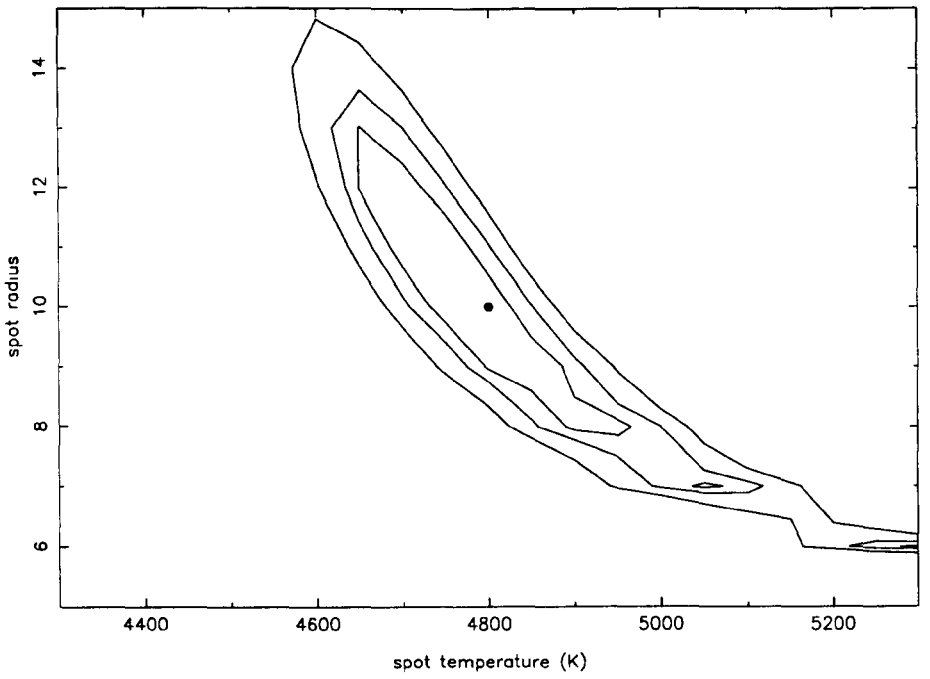

Figure 3.37: The 99%, 90% and 68.3% confidence regions in fitting a grid of spotted lightcurves to the V band lightcurve illustrated in Figure 3.2. The best fitting parameters are indicated by the circle and coincide with the correct parameters, indicated by the cross.

of fit to the original lightcurve.

3.5.4 Rotation

Interestingly, for the case of a rotating source, one can change the ratio of the amplitude to width for the spot signature, since this effectively changes the transverse velocity of the lens with respect to the spot, without changing the lens transverse velocity with respect to the star as a whole.

Consider first the situation illustrated by Figure 3.38, where a hot spot of 4800 K on the same photosphere as Figure 3.2, except for source rotation now being considered. Figure 3.38 illustrates the admittedly artificial situation of the period of rotation of the source being equal to Einstein radius crossing time, i.e. the source makes one complete revolution in exactly the same time as it crosses one Einstein ring radius.

The axis of rotation of the source star in Figure 3.38 is perpendicular to the lens trajectory. At minimum impact parameter the spot is directly underneath the lens, providing the large

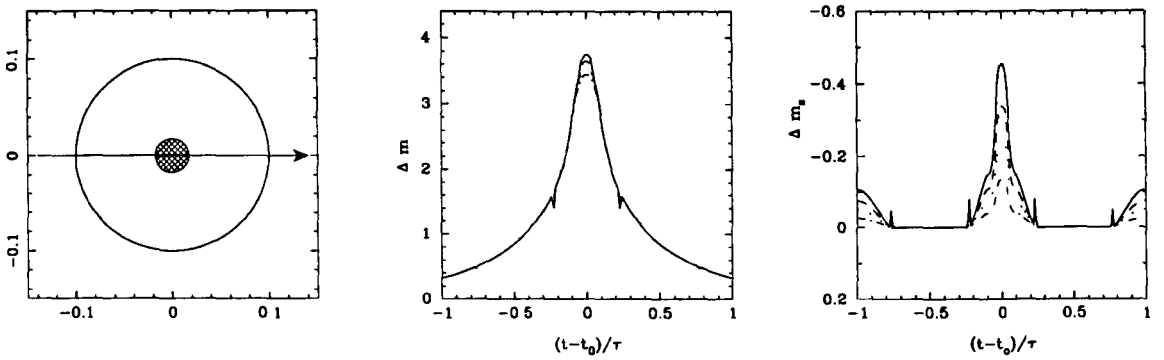

Figure 3.38: The V, R, I and K microlensing light curves produced by the transit of a lens, with minimum impact parameter $u_0 = 0.0AER$, across the disk of a $4000K$ star, of radius $0.1AER$, with $\log g = 1.0$, with a $4800K$ starspot (as shown in the left hand panel) of radius 10° with the source rotating with a period equal to the Einstein radius crossing time. The magnitude changes, Δm and Δm_s are as defined in Equations 3.3 and 3.4.

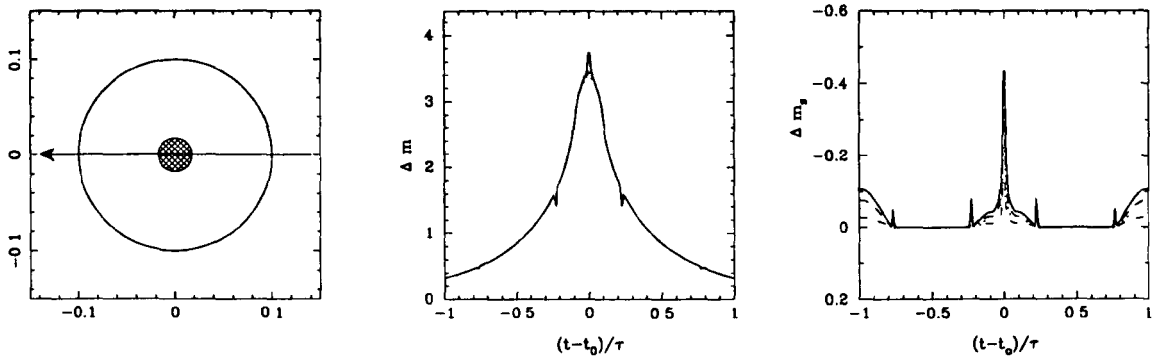

Figure 3.39: The V, R, I and K microlensing light curves produced by the transit of a lens, with minimum impact parameter $u_0 = 0.0AER$, across the disk of a $4000K$ star, of radius $0.1AER$, with $\log g = 1.0$, with a $4800K$ starspot (as shown in the left hand panel) of radius 10° with the source rotating with a period equal to the Einstein radius crossing time. The magnitude changes, Δm and Δm_s are as defined in Equations 3.3 and 3.4.

spot signature indicated by the final panel. The constant offset seen in other examples throughout this Chapter is not present, as for half the event duration the spot is on the back-side of the photosphere and, hence, does not provide a flux during this time. As the source is rotating from left to right as seen in the first panel the period for which the lens is close to the spot is extended. This has the effect of producing a longer spot signature.

In Figure 3.39 an identical configuration is illustrated, however, the lens trajectory has been reversed, i.e. it goes from right to left. This produces a *narowwer* spot signature, as the spot is moving in the opposite direction to the lens and so spends less time close to the lens trajectory. Again the usual constant offset magnitude is not present.

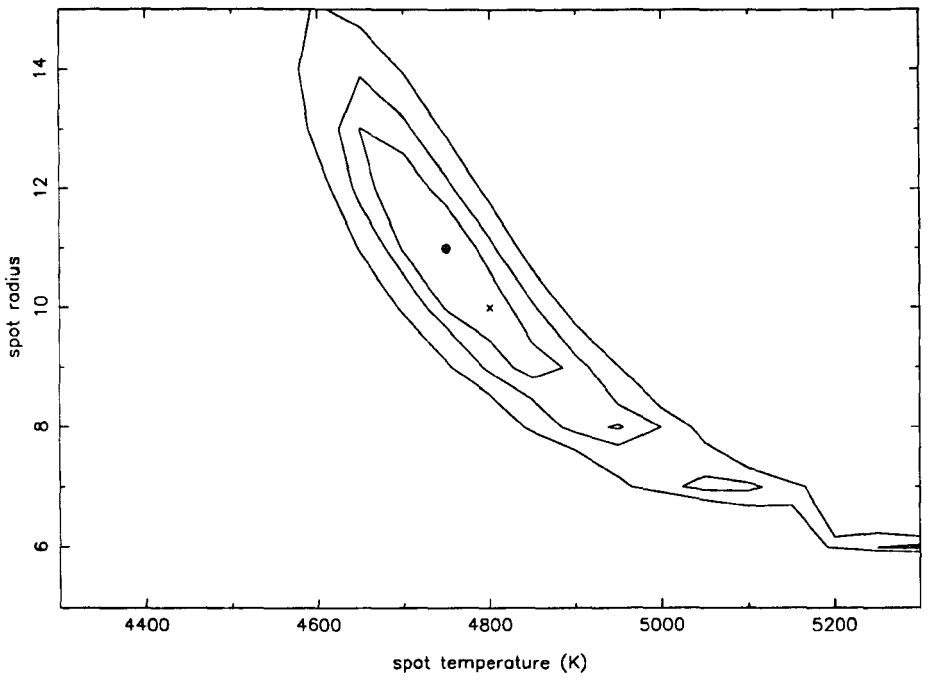

Figure 3.40: The 99%, 90% and 68.3% confidence regions in fitting a grid of spotted lightcurves to the V band lightcurve of a rotating source. The best fitting parameters are indicated by the circle and the correct parameters indicated by the cross.

This broadening or slimming of the spot signature is also present at more modest (i.e. slower) rotation periods. If one considers the case of a period of rotation equal to $10t_E$ and compares the resulting lightcurve to a static source, the bestfitting source will typically overestimate the spot radius for a geometry identical to Figure 3.38. For a spot of 10° radius on the rotating source, the best fitting static source was found to be a slightly cooler 11° radius on the static source. The confidence regions of such a fitting are presented in Figure 3.40 – again showing a "banana" region of suitable spot solutions.

For a geometry such as illustrated in Figure 3.39 the best fitting spot was of radius 9°. Although such biases are, indeed, small, they are yet another example of the difficulties in extracting a 2-d surface brightness profile out of a 1-d lightcurve.

3.6 Conclusions

Microlensing is indeed sensitive to non-radial surface brightness profiles, starspots, providing that the temperature contrast is sufficent and that the starspot is sufficently close

to the lens trajectory and that the lightcurve is well sampled.

It is not anticipated that planetary signatures could potentially be confused with starspot signatures. Starspot signatures occur during the transit portion of the lightcurve rather than predominantly the wings. Furthermore, starspot signatures are strongly chromatic as compared with the achromaticity due to amplification by a planetary caustic. Although for small planetary caustics this may not be the case.

Starspots are more likely to be found by using, say, V band observations than longer wavelengths. The signatures decrease in both magnitude and duration at longer wavelengths.

Whilst it is possible to identify bumps or depressions on microlensing lightcurves that could be due to the presence of starspots, one cannot effectively constrain the 2-dimensional structure of a given spot feature from only a 1-dimensional microlensing light curve. Similar remarks clearly apply to the photosphere as a whole, where groups of (arbitarly shaped) individual spots could mimic the signature of a single, larger, spot and vice versa.

Ultimately, the detection of starspots by microlensing will require high quality dense photometric sampling during transit events. Currently such events are very difficult to alert. The clearest indication of the onset of a transit event is a chromatic signature, which obviously requires a multi-colour monitoring campaign. The simple fact that only one transit event has so far been unambigously found, indicates the difficulties in observing this class of events.

Chapter 4

Imaging stellar photospheres in caustic crossing events

4.1 Background

As discussed both previously and throughout microlensing literature, caustic crossing events are extremely attractive for gravitational imaging for several reasons: Firstly, there is the high levels of magnification which provides not only more flux but also necessitates an extended source treatment for every source. Furthermore the alerting by the source's entry into the caustic has allowed excellent sampling of such lightcurves in recent microlensing events.

A recent treatment of microlensing of star spots during caustic crossing events by Han et al. (2000), concluded that the star spots could indeed be detected. The signatures, however, were only present very close to the crossing, i.e. within a few source radii. This means that the use of the amplification approximation (Equation 1.22) is clearly justifable, as it is with other examinations of stellar atmospheres during caustic crossings. The work of Han et al. (2000) disregarded any limb darkening, in an attempt to isolate the spot signature. However, it is abundantly clear that a treatment for limb darkening would be required as it is now almost routinely being detected. Spot signatures could be suppressed by limb darkening effects and a convincing detection of a spot would certainly

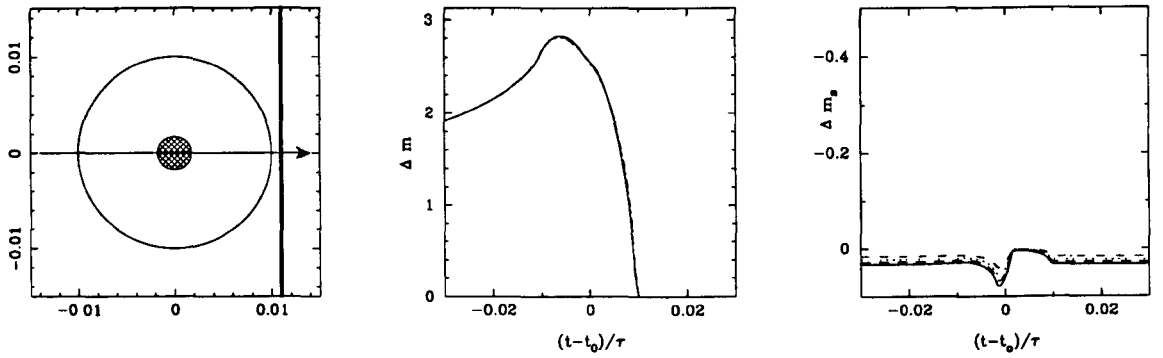

Figure 4.1: The V, R, I and K microlensing light curves produced by the transit of a fold caustic, across the disk of a 5000K star, of radius 0.01AER, with $\log g = 4.0$, with a starspot (as shown in the left hand panel) of radius 10° and effective temperature 4200 K. The magnitude changes, Δm and Δm_s are as defined in Equations 4.1 and 4.2.

require evidence that a more conventional atmosphere model (such as limb darkening) could not produce the same effects. Furthermore, in Han et al. (2000) only a very limited number of parameters were considered and the detectability of a spot at any position on a photosphere was not assessed.

In this Chapter, illustrative examples are presented, showing variations in spot signature, dependent on source and spot parameters. This is followed by discussion on the detectability of such features, in much the same fashion as the previous Chapter.

The effects of limb darkening are incorporated, as in Chapter 3, by the use of the Next Generation stellar atmospheres. In accordance with extended source treatments the amplification is calculated as an integral over the source function using the inverse square root approximation. The chromatic nature of the spot signatures is examined by computation of the lightcurves in 6 colour-bands.

4.2 Illustrative examples

In Figure 4.1 the microlensing lightcurves for a 5000 K, $\log g = 4.0$ source with a cool (4200 K) spot (of radius 10°) are presented in the same manner as in the previous Chapter. The first panel displays the location and size of the spot on the photosphere, the trajectory of the source is indicated by the arrow and the fold caustic by the thick line. In these examples the source is exiting the caustic structure. The middle panel indicates the change,

Δm, in apparent magnitude as a function of time, given by the formula

$$\Delta m = 2.5 \log_{10}(\frac{F_{LSP}}{F_{USP}}) \tag{4.1}$$

where F_{LSP} and F_{USP} denote the flux from the lensed, spotted source and unlensed, spotted source respectively. The final panel on Figure 4.1 shows the change in apparent magnitude, Δm_S, due to the spot, which is given by the formula

$$\Delta m_S = 2.5 \log_{10}(\frac{F_{LSP}}{F_{LSF}}) \tag{4.2}$$

where F_{LSF} is the lensed flux from the spot-free source, which allows us to identify the features in the lightcurves due to the spot rather than the amplification or limb darkening functions.

Four Johnson colour bands, V, R, I and K, are presented in the usual manner, as continuous, dashed, dotted and dash dotted lines respectively.

It can be seen from the final panel of Figure 4.1 that the spot signature produced is very modest. The difference in magnification, between the spotted source and an unspotted source, with otherwise identical parameters, in the V band is only 0.05 magnitudes. We are defining this magnitude change as

$$\Delta m_{max} = 2.5 \log_{10}(\frac{F_{LSP}}{F_{USP}}) - 2.5 \log_{10}(\frac{F_{LSF}}{F_{USF}}). \tag{4.3}$$

The spot signature in Figure 4.1 is, in fact, lower than for a similar source being transited by a point mass lens. This is because at the time of the peak signature the caustic is bi-secting the source and there is a large strip of the photosphere directly underneath the caustic which is diluting the signature from the spot.

It is also worth mentioning that the source radius is, $\rho = 0.01$ AER, in this and the following Figures. A smaller source radius is used in this Chapter as any caustic crossing requires an extended source to model the othewise infinite amplification and so we can

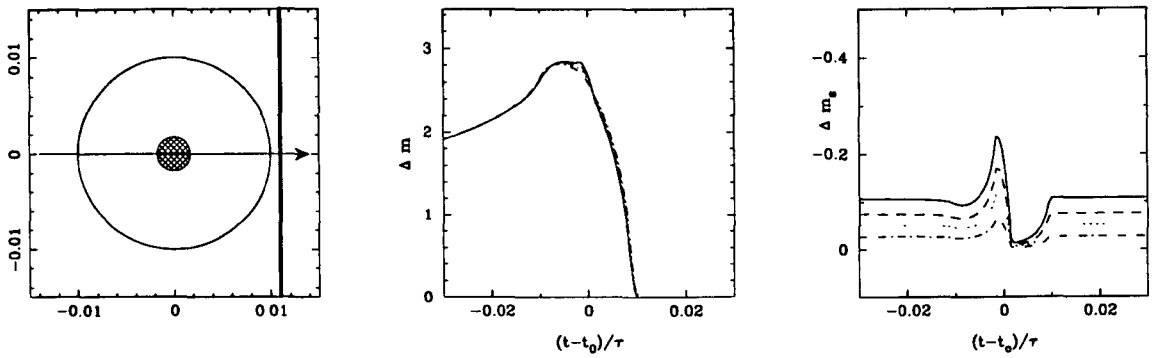

Figure 4.2: The V, R, I and K microlensing light curves produced by the transit of a fold caustic, across the disk of a 4000K star, of radius 0.01AER, with $\log g = 1.0$, with a starspot (as shown in the left hand panel) of radius 10° and effective temperature 4800 K. The magnitude changes, Δm and Δm_s are as defined in Equations 4.1 and 4.2.

choose a smaller source model which is more likely to be prevalent amongst the source population. Recall, from Subsection 1.3.4, that this is equivalent to $5R_{\odot}$ for a *typical* bulge event.

In Figure 4.2 a hot, 4800 K spot on a 4000 K, $\log g = 1.0$ source produces a much more significant magnitude change. In the V colour band the magnitude change reaches 0.13 mags. The chromatic effects, i.e. the spot signature diminishing at longer wavelengths, are also much clearer. This comparison between hot and cold spots is unsurprising considering that the spot signature is still subject to the effects of the differences in surface temperature and hence brightness diminishing at longer wavelengths. The *offset* magnitude change is also larger than in the cool spot case.

However, if one the considers varying the location of the spot, it can be seen that the whether a spot crosses the caustic before or after the majority of photosphere has a significant effect on the spot's microlensing signature. We can see this in Figure 4.3. The spot on the far left of the first panel is the last feature to exit the caustic structure – after most of the photosphere is no longer being amplified by the caustic and produces the largest signal, as shown in the right-hand 'bump' on the final panel. Despite having a smaller effective area the left hand spot produces a larger signal since when it is being imaged the overall flux comes from the region of the photosphere to the left of the spot which is a very much smaller fraction of the stellar disk compared with for the other two spots. Thus the signal from the spot itself makes a larger fractional contribution to the

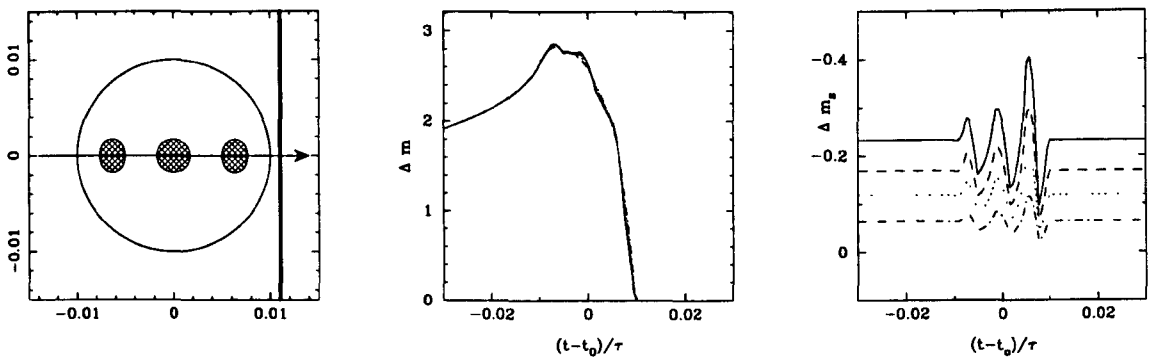

Figure 4.3: The V, R, I and K microlensing light curves produced by the transit of a fold caustic, across the disk of a 4000K star, of radius 0.01AER, with $\log g = 1.0$, with three starspots (as shown in the left hand panel) of radius 10° and effective temperature 4800K. The magnitude changes, Δm and Δm_s are as defined in Equations 4.1 and 4.2.

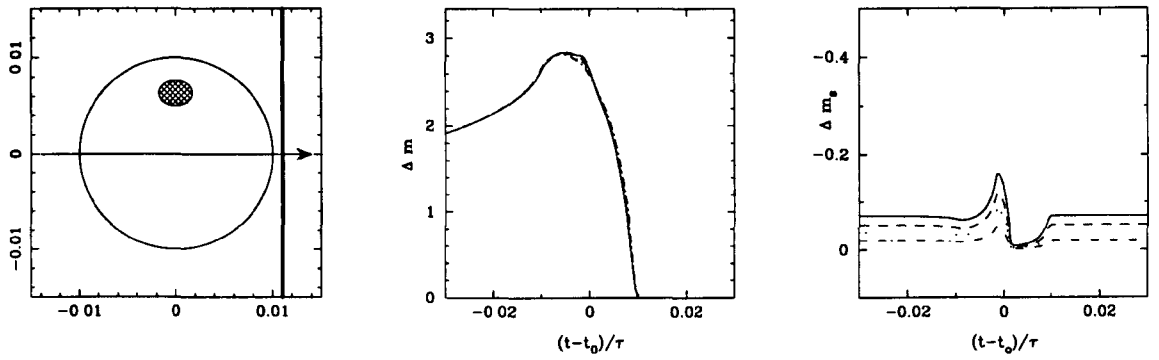

Figure 4.4: The V, R, I and K microlensing light curves produced by the transit of a fold caustic, across the disk of a 4000K star, of radius 0.01AER, with $\log g = 1.0$, with a starspot (as shown in the left hand panel) of radius 10° and effective temperature 4800K at latititude 40°. The magnitude changes, Δm and Δm_s are as defined in Equations 4.1 and 4.2.

lightcurve. This effect was also illustrated in Chapter 2, when it was shown that the trailing limb (in this case the location of the left hand spot) provided the largest difference in flux between opposing stellar atmosphere models.

The *offset* magnitude change in Figure 4.3 is very large, as the three hot spots make a large contribution to the unlensed flux from the source. So it is rather difficult to comment on the shape of each spot signature in turn as they are affected by the offset magnitude due to the presence of the other spots, however, surface temperature variations close to the trailing limb produce, by far, the greatest magnitude changes.

Figure 4.4 illustrates the effect, on the spot signature, of increasing the spot latitude. The peak magnitude change in Figure 4.4 is 0.09 mags, which much more accessible to being

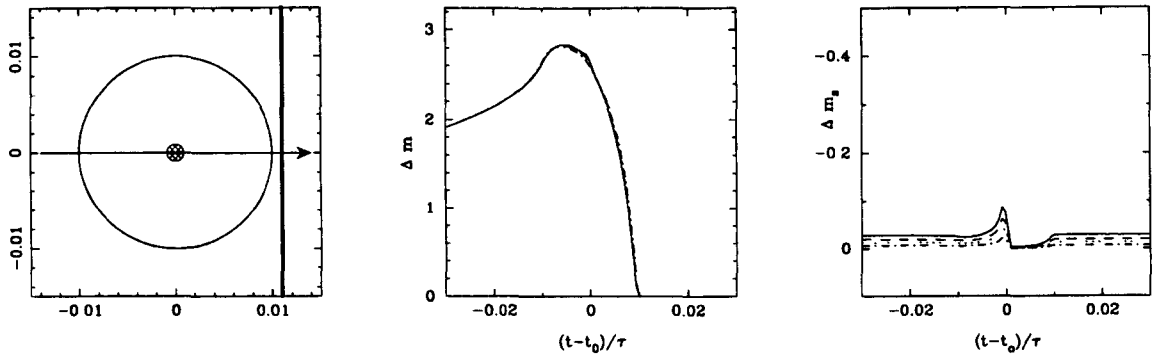

Figure 4.5: The V, R, I and K microlensing light curves produced by the transit of a fold caustic, across the disk of a 4000K star, of radius 0.01AER, with $\log g = 1.0$, with a starspot (as shown in the left hand panel) of radius 5° and effective temperature 4800K. The magnitude changes, Δm and Δm_s are as defined in Equations 4.1 and 4.2.

imaged than a spot at the same location during a point mass zero impact parameter event. This is because the caustic sweeps over *every* feature during the course of the event rather than a just a strip of the photosphere. However, as discussed with reference to the lack of substantial magnitude change with the cool spot example in Figure 4.1, the fact that every element of the photosphere is imaged during the crossing means that the flux from the feature one is hoping to image can also be "washed out" by the overall flux from the rest of the disk. As a spot moves closer to a limb, the signature is still subject to the effects of fore shortening reducing the effect size and limb darkening reducing the temperature contrast, but is still detectable.

In Figure 4.5 the signature from a hot spot of radius 5° is illustrated. It can be seen from the final panel of Figure 4.5 that both the peak magniude change, $\Delta m_{max} = 0.06$ and the timescale of the spot signature are reduced. The timescale is only slightly reduced, the spot can produce a detectable signature not only when the caustic is directly over it but also when close to the feature. The *offset* magnitude change is also lower, however a similar signature could be produced by a larger spot of lower temperature, or, a spot at a higher latitude. These situations will be further examined in Section 4.4.

4.3 Detectability

We have seen that the interplay between the spot temperature and position can conspire to produce similar peak magnitude changes. As we investigate the spot detectability as a function of position we can present the magnitude changes for a variety of spot parameters in a more meaningful way. We wish to identify the regions of a source photosphere where changes in the overall radial surface brightness profile could be identified.

As we are considering caustic crossings we no longer need to consider the effects of varying the impact parameter on the size of the regions of detectability. This allows a greater number of spot parameters, namely temperature and size to be examined in the following section.

The levels of detectability are defined in the same way as Δm_{max}, that at least one data point provides a change in magnitude, of some threshold value, between the lensed and unlensed magnifications. So, in the same way as Chapter 3, we are assesing the areas the of photosphere for which spots can be located which will produce a signature above a given magitude.

In the following plots the lightcurves used to produce the contour maps were calculated for a grid of spot positions over the photosphere. The grey scale at a particular point on the photosphere indicates the photometric precision that would be required to image a spot of the relevant parameters at that position. The lightcurves were all calculated using 20 data points across the crossing portion of the lightcurve and then compared to lightcurves from an identical but unspotted source.

A wide variety of spot parameters, i.e. temperature and radius are examined is this Section – so the magnitude scales do vary between the plots in order to present the results in the most informative way. Additional lower and higher detectablility levels are included when considering the more extreme spot parameters.

In Figure 4.6 the regions of detectability of a 3° radius, 4400 K spot on a 4000 K, $\log g = 1.0$ are presented. The magnitude levels are chosen to show how the signature varies over the

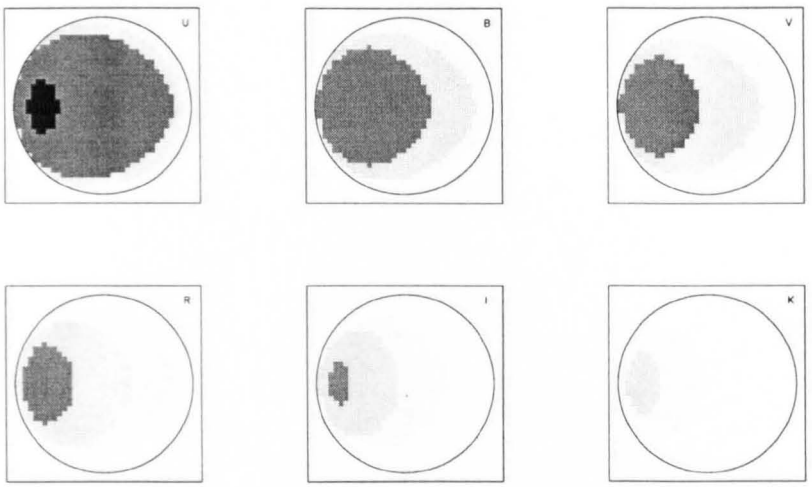

Figure 4.6: The regions of the source photosphere where a 3° radius 4400K spot would provide a 0.005, 0.01 and 0.05 magnitude signature during a microlensing caustic crossing event.

photosphere, although the lowest magnitude level is highly optimistic. One can immediately see that the regions of detectability lie on the the left hand side of the photosphere. The source we are modelling is moving from left to right and exiting the caustic structure (as with the plots presented in the previous Section). This means that the regions of greatest detectability are on the limb that is last to exit the caustic, i.e. when the amplification is arising only from that limb rather than the majority of the photosphere. There is also evidence of large chromatic differences in the spot signature. In the K colour band only a small area of the photosphere near the trailing limb can produce the lowest magnitude change; this area is very close, in terms of size and position, to the largest magnitude change produced in the U band.

Spots closer to the top or bottom limb do not produce detectable signals, their signature is affected by foreshortening and limb darkening but most crucially the fact that as the caustic transits them, it is also amplifying a great deal of the photosphere, which then dilutes the spot signature. Whilst spots close to the centre but on the left hand side hemisphere of the source are not as sensitive to the geometric effects, nor limb darkening, they also fail to provide detectable signals as the overall amplification is too high as the caustic crosses them. This effect is quite different to the "lung" shapes produced by a similar treatment of spot detectability for point mass lenses.

In Figure 4.7 the detectability regions due to the presence of a spot of larger radius (6°) are presented. As this spot produces larger signals the levels of detectability have been

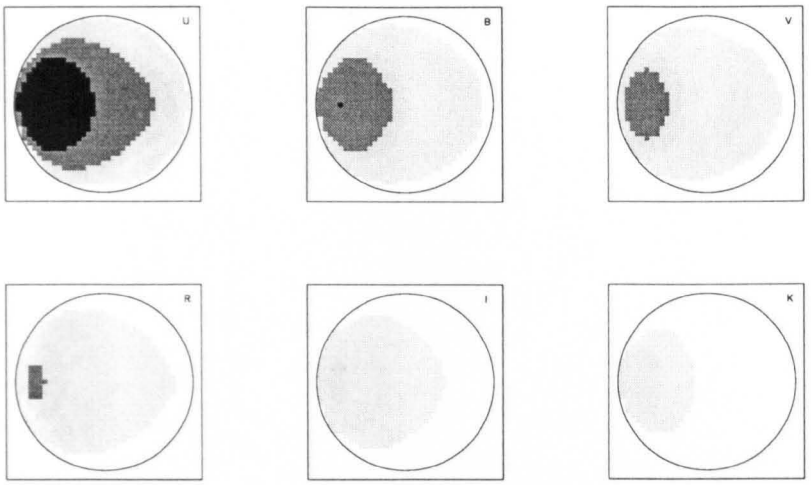

Figure 4.7: The regions of the source photosphere where a 6° radius 4400 K spot would provide a 0.01, 0.05 and 0.1 magnitude signature during a microlensing caustic crossing event.

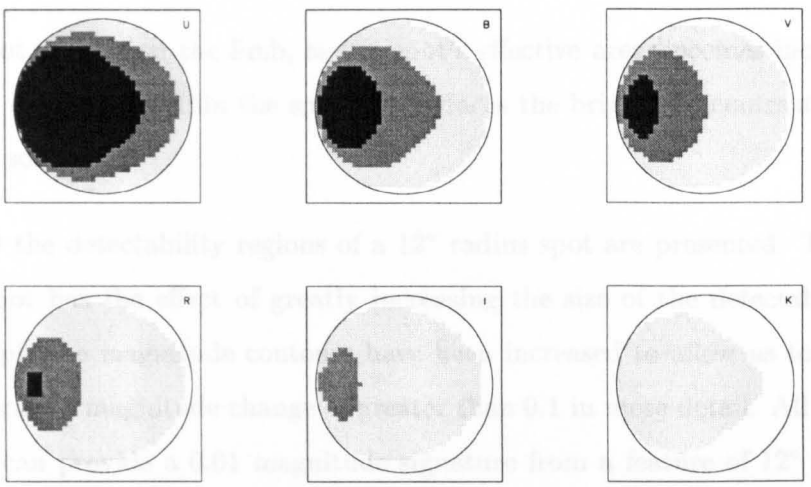

Figure 4.8: The regions of the source photosphere where a 9° radius 4400 K spot would provide a 0.01, 0.05 and 0.1 magnitude signature during a microlensing caustic crossing event.

increased to 0.01, 0.05 and 0.1 magnitudes. The largest magnitude change only occurs on or close to the trailing limb. The signatures are, again, highly chromatic.

In Figure 4.8 the detectability regions due to 9° radius spot are presented. Unsurprisingly, the regions of detectability are larger in Figure 4.8 than for a smaller spot of the same temperature contrast as illustrated in Figure 4.7. The chromatic effects and the larger magnitude changes at the limb are retained. In the V colour band panel of Figure 4.8 it can be seen that whilst the region of peak magnitude change is on the left hand side limb it does not extend completely to the limb. This feature is, actually, repeated throughout this study and is evident in many of the panels. It is, of course, due to the difficulties of

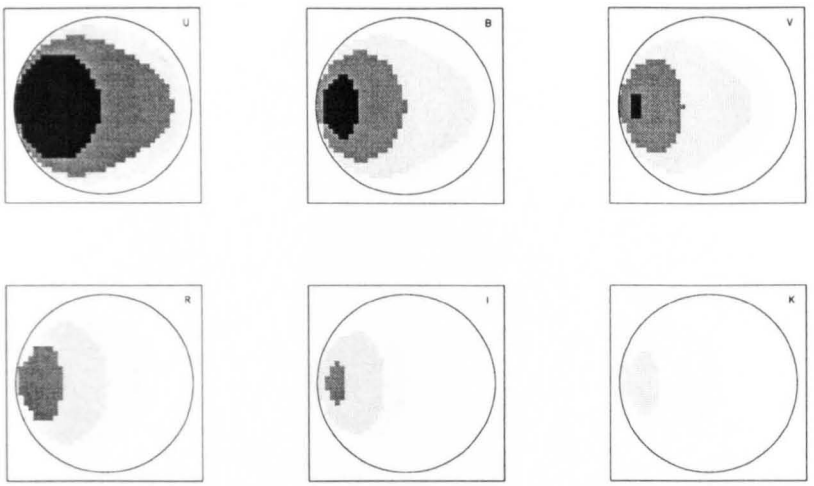

Figure 4.9: The regions of the source photosphere where a 12° radius 4400 K spot would provide a 0.05, 0.1 and 0.2 magnitude signature during a microlensing caustic crossing event.

imaging a spot *exactly* on the limb, as the spot's effective area becomes increasing small and the limb darkening within the spot also reduces the brightness contrast between the spot and the source.

In Figure 4.9 the detectability regions of a 12° radius spot are presented. The increased size of the spot has the effect of greatly increasing the size of the detectability regions. In this example the magnitude contours have been increased to allow us to examine the region producing a magnitude change of greater than 0.1 in more detail. All of the source photosphere can provide a 0.01 magnitude signature from a feature of 12° radius at the temperature of 4400 K – bar only the limb regions in the K colour band. Whilst the greatest magnitude change of 0.2 magnitudes is only present close to the trailing limb in the U, B and V colour bands it is eminently detectable. These results mean that it is possible to say that any spot of temperature contrast of at least +400 K and of radius $\geq 12°$ will be detectable during a caustic crossing event if the sampling rate is equivalent to twenty observations during the transit with a photometric precision of 0.01 magnitudes.

In Figures 4.10, 4.11 and 4.12 the detectability regions for a 4800 K spot of radius 3°, 6° and 9° are presented. Again the magnitude scale differs between these Figures. In Figure 4.10 the magnitudes 0.01, 0.05 and 0.1 provide an adequate discriminant between the regions of detectability. However in Figures 4.11 and 4.12, the higher scale of 0.05, 0.1 and 0.2 is again introduced as a great deal of the photosphere is capable of producing a 0.1 magnitude change. Again we witness the chromatic effects and the acute resolution of

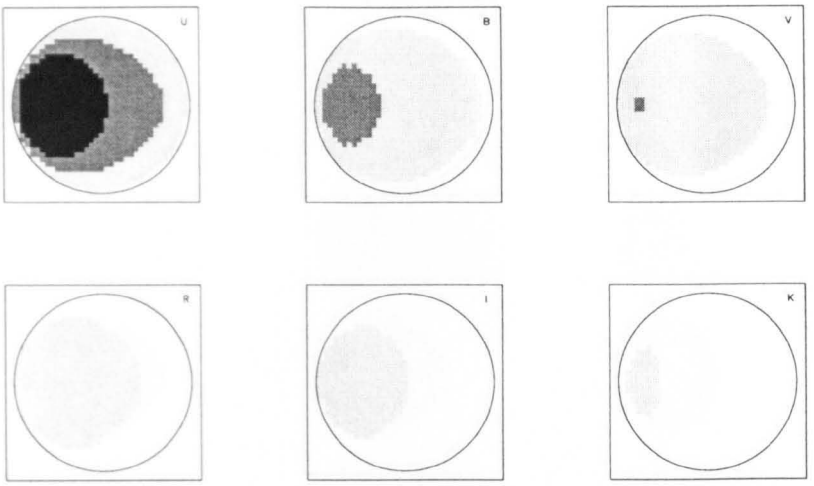

Figure 4.10: The regions of the source photosphere where a 3° radius 4800 K spot would provide a 0.01, 0.05 and 0.1 magnitude signature during a microlensing caustic crossing event.

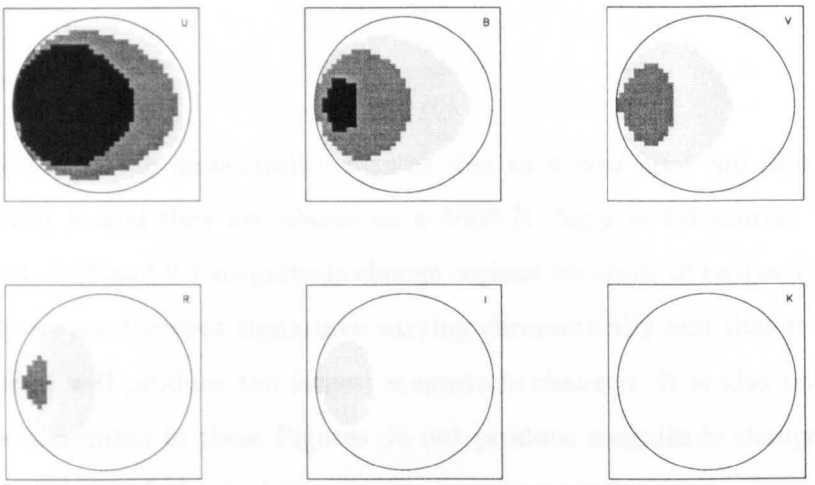

Figure 4.11: The regions of the source photosphere where a 6° radius 4800 K spot would provide a 0.05, 0.01 and 0.2 magnitude signature during a microlensing caustic crossing event.

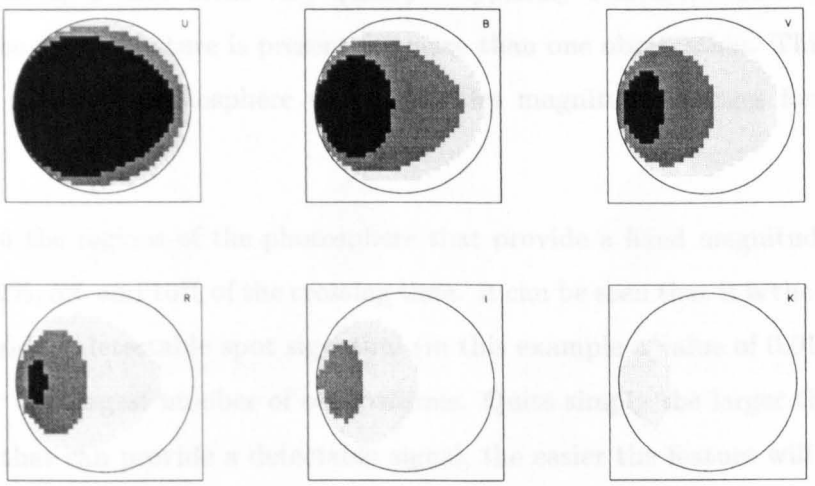

Figure 4.12: The regions of the source photosphere where a 9° radius 4800 K spot would provide a 0.05, 0.1 and 0.2 magnitude signature during a microlensing caustic crossing event.

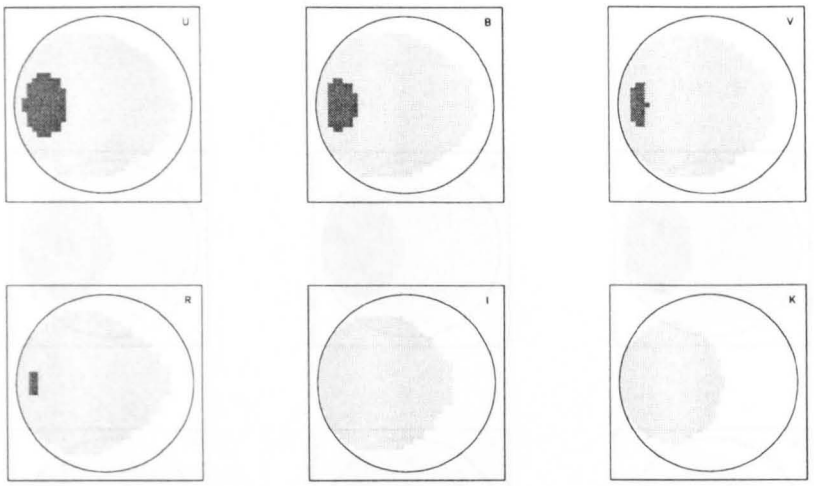

Figure 4.13: The regions of the source photosphere where a 6° radius 4200 K spot on a 5000 K, $\log g = 1.0$ source would provide a 0.01, 0.05 and 0.1 magnitude signature during a microlensing caustic crossing event.

the trailing limb.

In Figures 4.13, 4.14 the detectability regions due to a *cool* spot are illustrated. The spots are of 4200 K and they are placed on a 5000 K, $\log g = 4.0$ source. The Figures present the 0.01, 0.05 and 0.1 magnitude change regions for spots of radius 3°, 9° and 12°. Unsurprisingly we see the spot signatures varying chromatically and that it spots on the trailing limb that will produce the largest magnitude changes. It is also noticeable that the cool spots illustrated in these Figures do not produce magnitude changes as large of those due to hot spots of identical size and temperature contrast.

As caustic crossing events occur very quickly – typically over a few hours, we want to ensure that the spot signature is present for more than one observation. This also allows us to isolate region of photosphere which provides magnitude changes for the longest timescale.

In Figure 4.16 the regions of the photosphere that provide a fixed magnitude change for greater than 2%, 5% and 10% of the crossing time. It can be seen that it is the trailing limb that will provide a detectable spot signature (in this example a value of 0.01 magnitudes was used) for the largest number of observations. Quite simply the larger the number of observations that can provide a detectable signal, the easier the feature will be to detect and the more convincing that detection will be. Figure 4.16 was produced by modelling a

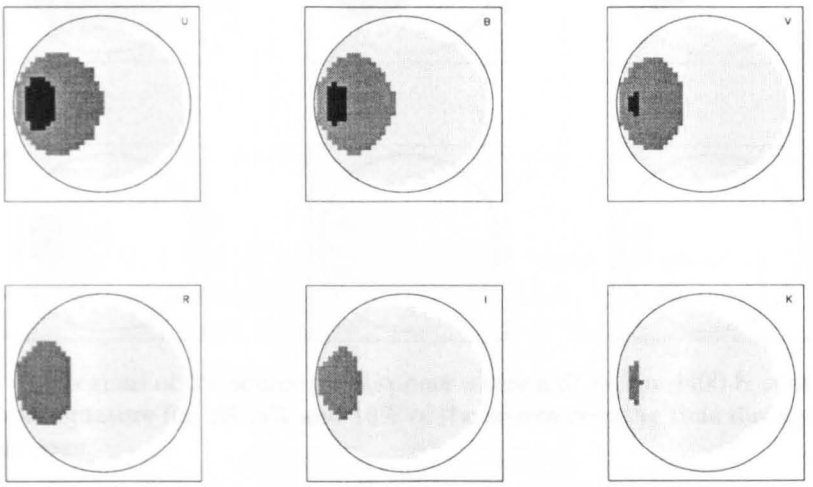

Figure 4.14: The regions of the source photosphere where a 9° radius 4200 K spot on a 5000 K, $\log g = 1.0$ source would provide a 0.01, 0.05 and 0.1 magnitude signature during a microlensing caustic crossing event.

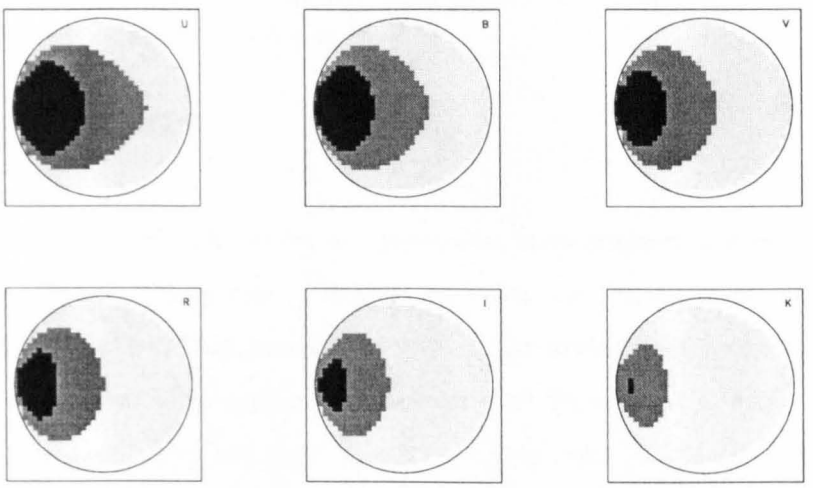

Figure 4.15: The regions of the source photosphere where a 12° radius 4200 K spot on a 5000 K, $\log g = 1.0$ source would provide a 0.01, 0.05 and 0.1 magnitude signature during a microlensing caustic crossing event.

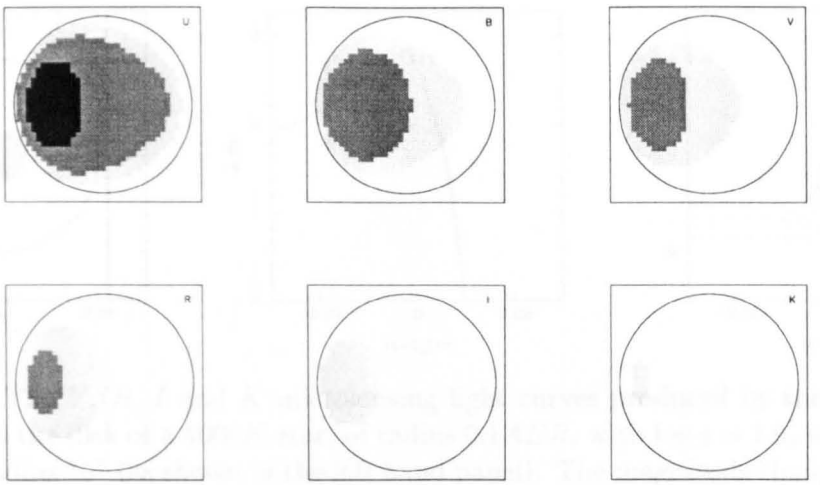

Figure 4.16: The regions of the source photosphere where a 6° radius 4400 K spot would provide a 0.01 magnitude signature for 2% ,5% and 10% of the source crossing time during a microlensing caustic crossing event.

series of lightcurves for a 6° radius, 4400 K spot at every location on the source photosphere of $logg = 1.0$ and 4000 K: however these lightcurves were also very densely sampled at a rate of 100 observations during the transit itself. The duration of the detectable magnitude change is greatly reduced at longer wavelengths. At longer wavelengths the signature is not only reduced in magnitude but also in breadth.

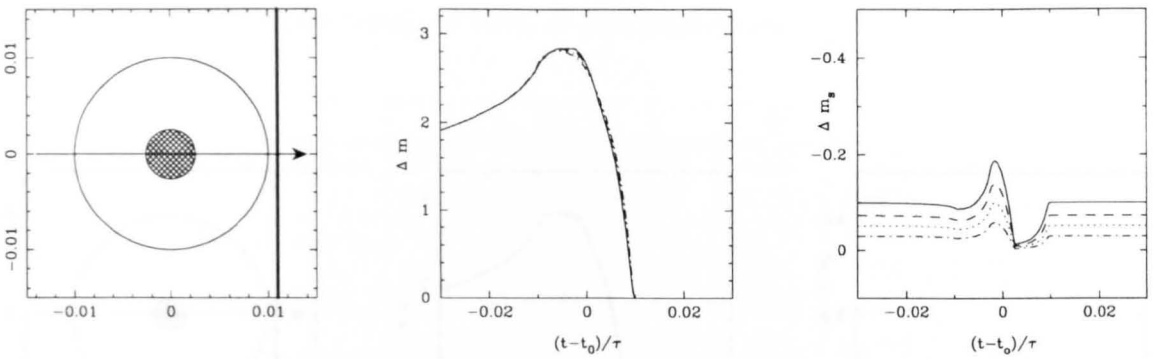

Figure 4.17: The V, R, I and K microlensing light curves produced by the transit of a caustic across the disk of a $4000K$ star, of radius $0.1AER$, with $\log g = 1.0$, with a $4300K$ starspot of radius 15° (as shown in the left hand panel). The magnitude changes, Δm and Δm_s are as defined in Equations 4.1 and 4.2.

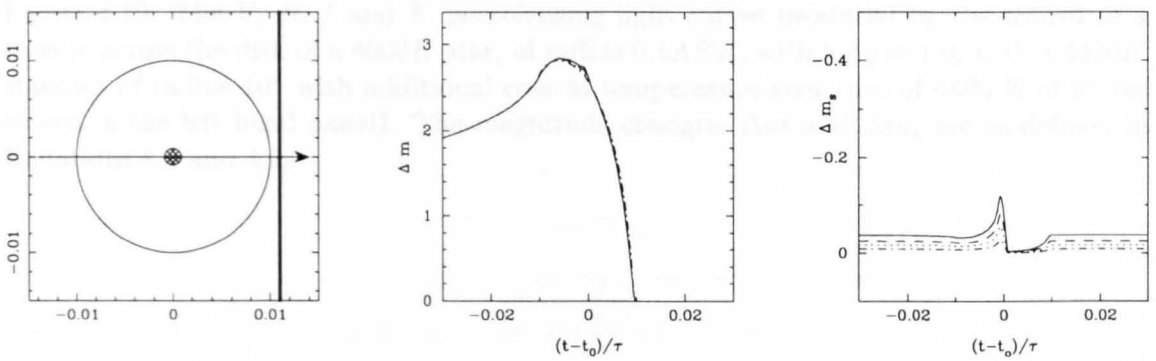

Figure 4.18: The V, R, I and K microlensing light curves produced by the transit of a caustic across the disk of a $4000K$ star, of radius $0.1AER$, with $\log g = 1.0$, with a $5000K$ starspot of radius 5° (as shown in the left hand panel). The magnitude changes, Δm and Δm_s are as defined in Equations 4.1 and 4.2.

4.4 Complications

In this Section, 4 sets of lightcurves are presented from spotted sources, undergoing a caustic crossing event. This group of lightcurves is intended to illustrate that a variation in the spot configuration of the lensed source does not always produce a variation in the microlensing lightcurve. The lightcurves presented in Figures 4.17, 4.18, 4.19 and 4.20 represent, a large (not very) hot spot, a smaller hotter spot, a hot spot with additional temperature structure and a group of small spots, respectively.

The spot signatures from Figures 4.17, 4.18, 4.19 and 4.20 are compared in Table 4.1 in terms of the peak magnitude change due to the presence of the spot(s) and the percentage, t_s, of the evaluated portion of the lightcurve (i.e. 3 source diameters) for which the spot

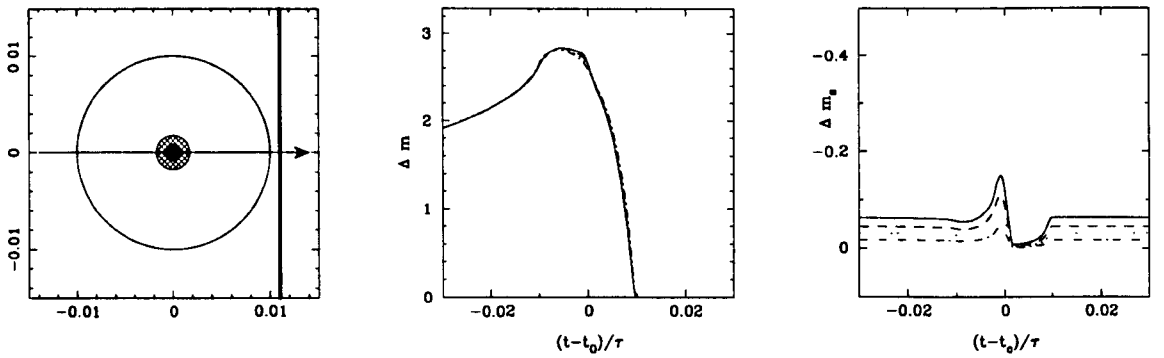

Figure 4.19: The V, R, I and K microlensing light curves produced by the transit of a caustic across the disk of a $4000K$ star, of radius $0.1AER$, with $\log g = 1.0$, with a $4400K$ starspot of radius 10° with additional central temperature structure of 4800 K of 5° (as shown in the left hand panel). The magnitude changes, Δm and Δm_s are as defined in Equations 4.1 and 4.2.

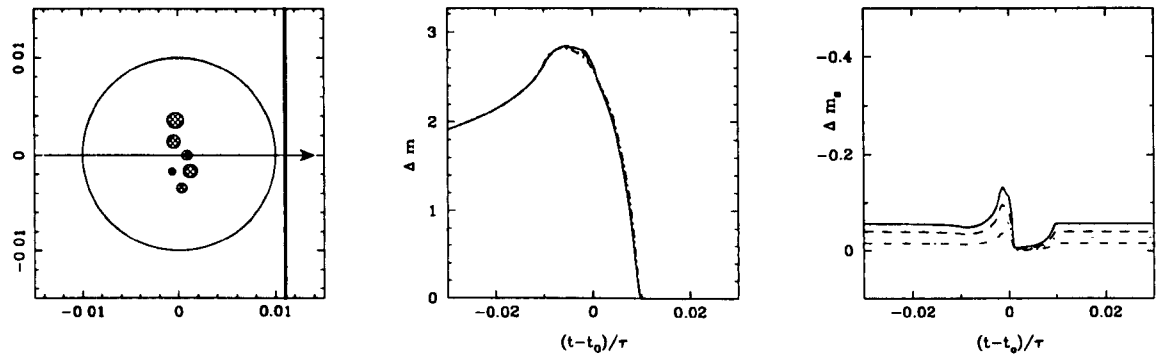

Figure 4.20: The V, R, I and K microlensing light curves produced by the transit of a caustic across the disk of a $4000K$ star, of radius $0.1AER$, with $\log g = 1.0$, with six $4400K$ starspots of varying radius (as shown in the left hand panel). The magnitude changes, Δm and Δm_s are as defined in Equations 4.1 and 4.2.

signature is higher than a threshold value of 0.01 magnitudes.

		U	B	V	R	I	K
Figure 4.17	Δm_s	0.189	0.093	0.066	0.050	0.037	0.022
	t_s	35.5%	27.5%	23%	21.5%	20.5%	17%
Figure 4.18	Δm_s	0.397	0.145	0.082	0.057	0.039	0.019
	t_s	37.5%	23.5%	20.5%	19%	17%	2.5%
Figure 4.19	Δm_s	0.318	0.138	0.088	0.065	0.046	0.025
	t_s	37.5%	27.5%	22%	21%	19.5%	16%
Figure 4.20	Δm_s	0.254	0.114	0.076	0.055	0.040	0.022
	t_s	35.5%	27%	22.5%	21.5%	20%	16%

Table 4.1: Comparison of 4 similar microlensing lightcurves produced by differing spot models as illustrated in indicated Figures, in terms of the magnitude and duration of the spot signature, in 6 colour bands.

In Table 4.1, we can see the spot signatures decreasing at longer wavelengths, as would be anticipated. These signatures are certainly all comparable, however, there are two points that could be made in relation to identifying spot solutions; firstly, the *offset* varies between the models, and is highest for the large cool spot and secondly, the signature decreases at longer wavelengths most quickly for the hottest spots.

In Section 3.5 it was shown that the most plausible spot solutions for a given lightcurve could produce either larger spot radii at cooler effective temperatures *or* smaller spot radii at hotter effective temperatures, this is also true of the signatures presented above. The consideration of the spot's latitude also becomes of some interest. In Section 3.4.3 it was shown that the detectability region of a spot during a point caustic transit is a strip, above, however, we saw that much more of the photosphere was accessible to gravitational imaging, meaning that spots at varying latitudes can produce similar spot signatures.

We have not considered the effects of rotation on the spot signature in the case of fold caustic crossings, as the timescale ($\sim$ few hours) of these crossing is small, as expected timescales would be of the order of months..

4.5 Conclusions

There are undoubtedly better observational prospects for imaging photospheres during caustic crossing events, as the crossing itself is easier to plan for than a point caustic. The differential amplification during the event can be exploited to reveal temperature variations over a great deal of the source, in particular the trailing limb of the source is highly sensitive to the surface brightness profile. A spot close to the limb will produce a larger magnitude change for a longer time than a spot on the leading limb, as the source exits the caustic.

Cool spots are much harder to image – their small signal can be lost against the flux from the source as a whole, whereas the point caustic transits allow acute resolution of a narrow band across the photosphere. The signal from a cool spot can simply get lost due to the increased area undergoing maximum amplification.

We are still susceptible to degeneracy problems discussed in Chapter 3 but with fold caustics it actually becomes harder to constrain a particular spot solution as the signal remains present at a larger range of latitudes.

Chapter 5

Sources undergoing radial oscillations

5.1 Motivation

Although intrinsic variability is adopted as an exclusion criterion by current microlensing surveys, this doesn't preclude the possibility that variable stars themselves may be microlensed.

A study of binary sources in microlensing was made by Griest and Hu (1992), to address the concern that binary source microlensing events may be rejected as background.

In fact there has been very limited success in detecting binary source microlensing events – considering that a naive estimate based on the large numbers of stars in binary systems in the solar neighbourhood might suggest that a considerable fraction of microlensing source stars will belong to binary systems.

Griest and Hu (1992) demonstrated that one would expect to observe "offset dim/bright" events as well as strong asymmetries such as double peaks in the event lightcurves. Orbital motion within the binary system could introduce more exotic lightcurves – although typical timescales and orbital periods make this sub-class of event seem highly improbable.

However these events would still be achromatic (unless of course they occurred with a small impact parameter associated with extended source microlensing).

There exists data from two microlensing events that are not due to static sources.

The event EROS–2 (Ansari et al. 1995) displayed a small level of variability, which was attributed to an eclipsing binary with a period of 2.8 days. However this event recently repeated; making it a pretty dubious microlensing event. A microlensing event could in principle repeat due to a binary lens, but such an analysis of the "double" event has not been published.

There is much better data for the event MACHO 96–SMC–2, (see Alcock et al. 1997)which is more convincing candidate as a binary system source.

Of course many more events may be detected in the future as the microlensing surveys continue – especially as both sampling rates and photometric precision improves.

One reason for the lack of binary source events that has been supplied is that, quite simply, they can easily be fitted to a much simpler point source model with a different blend fraction, Dominik (1998).

Could it also be the case that variable source events aren't being detected as they can be adequately modelled by static sources? If such events are being "missed" as we can obtain acceptable fits with classic symmetric achromatic point sources models for the events then are we risking polluting the data set with biased parameters?

The aim of this Chapter is to firstly examine model microlensing lightcurves as produced by a radially ocsillating source and then to examine how these lightcurves may, if at all, effect parameter fitting if they were treated as standard microlensing lightcurves.

5.2 Model

To produce microlensing lightcurves of variable stars we use an extended source treatment. The amplification is calculated in the usual manner, as an integral over the source surface

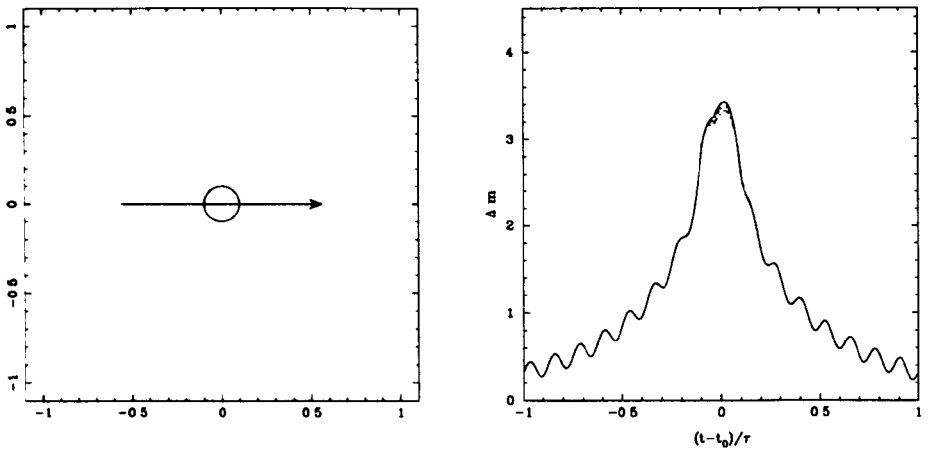

Figure 5.1: The lightcurves produced by a radially oscillating source with $u_0 = 0.0$.

brightness profile. To introduce variability we vary the source radius sinusoidally, so at every timestep during the lightcurve calculation the radius is recalculated before the flux can be found, as throughout this Chapter the flux varies during the microlensing event. For computational ease a linear limb darkening law is used: illustrative lightcurves are presented for situations in which a more sophisticated atmosphere model would normally be desired; however, for the majority of this work we are considering typical impact parameters for which such subtle effects would be undetectable. Whilst this model is simplified, it does allow direct comparisons and general conclusions to be made for generic problem rather than focussing on one particular type of potential variable source stars, such as Cepheid variables.

Figure 5.1 a lightcurve is presented for a lens with zero minimum impact parameter crossing a $0.1AER$ source which varies in radius by 5% sinusoidally 16 times in the portion of the lightcurve shown here. The source has a constant effective temperature of $4000K$ and $\log g = 1.0$. In the usual manner, 4 colour bands, V, R, I and K represented by continuous, dashed, dotted and dash-dotted lines, respectively. Only small chromatic effects are in evidence in Figure 5.1 near the peak of the lightcurve.

This lightcurve can be compared to that produced by a static source, ie a source of constant radius $0.1AER$, $T_{eff} = 4000K$ and $\log g = 1.0$. In Figure 5.2 we present a comparison of these lightcurves with

$$\Delta mag_{variable} - \Delta mag_{static} = 2.5 \log_{10} \frac{F_{LV}}{F_{UV}} - 2.5 \log_{10} \frac{F_{LS}}{F_{US}} \tag{5.1}$$

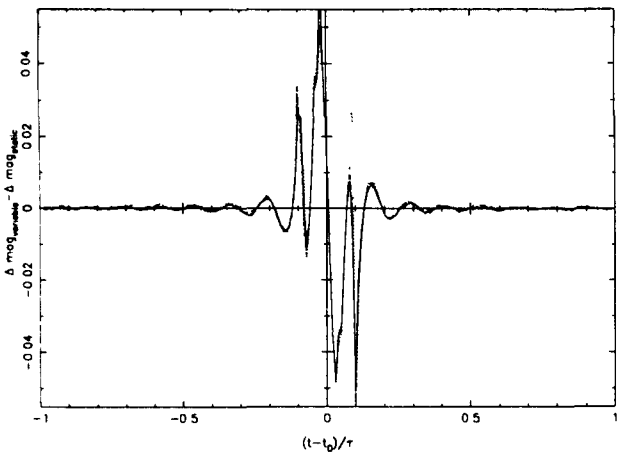

Figure 5.2: Comparison between a static source and radially oscillating source, both with (mean) radius $0.1AER$, $T_{eff} = 4000K$ and $\log g = 1.0$.

where F_{LV}, F_{UV},F_{LS} and F_{US} denote the lensed variable, unlensed variable, lensed static and unlensed static fluxes respectively.

The colour bands chosen for this comparison are again V, R, I and K are in presented in the same way as Figure 5.1. The greatest differences in the magnification between the two models unsurprisingly occur near minimum impact parameter, during the transit stage of the events.

In Figure 5.3 lightcurves from a more sophisticated source with sinusoidally varying temperature are presented. Again at each timestep during the event the temperature is recalculated. This also means that the linear limb darkening law coefficient must be found via a look-up table, at each timestep as this is temperature dependant. The source in this example is again $0.1AER$ and $\log g = 1.0$ for clarity with a mean effective temperature of $4000K$ which varies by 5%. Unsurprisingly the chromatic effects are substantially larger when a varying temperature is considered.

This treatment could be further extended to include variations in the surface gravity ($\log g$); however as this has much more subtle effects on the limb darkening, it does not vary significantly at the modest levels of oscillation considered here. Furthermore as $g = GM/r^2$, a 5% change in radius could not produce a significant change in the surface gravity.

One could, however, hope to relate the peak magnitude change between a static and an

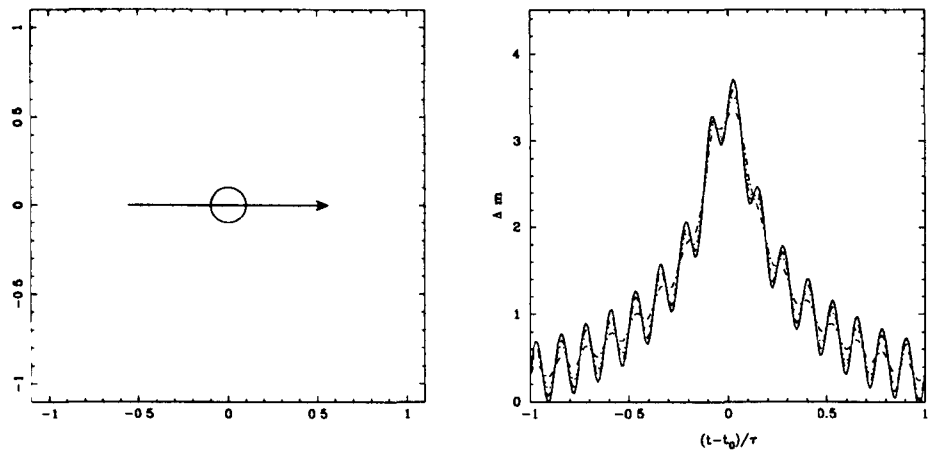

Figure 5.3: The lightcurves produced by a source with varying effective temperature for $u_0 = 0.0$.

oscillating model to the level of oscillation. Equation 5.1 can be used to find the peak magnitude change by examining a series of microlensing lightcurves. Table 5.1 presents the peak magnitude changes for impact parameters of 0.0, 0.05, 0.1 and 0.15 and for changes in stellar radius of 1%, 2%, 3%, 4% and 5% for a source of radius $0.1AER$, $T_{eff} = 4000K$ and $\log g = 1.0$. These results are the V band magnitude changes These peak magnitudes

ΔR	1%	2%	3%	4%	5%
$u_0 = 0.00$	0.024	0.033	0.043	0.053	0.064
$u_0 = 0.05$	0.009	0.014	0.024	0.031	0.039
$u_0 = 0.10$	0.007	0.015	0.023	0.035	0.044
$u_0 = 0.15$	0.001	0.002	0.004	0.005	0.007

Table 5.1: Peak magnitude changes between static and oscillating source microlensing lightcurves.

occur at or very close to minimum impact parameter. In the case of $u_0 = 0.10$, when the lenses grazes the source at its mean radius, the peak magnitude change is larger than a *full* transit (in this case $u_0 = 0.05$) for $\Delta R > 3\%$; in this situation the lensed flux is dominated by the region of the photosphere directly underneath it – in this case it happens to be the region in which the source is expanding in to or contracting out of – so the microlensing is more sensitive, to this essentially limb phenomena, when the minimum impact parameter is close to the limb.

5.3 Comparison to event MACHO–95–30

The event MACHO–95–30 was an extended source transit event. Radial oscillations have been modelled on an event with similar parameters in an attempt to illustrate how simple it would have been to detect any oscillation and that the phenomena discussed in this chapter cannot account for the overall poor χ^2 fit to the event parameters presented in the analysis of the event.

The data was taken at five observatories, in V and R bands only. The source parameters where found fo be, $L = 600 \pm 200 L_{\odot}$, $T_{eff} = 3700 \pm 250 K$, $\log g = 1.0 \pm 0.2$, $R = 61 \pm 12 R_{\odot}$, $D = 9 \pm 1$ kpc and $M \approx 1.0 M_{\odot}$.

The lens parameters were found to be $R_{\rm source} = 0.0756 AER$, $u_0 = 0.054 AER$ with a lens proper motion of $21.5 \pm 2.9 \mathrm{km\,s^{-1}}$ and a Einstein radius crossing time of 33.64 days for the limb darkened source. An extended source treatment reduced the χ^2 statistic for the event by ~ 1000. However the limb darkened source model only improved on this by ~ 9 – leaving a value of ~ 2100 for the final treatment based on ~ 800 observations, see Alcock (1997).

These parameters were applied to a source undergoing radial oscillations. As shown in Figures 5.4, 5.5 and 5.6, any oscillation greater than $\sim 2\%$ would have produced strong enough effects to have been detectable at the modest level of 0.02 mags used in the event analysis.

In Figures 5.4, 5.5 and 5.6 the static source model is shown by a dashed line. It can be seen near the lightcurve peaks, i.e. near maximum light, that the variable models produce asymmetric behaviour in the lightcurve shape, as maximum amplification does not necessarily occur at the maximum of the oscillation. The presence of the radial oscillation is also apparent in the lightcurve wings. In the absence of lensing the magnitude differences with, for example, a 2.5% change in radius can be $\sim \pm 0.05$ mags in the the V colour band. Such variability would have been detected in observations of the source following the event.

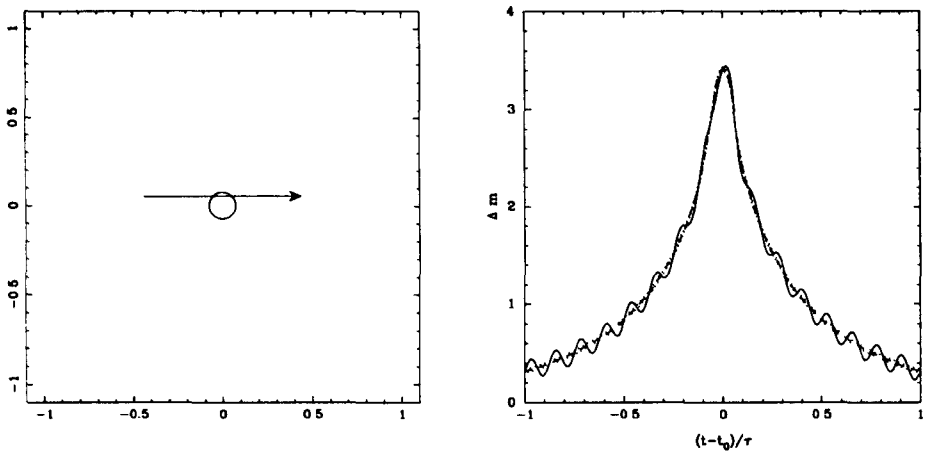

Figure 5.4: The V band lightcurve (solid-line) produced by a source with a 5% variation in radius with 16 cycles completed in the Einstein ring diameter crossing time compared with a similar lightcurve to MACHO–95–30 (dashed line), with errors indicated by dotted lines.

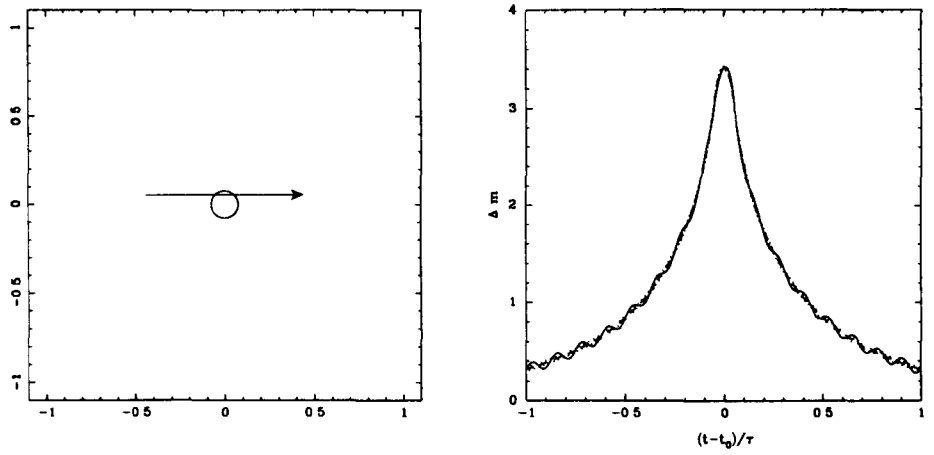

Figure 5.5: The V band lightcurve (solid-line) produced by a source with a 2.5% variation in radius with 16 cycles completed in the Einstein ring diameter crossing time compared with a similar lightcurve to MACHO–95–30 (dashed line), with errors indicated by dotted lines.

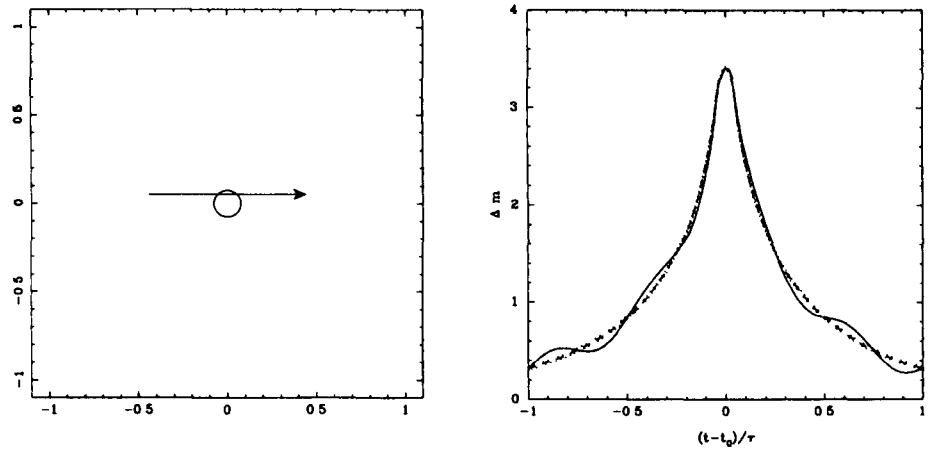

Figure 5.6: The V band lightcurve (solid-line) produced by a source with a 5% variation in radius with 4 cycles completed in the Einstein ring diameter crossing time compared with a similar lightcurve to MACHO–95–30 (dashed line), with errors indicated by dotted lines.

5.4 Parameter fitting

Suppose that the microlensing of a variable source is observed, but the event is modelled as a static point source. It is interesting to consider whether, in this case, the event parameters estimated assuming the static model accurately reflect the true event parameters. In other words, does the failure to correctly model the source as variable result in a bias in the estimated parameters?

To investigate this question we generated variable source lightcurves – again using an extended source treatment – and compared them to a grid of static point source models. The static models were calculated using the point source amplification function

$$A(t) = \frac{u^2+2}{u\sqrt{u^2+4}} \tag{5.2}$$

where,

$$u(t) = \sqrt{u_0 + \frac{(t-t_0)^2}{t_e^2}}. \tag{5.3}$$

and u_0, t_0 and t_E take their usual meanings.

The lightcurves were calculated over a grid of varying impact parameter, u_0, and timescale t_E.

We considered a variable source model with parameters $\rho = 0.05 AER$, $\log g = 1.0$, $T_{eff} = 4000K$ $\Delta\rho = 5\%$ with $u_0 = 0.15$ and $t_E = 50$. We generated a V band lightcurve with $n = 101$ data points, adding to each point a photmetric error drawn from a Gaussian with mean zero and dispersion $\sigma = 0.02$ mags, to give a set of 'observed' magnitudes, $\{m_{obs}(i); i = 1, ..., n\}$. For each one of our grid of static models, we then formed a (reduced) χ^2 statistic given by

$$\chi^2 = \frac{1}{n-2}\sum_{i=1}^{n}\left(\frac{m_{obs}(i) - m_{pred}(i)}{\sigma}\right)^2 \tag{5.4}$$

where $m_{pred}(i) = 2.5 log_{10}(F_{LS}/F_{US})$ is the magnitude change predicted for the i^{th} observation, derived from the ratio of lensed static to the unlensed static flux, for a given pair of values of u_0 and t_E.

The parameters of the best-fitting point source static model were the found by minimising χ^2 in the usual way. Although it is worth mentioning that these calculations are only completely relevant if the uncertainties are gaussian.

In Figure 5.7 the V band microlensing lightcurve from a variable source is shown by continuous line, and the best fitting static point source model (with $\hat{t}_E = 50$ and $\hat{u}_0 = 0.148$ – i.e. a small negative bias in u_0) is shown by a dashed line. These parameters gave a reduced $\chi^2 \simeq 15$, which clearly suggests that the static point source model does not represent an acceptable fit to the variable source data. This is supported by Figure 5.8, which plots the confidence regions for the timescale and impact parameter and shows that the best fit static point source parameters and the true parameters are significantly different at about the 99% level. It seems clear that the poor fit of the variable source V band lightcurve to the static point source model is due much less to the fact that the source is extended and much more to the fact that the source is variable. We can illustrate this as follows. When we generate the V band lightcurve of a static extended source with the same event parameters and fit these data to our grid of static point source models, we obtain the same best fit parameters but now with $\chi^2_{red} = 1.06$, indicating that the point source static model gives a good fit to the data. Thus the poor fit of the variable source is due to its variability, rather than the use of an extended source model. Note, however, that although the goodness of fit is now perfectly acceptable, the small negative bias in the estimated impact parameter is still evident. We can see this in Figure 5.8 where the dashed contours lie very close to the contours of the fit to the variable source data. In other words an extended static source could effectively mimic a static point source with slightly different impact parameter but would otherwise give an acceptable fit to the lightcurve. An extended variable source on the other hand, whilst also mimicking a static point source with a slightly different impact parameter, would be easier to diagnose due to the degradation of the goodness of fit, caused by the variability itself.

The fitting procedure was also applied to B and R band lightcurves and the negative bias in the estimation of the impact parameter also occurred. At the impact parameter under consideration here the chromatic effects are very small and so it is not possible to display several colour bands simultaneously, as they simply overlap.

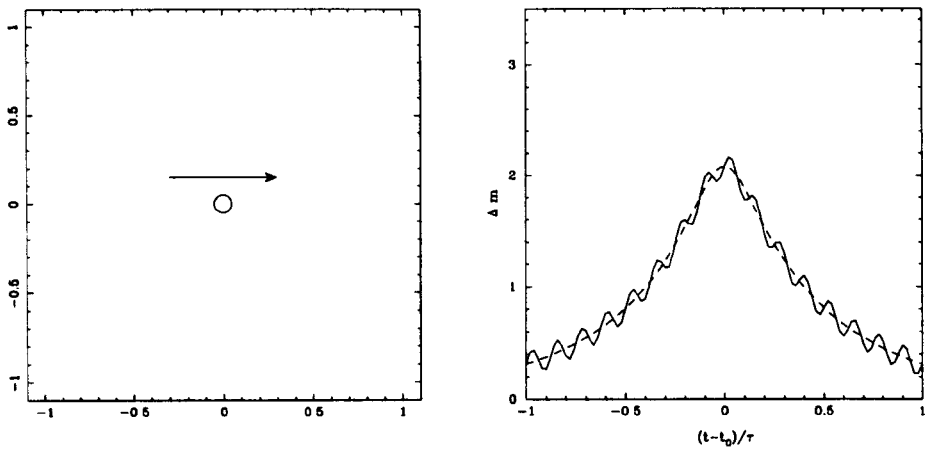

Figure 5.7: The V band lightcurve produced by a radially oscillating source with $u_0 = 0.15$ (continuous line) and the bestfitting static point source (dashed line).

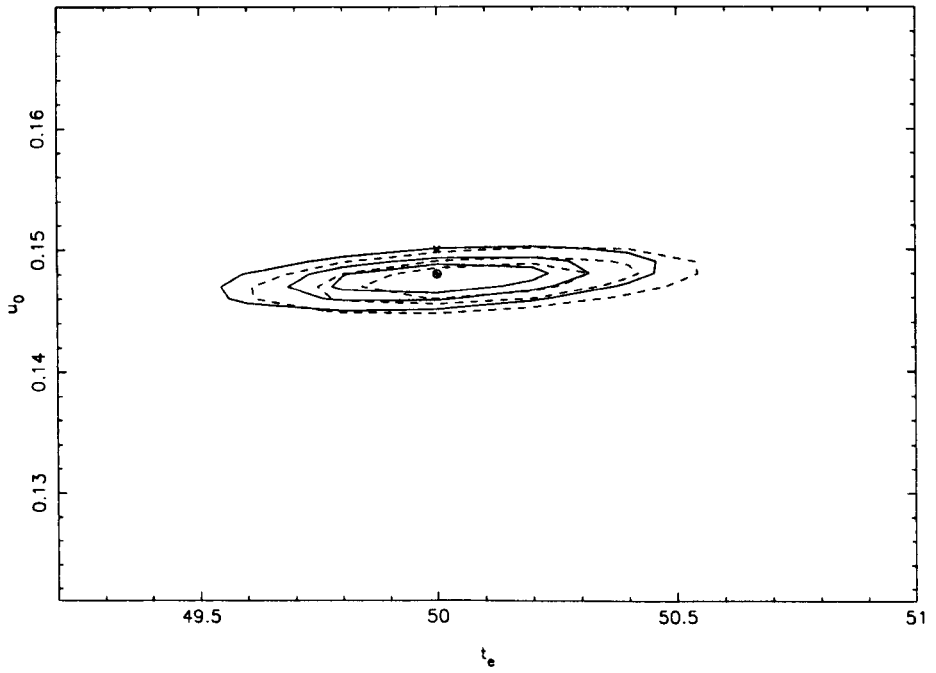

Figure 5.8: The 99%, 90% and 68.3% confidence regions, represented by the continuous line, in fitting a point source to the V band lightcurve illustrated in Figure 5.7. The best fitting parameters are indicated by the circle and the true parameters by the cross. The dashed lines represent the 99%, 90% and 68.3% confidence regions of fitting a static extended source to the point source lightcurves.

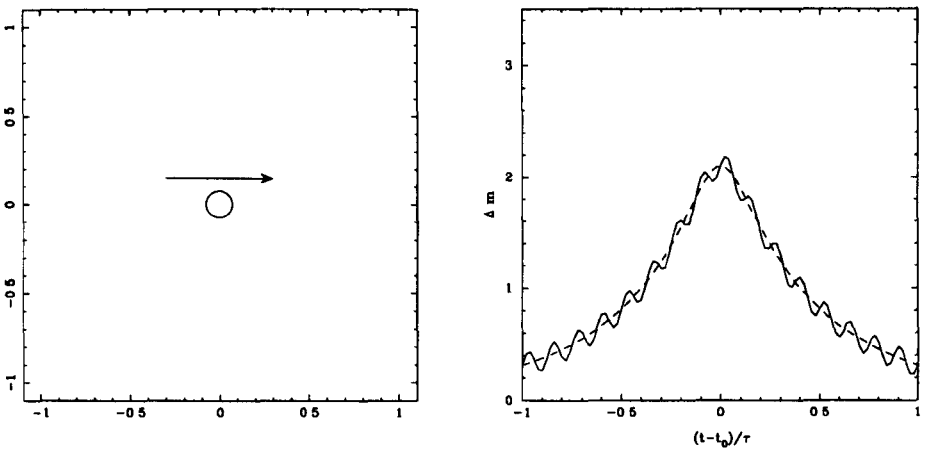

Figure 5.9: The V band lightcurve produced by a radially oscillating source, $\rho = 0.075$ with $u_0 = 0.15$ (continuous line) and the bestfitting static point source (dashed line).

In Figure 5.9 a variable source has again been compared to a grid of static point source models. The true event and source parameters are identical to those of Figure 5.7 – apart from the source radius which is somewhat larger, $\rho = 0.075$ so that $u_0 = 2\rho$. Again we find that the impact parameter is underestimated, with $u_0 = 0.145$ for the best fitting point source model to both the variable and the static extended sources. In a similar manner to the first example, the fit to the extended variable source model provides a reduced $\chi^2 \simeq 15$, compared to the fit to the static extended source with $\chi^2 \simeq 1$.

Figure 5.10 shows the confidence regions for the timescale and impact parameter estimated from fitting the variable extended source data (continous lines) and static extended source data (dashed lines) to the grid of static point source models. Again we see a negative bias in the estimation of the impact parameter; the true value actually lies outside the 99% confidence region in both cases.

We next considered a reduced level of variability such as in Figure 5.11, where the change in source radius is only 2%. Again we obtained the best fit values of the event parameters by fitting the simulated lightcurves to our grid of static point source models. In this case the correct event parameters were found in the three colour-bands examined, other than the impact parameter which was estimated to be $u_0 = 0.147$. As can be seen from Figure 5.11 the smaller change in source radius produces smaller deviations in the microlensing lightcurve from the point source model. Consequently the best fitting point source model provides a $\chi^2 \simeq 3$ in this case, which is greatly improved although still only marginally

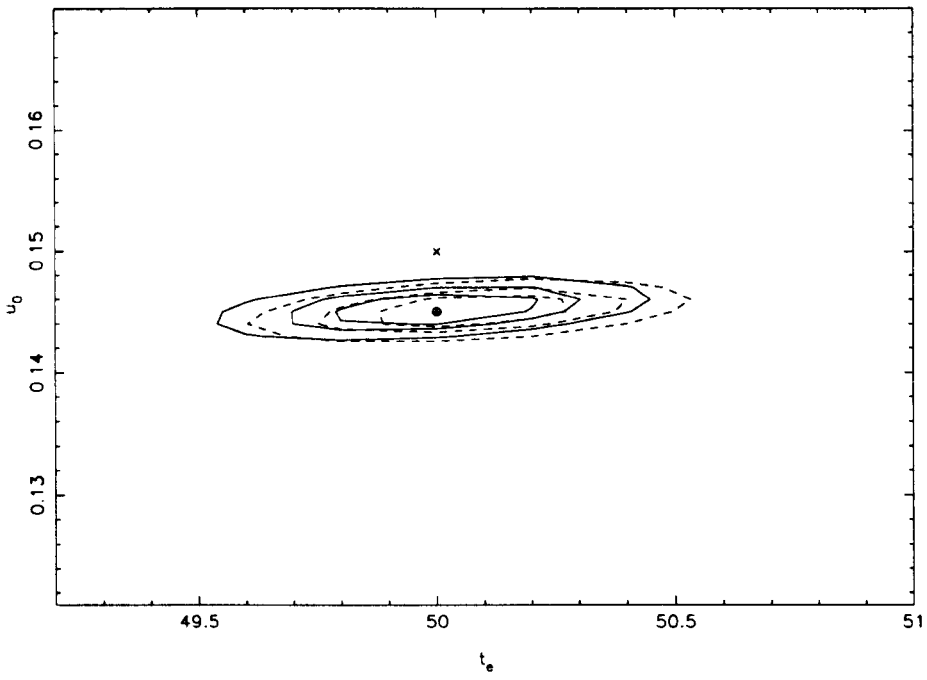

Figure 5.10: The 99%, 90% and 68.3% confidence regions, represented by the continuous line, in fitting a point source to the V band lightcurve illustrated in Figure 5.9. The best fitting parameters are indicated by the circle and the true parameters by the cross. The dashed lines represent the 99%, 90% and 68.3% confidence regions of fitting a static extended source to the point source lightcurves.

acceptable.

In the previous examples, 16 cycles of the variation were completed during the crossing of one Einstein diameter. We contrast this in Figure 5.12 with the case where only 8 complete cycles are presented.

The source parameters are again $\rho = 0.05AER$, $\log g = 1.0$, $T_{eff} = 4000K$ $\Delta\rho = 5\%$ with $u_0 = 0.15$. The event parameters were also again correctly found – with the exception of the underestimation of the impact parameter, $u_0 = 0.148$ – but as before with a $\chi^2 \simeq 15$ indicating an unacceptable fit to the point source static model. Hence with a sufficiently sampled lightcurve even a reduced number of cycles of variation will still result in a unacceptably high goodness of fit.

The inclusion of an extra parameter, the amount of blended light into the fitting procedure as described above, did not influence the calculation. For a 'blend' within the photometric error of the simulated event, it was found that the correct baseline magnitude was found without affecting the other parameters under examination.

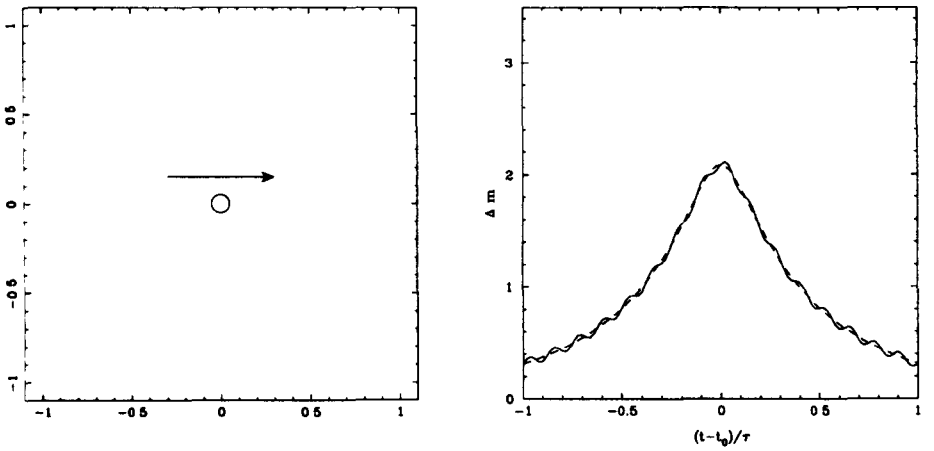

Figure 5.11: The V band lightcurve produced by a radially oscillating source with $u_0 = 0.15$ (continuous line) and the bestfitting static point source (dashed line).

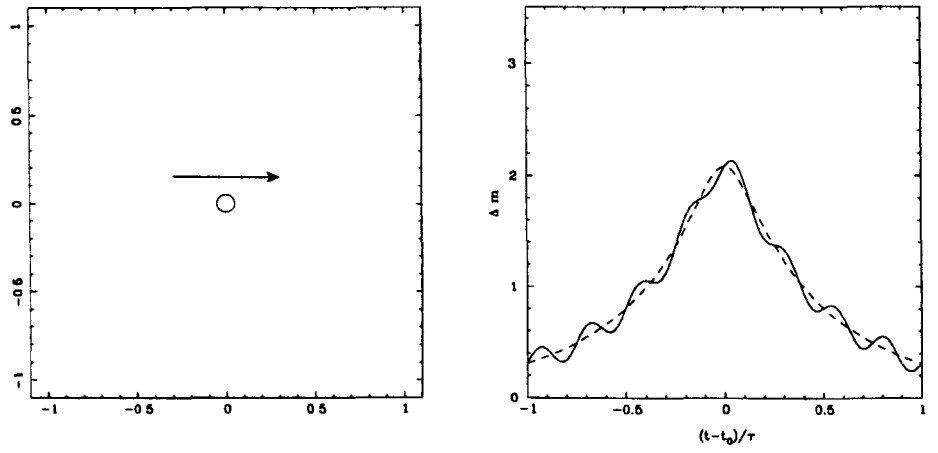

Figure 5.12: The V band lightcurve produced by a radially oscillating source with $u_0 = 0.15$ (continuous line) and the bestfitting static point source (dashed line) with only 8 cycles of the oscillation occuring within the Einstein ring diameter crossing time.

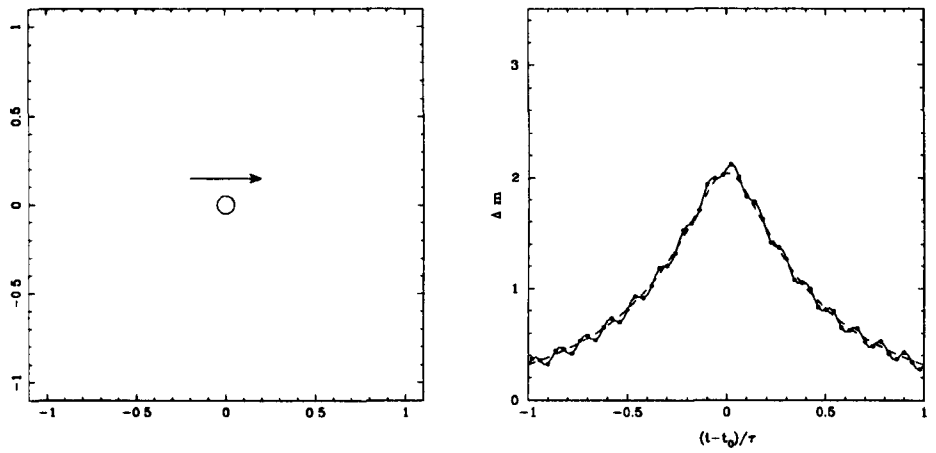

Figure 5.13: The V band lightcurve produced by a radially oscillating source with $u_0 = 0.15$ (continuous line) and the bestfitting static point source (dashed line) using 50 data points.

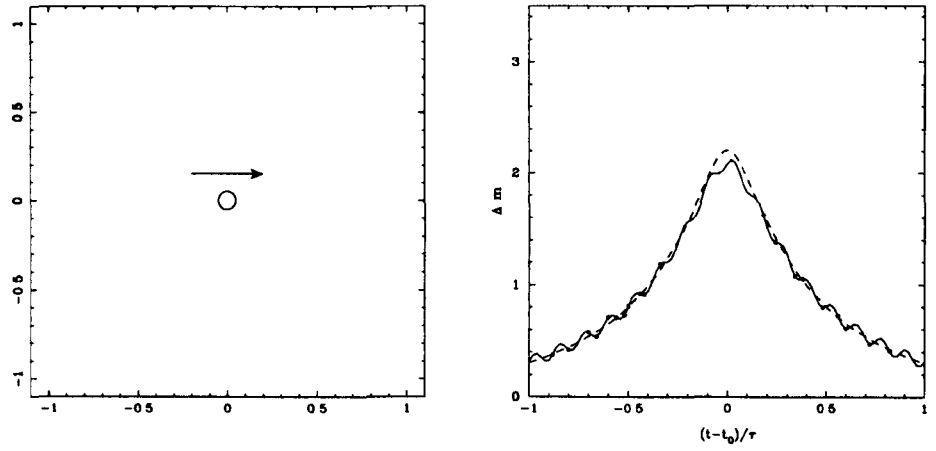

Figure 5.14: The V band lightcurve produced by a radially oscillating source with $u_0 = 0.15$ (continuous line) and the bestfitting static point source (dashed line) using 20 data points in the "wings".

5.4.1 Sampling considerations

The previous fits were all made by comparison with a regularly sampled lightcurve with 101 points. In practise events aren't necessarily regularly sampled, nor is the entire lightcurve always sampled due to the more mudane realities of observing microlensing, such as poor weather conditions.

Four sampling strategies were chosen to allow study of their ability to estimate correctly the event parameters when presented with the unusual events considered in this chapter.

The (rather exaggerated) sampling strategies chosen were,

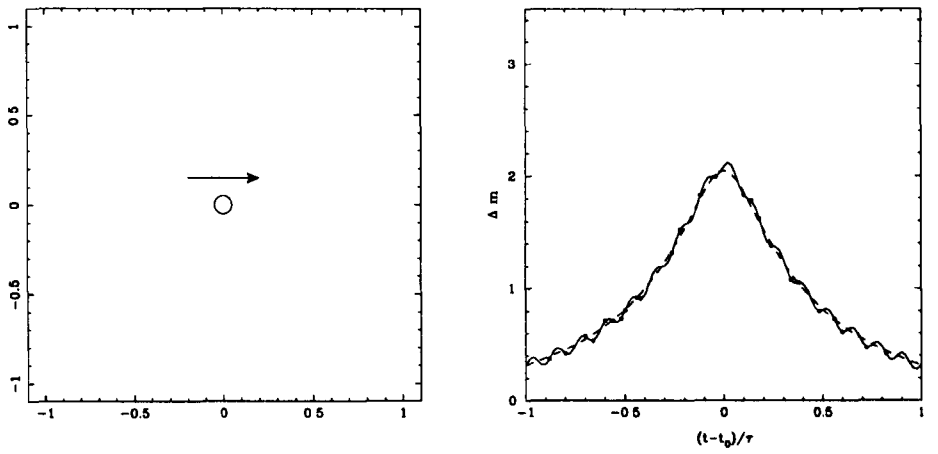

Figure 5.15: The V band lightcurve produced by a radially oscillating source with $u_0 = 0.15$ (continuous line) and the bestfitting static point source (dashed line) using 20 data points in the "wings" plus 5 close to maximum light.

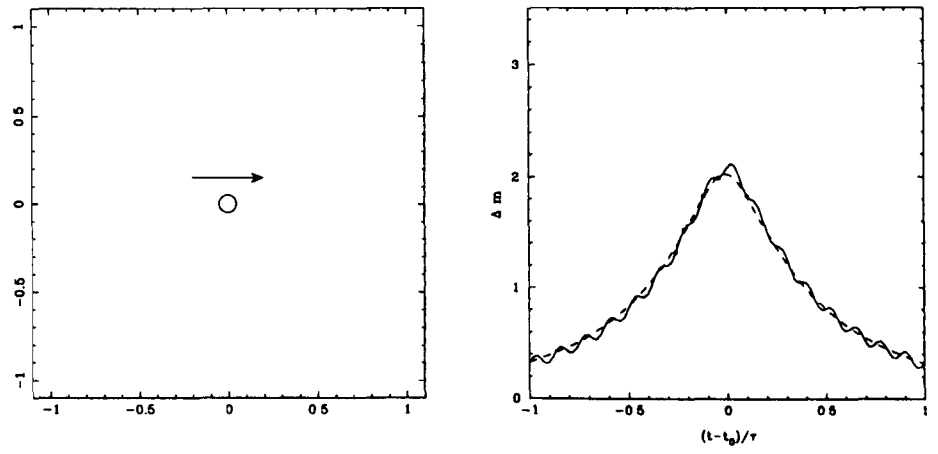

Figure 5.16: The V band lightcurve produced by a radially oscillating source with $u_0 = 0.15$ (continuous line) and the bestfitting static point source (dashed line) using only 5 data points close to maximum light.

1. Using 50 evenly spaced data points
2. Using 20 points mainly in the lightcurve "wings"
3. Using 20 points mainly in the lightcurve "wings", plus 5 points close to maximum light
4. Using only 5 points, close to maximum light

The fitting of data derived from these strategies to static point source models is presented in Figures, 5.13, 5.14, 5.15 and 5.16 in the V band.

In all cases the source is radially oscillating by 2.5%, with 16 cycles in the event.

The fits to the point source parameters are illustrated in Figures 5.17, 5.18, 5.19 and 5.20, where the confidence levels are shown as continuous lines. The confidence levels of fitting point source models to a *static* extended source are illustrated by the dashed lines. The fitting procedure was carried out exactly as previously, but now with a photometric error of 0.05 magnitudes.

These confidence region plots allow us to discuss how poorly sampled microlensing lightcurves may affect parameter fitting to non-static sources. In Figure 5.17 it can be seen that the confidence levels do not differ greatly between the static and the variable sources. This is consistent with the results in the previous Section. Note, however, that the confidence regions are much larger, reflecting both the decrease in the photometric precison and the smaller number of observations. In particular, the timescale is not very well constrained.

In Figure 5.18, which is constructed using only points in the lightcurve wings, we can see that the fitting is considerably poorer for the variable source than for the static case. Both models would lead to a large underestimation of the impact parameter and the timescale, although the formal error on both parameters would be somewhat smaller for the static extended case.

If one then adds to these observations with a few close to maximum light the fit is improved, as is shown in Figure 5.19. Unsurprisingly the fit to the impact parameter is greatly improved by the addition of the observations when the lens is close to the minimum

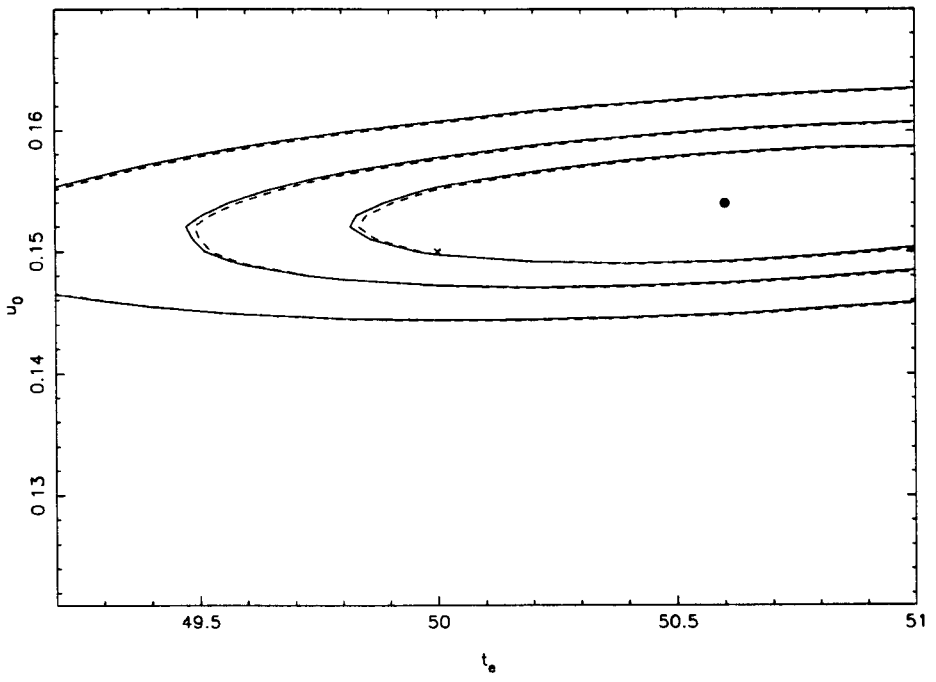

Figure 5.17: The 99%, 90% and 68.3% confidence regions, represented by the continuous line, in fitting a point source to the V band lightcurve illustrated in Figure 5.13. The best fitting parameters are indicated by the circle and the true parameters by the cross. The dashed lines represent the 99%, 90% and 68.3% confidence regions of fitting a static extended source to the point source lightcurves.

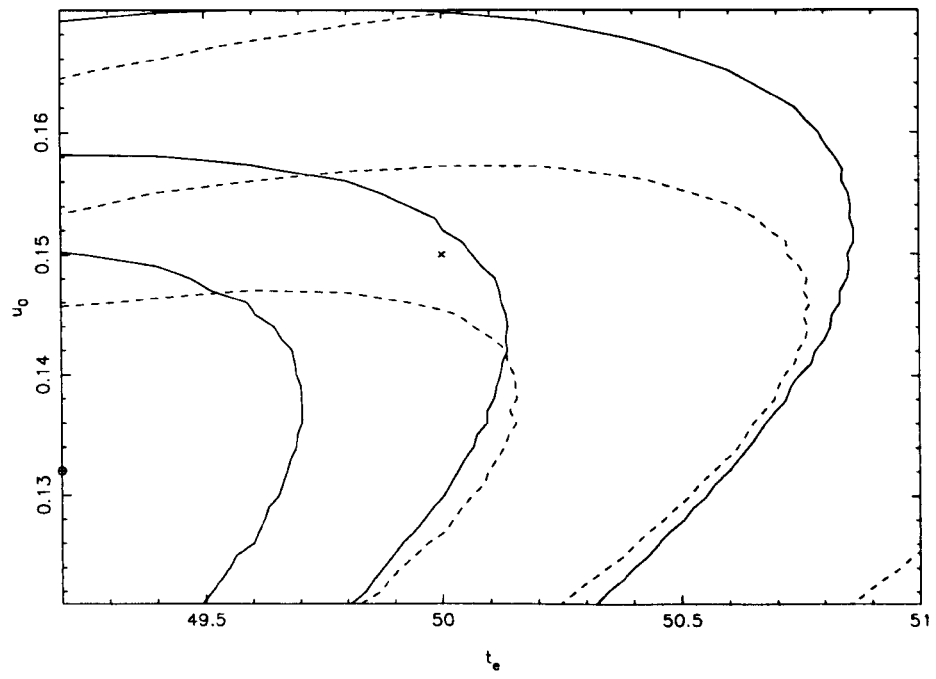

Figure 5.18: The 99%, 90% and 68.3% confidence regions, represented by the continuous line, in fitting a point source to the V band lightcurve illustrated in Figure 5.14. The best fitting parameters are indicated by the circle and the true parameters by the cross. The dashed lines represent the 99%, 90% and 68.3% confidence regions of fitting a static extended source to the point source lightcurves.

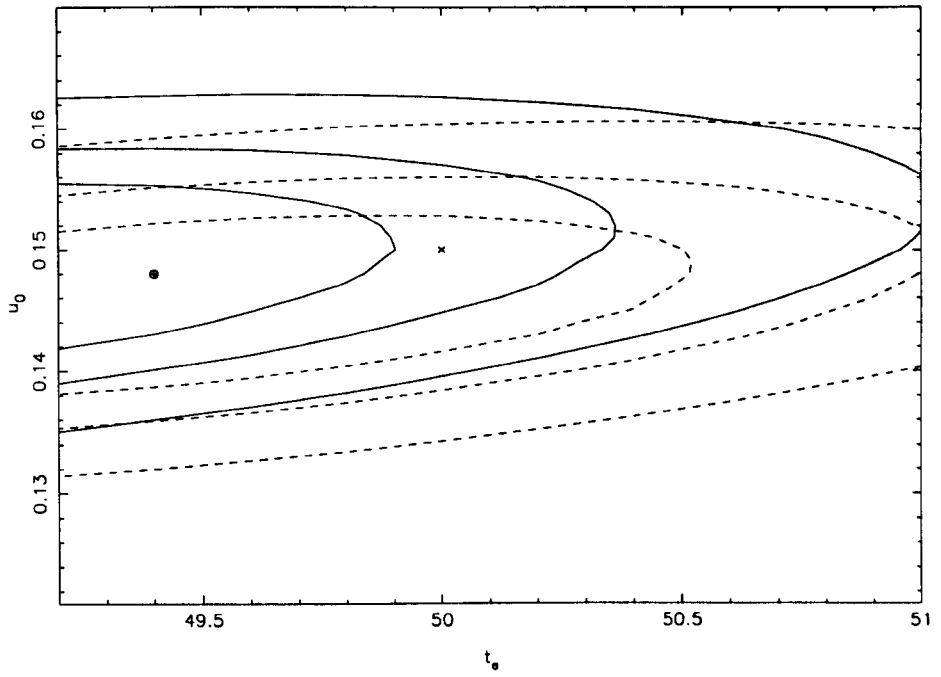

Figure 5.19: The 99%, 90% and 68.3% confidence regions, represented by the continuous line, in fitting a point source to the V band lightcurve illustrated in Figure 5.15. The best fitting parameters are indicated by the circle and the true parameters by the cross. The dashed lines represent the 99%, 90% and 68.3% confidence regions of fitting a static extended source to the point source lightcurves.

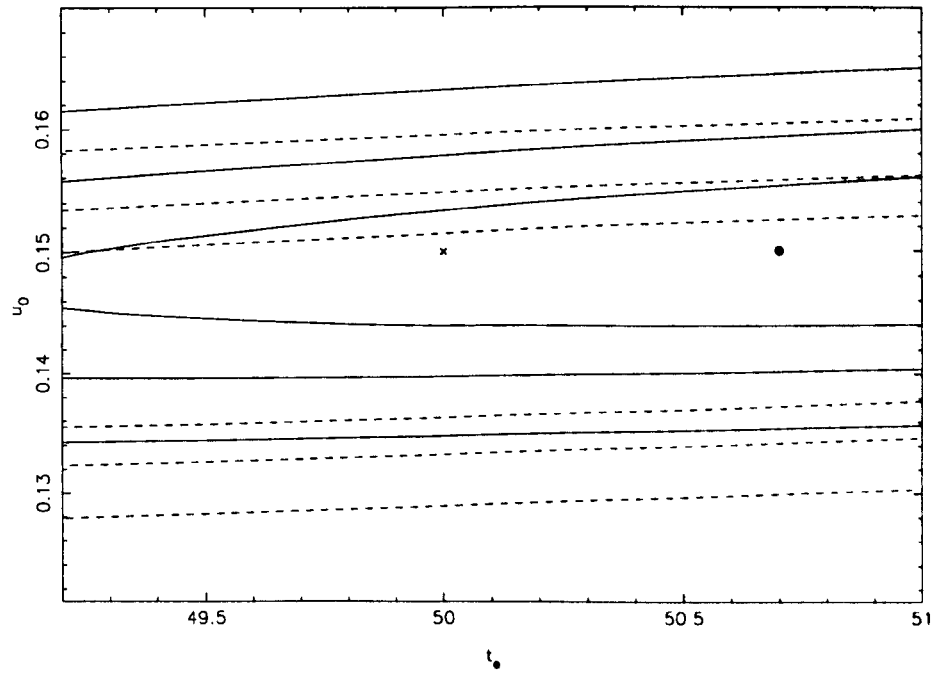

Figure 5.20: The 99%, 90% and 68.3% confidence regions, represented by the continuous line, in fitting a point source to the V band lightcurve illustrated in Figure 5.16. The best fitting parameters are indicated by the circle and the true parameters by the cross. The dashed lines represent the 99%, 90% and 68.3% confidence regions of fitting a static extended source to the point source lightcurves.

impact parameter. Neverthelesss the fitting of the variable source is still clearly inferior to that of the extended static source.

By using only the observations close to maximum light, as shown in Figure 5.20, we can see that the correct impact parameter can be reasonably well constrained, but we have very little information on the timescale of the event as a whole. Also using only the peak points again displays a large difference between the fitting of the static and variable extended sources.

In summary, therefore, it appears that the effects of variable sources on the estimation of event parameters are not too concerning – subject to the caveat that observations of good photometric accuracy are required throughout the event. Firstly, there appears to be little evidence of bias on the determination of the event timescale, unlike in the binary source situation (Griest and Hu 1992). Secondly the negative bias on determining the impact parameter is very small (although significant) and is in any case also found in the static extended source lightcurve fitting procedure. In other words the bias arises from a failure in the point source model rather than a failure to include the variability. Thirdly, in any case, the impact parameter is perhaps not the most important parameter to be determined from a microlensing event. Finally, it is unlikely that a variable extended source event would *not* be correctly identified as a variable source, due to the poor goodness of fit which these events give to a static model. Even if an appropriate baseline flux cannot be found, as was the case in the models considered here, where only the amplification was fitted, it would be abundantly clear from the lightcurve shape that perturbations due to source variability were present.

Chapter 6

Microlensing of circumstellar envelopes

It is clear that sources with a significant angular radius are the most likely to be imaged during a extended source microlensing event. By considering the circumstellar envelope instead of just the stellar photosphere the source radius can be greatly increased, and so too the likelihood of useful extended source effects being observed. Ignace and Hendry (1999) modelled a series of point lens microlensing events in which it was shown that microlensing can provide information on the velocity field within circumstellar envelopes. Such events are discussed below and a similar treatment is then applied to the case of caustic crossing events. The possibilities for using this technique to resolve spectroscopically stellar winds are indeed hopeful as spectroscopic studies of high amplification microlensing events are becoming more common particularly for caustic crossing events. By modelling such events and demonstrating the diagnostic potential of microlensing the aim is to provide motivation for continuing concerted spectroscopic studies of microlensing events. The demonstration that information on the velocity field in stellar winds is accessible by studying microlensing events in progress is hoped to be of great interest to the microlensing community as a whole. The very high amplification events due to complex lenses do indeed provide sufficient flux for accurate spectroscopy (see Alcock 1999a) and so the opportunity for using this technique to probe circumstellar envelopes clearly exists.

6.1 Expanding and rotating shells in circumstellar envelopes

In this study we examine the highly simplified cases of bulk motion in uniform expansion or rotation as previously considered in Ignace and Hendry (1999). The unlensed line profiles considered here make use of three important simplifications.

1. The star is approximated as a point source of illumination. This allows the effects of both absorption and occultation to be ignored.

2. The motion is simplified so that only optically thin spherical shells are considered. The result of this assumption is that every photon scattered or produced in the envelope will escape, meaning that the radiative transfer for the line profile reduces to a volume integral over the envelope.

3. It is assumed that the flow speeds in the envelope greatly exceed the thermal broadening. Thus the locus of points contributing to the emission at any particular frequency is an "isovelocity zone" – ie the locus of points with the same line of sight bulk motion. These zones are described by the Doppler shift formula

$$\nu_Z = \nu_0(1 - \frac{v_Z}{c}) \tag{6.1}$$

where (X, Y, Z) are the observer's coordinates with the line of sight along Z, ν_Z is the Doppler shifted frequency and $v_Z = -\mathbf{v}(\mathbf{r}) \cdot \hat{\mathbf{Z}}$ is the projection of the flow speed onto the line of sight. Differing line of sight flow speeds naturally result in differing frequencies of line emission and so the isovelocity zones can be identified.

It is by consideration of the geometry of the isovelocity zones produced by differing bulk motions that microlensing is shown to be a powerful probe of motion in circumstellar envelopes.

6.1.1 Constant expansion

Figure 6.1 represents the geometry of the isovelocity zones associated with uniformly expanding shells. In this case $\mathbf{v} = v_0\hat{\mathbf{r}}$. The velocity shift along the observers line of sight

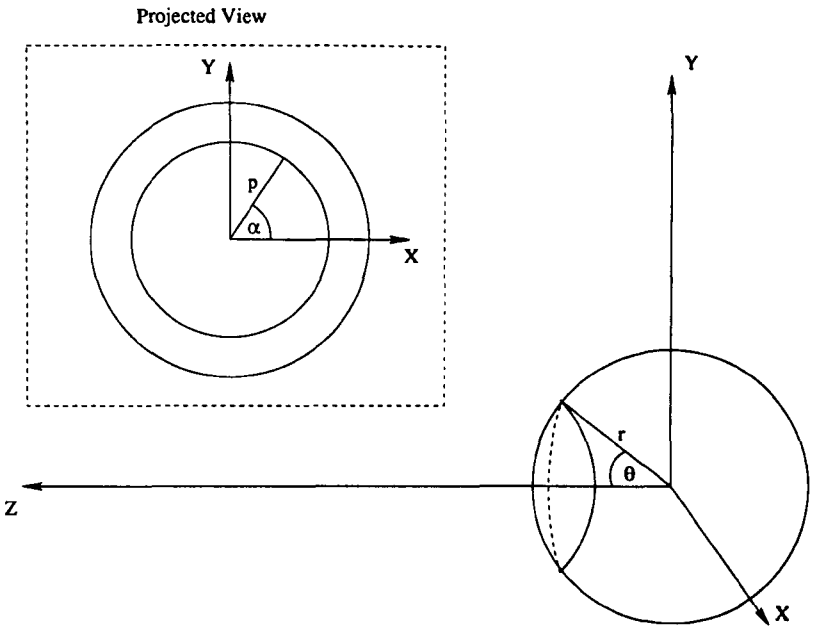

Figure 6.1: The geometry of a uniformly expanding spherical shell. Lower right shows the 3-dimensional view of the isovelocity zones, which are seen as rings centred on the Z-axis, ie the observer's line of sight. These zones are seen in projection in the upper right box.

is $v_Z = -v_0 \cos\theta = -v_{max} \cos\theta$, where θ is the angle between the line of sight and $\hat{\mathbf{r}}$. From Equation 6.1 it is clear that the isovelocity zones (i.e. when v_Z is constant) occur at constant values of θ and so trace a ring on the surface of the shell.

Consider now a ring of radius p. So the intensity at radius p and position angle α, measured from X in the $X - Y$ plane, is $I_\nu(p, \alpha)$. The observed flux of line emission from this ring is

$$F_\nu = \int_0^{2\pi} I_\nu(p, \alpha) p \, \mathrm{d}p \, \mathrm{d}\alpha = 2\pi I_\nu(p) p \, \mathrm{d}p \tag{6.2}$$

as $I_\nu(p, \alpha) \equiv I_\nu(p)$. Furthermore $I_\nu(p)$, the observed intensity from the isovelocity ring with radius p, is $j_\nu(r) \, \mathrm{d}z$ where j_ν is the emissivity.

Using spherical coordinates with

$$\mathrm{d}V = r^2 \, \mathrm{d}r \, \mathrm{d}\mu \, \mathrm{d}\alpha \tag{6.3}$$

and

$$\mathrm{d}\mu = -\frac{\mathrm{d}v_z}{v_0} = -\sin\theta \, \mathrm{d}\theta \tag{6.4}$$

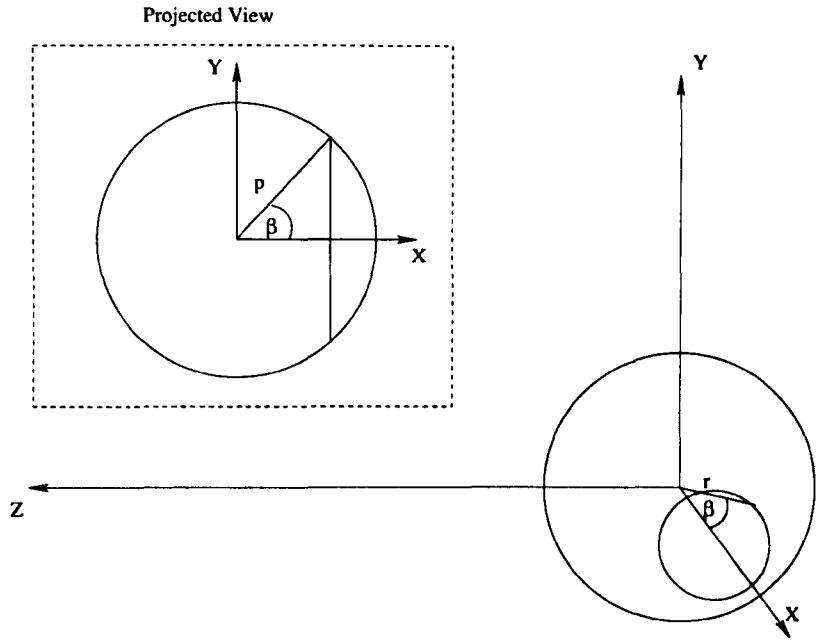

Figure 6.2: The geometry of a uniformly rotating spherical shell. Lower right shows the 3-dimensional view of the isovelocity zones, which are seen as rings centred on the X-axis. The zones are seen in projection in the upper right box as strips.

The flux in Equation 6.2 becomes

$$F_\nu = \int_{v_Z} j_\nu(r)\,\mathrm{d}z p\mathrm{d}p\mathrm{d}\alpha = \int_{v_Z} j_\nu(r)\,\mathrm{d}V. \tag{6.5}$$

The total flux from the line emissions, from the ring, is now

$$F_\nu = \frac{2\pi r^2 j_\nu(r)}{v_0}\,\mathrm{d}r\,\mathrm{d}v_Z \tag{6.6}$$

As the velocity shift term, v_Z, is not present in this expression, the total flux from line emissions, F_ν is constant with frequency. This results in a flat top line profile and the observer is unable to differentiate between the isovelocity zones. The flux from every isovelocity zone is the same and so the size of the flat top feature is limited by the velocity of expansion v_0 at the extremities of the source on the x axis.

6.1.2 Constant rotation

In the case of uniform rotation the flow velocity is given by $\mathbf{v} = v_0\hat{\varphi}$ and the velocity shift becomes $v_Z = -\sin\theta\cos\varphi\sin i$, where i is the viewing inclination. Again the isovelocity

zones reduce to circular rings, however in this case they are concentric around the X axis. The flux of line emission from the ring F_ν becomes

$$F_\nu = \frac{2\pi r^2 j_\nu(r)}{v_0 \sin i} \, \mathrm{d}r \, \mathrm{d}v_Z \tag{6.7}$$

for a rotating shell. As with constant expansion a flat top line profile is produced, but there are clear geometric differences in the projection of the isovelocity zones between the two cases. In the expanding case the isovelocity ring is circular in projection, however in the rotating case the ring is viewed "edge on" and so appears as a strip. In the expanding case the shells are front back symmetric – every isovelocity zone on the front side is identical to one on the back with opposite v_Z sign – in the rotating case the symmetry is left–right. It is these differences in the projection of the isovelocity zones that have significant repercussions when the effects of microlensing are considered, despite these geometric differences not being evident from the unlensed line profiles.

6.2 Microlensing by a point mass lens

As discussed previously, in extended source microlensing the amplification is given by the intensity weighted amplification averaged over the surface of the source star, ie

$$A(t) = \frac{\int_0^{2\pi} \int_0^{r_{\mathrm{source}}} I(r,\theta) A(r,\theta,t) r \, \mathrm{d}r \, \mathrm{d}\theta}{\int_0^{2\pi} \int_0^{r_{\mathrm{source}}} I(r,\theta) r \, \mathrm{d}r \, \mathrm{d}\theta} \tag{6.8}$$

where (r,θ) are the radial coordinates in the source plane. And $A(r,\theta,t) = A(u)$, using the familar point source form of the amplification function

$$A(u) = \frac{u(t)^2 + 2}{u(t)\sqrt{u(t)^2 + 4}} \tag{6.9}$$

So in order to calculate the amplified flux from the line profiles it is necessary to calculate the projected distance, u, between the isovelocity zone and the lens. The results of such calculations for this case are given in Ignace and Hendry (1999). However a brief discussion, intended to acquaint the reader, follows in the next Section.

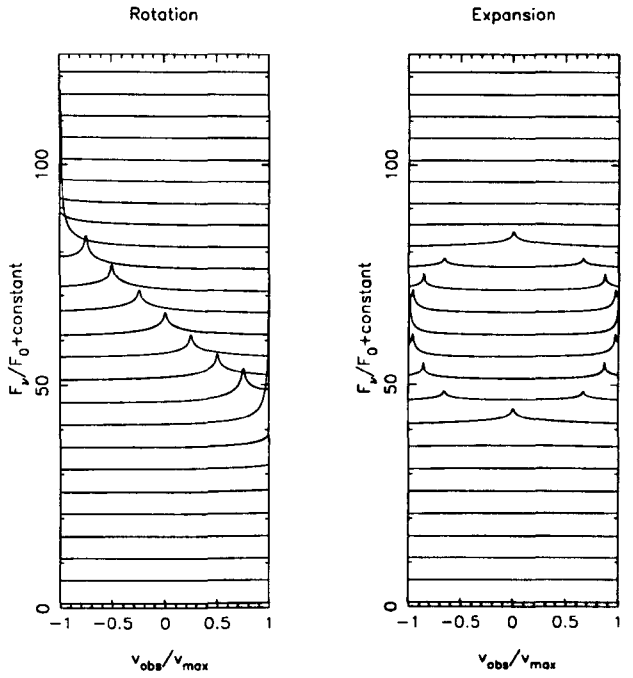

Figure 6.3: The line profile evolution (time increasing upwards) of an uniformly rotating shell, left panel and an uniformly expanding shell, right panel. In this example the shell radius is $0.5AER$, the minimum impact parameter is 0.0 and the lens trajectory is inclined at an angle of 45° to the projected axis of rotation. The constant offset is applied between the line profiles in order to clearly show the evolution throughout the event.

6.2.1 Distinguishing expansion from rotation

Figure 6.3 compares the line profile evolution between rotating and expanding shells. The observed velocity shift is $v_{obs} = v_Z$ and the maximum velocity shift is equal to v_0 in the case of expansion and $v_0 \sin i$ in the case of rotation. In this example the shell radius, ρ is equal to $0.5\theta_E$. The lens transits the shell with impact parameter u_E equal to 0.0 – the shell centre. Furthermore these events were calculated for a parameters in which the lens trajectory position angle, measured from the Y-axis (the axis of rotation), is 45°. The panels present a sequence of line profiles, beginning at the bottom with the centre of the shell at a projected distance of $3\theta_E$ from the lens, to minimum impact parameter – the middle line profile – to a projected distance of $3\theta_E$ on the other side of the lens. The line profiles are plotted as the ratio of the lensed flux to the unlensed flux with a constant offset to allow the reader to easily discriminate the line profiles at different stages during the event.

Also in this Figure (and in all of the following line profile evolution figures) the amplification in the expanding case is multiplied by 2 to make the peaks clearer.

It is clear that, due to the effects of microlensing, both cases differ from the unlensed *top hat* profile that they share. It is very evident from these examples that the microlensed line profiles are discernably different from each other. In the case of expansion, the line profiles are symmetric about line centre, yet in the rotating example the peak amplification appears to move through the line profile as the event progresses. These differences can be explained by considering the geometry of the isovelocity zones in each of the two cases. For example, in the expanding case the isovelocity zones appear as strips and as the amplification at each timestep is dominated by the portion of the circumstellar envelope close to the lens, it can be thought that the lens amplifies each strip in turn. However in the instance of expanding shells, where the isovelocity zones are front-back symmetric, at any instant during the transit the amplication will be dominated by two sources of flux, one from the 'front' of the envelope and one with equal but opposite sign velocity shift from the 'back' of the envelope, again at the closest projected distance between the shell and the lens.

It was seen, by Ignace and Hendry that in the smaller shell radii cases the amplification can be said to be *peakier*. The less compact the shell is the lower the peak amplification becomes. Although larger shells do increase the likelihood of a transit event, they would require very accurate spectroscopic monitoring to in order to deduce the velocity field. This is unsurprising considering the effects observed in the previous chapters where it was shown that large sources effectively *dilute* the amplification.

For this technique to be used successfully it is vital that the events are transits, the lens *must* transit the source for useful information to be gained from the line profile evolution. This means that transit events must be triggered by the surveying program in order to allow follow–up spectroscopic data to be taken. The symmetry is only broken by the high gradient of magnification over the source: if this gradient is not present, ie the projected source–lens separation is greater than the source radius, then it is not possible to distinguish between the two velocity fields. However in practice it is actually quite difficult to trigger point lens extended source events.

6.3 Microlensing by a fold caustic

As discussed previously caustic crossing events due to the presence of, for example, a binary lens afford a considerably better opportunity for gravitational imaging as they can be triggered by the first caustic crossing, since every source is essentially an extended source and there are frequently very high amplifications allowing for spectroscopic studies.

6.3.1 The amplification function

As discussed previously, in the vicinity of a fold caustic the amplification function can be approximated by $A \propto 1/\sqrt{u}$ where u is the distance from the fold. This allows the excess amplification in the region close to the fold to be examined using the relation.

$$A(u) = A_0 + \frac{b_0}{\sqrt{u}} \tag{6.10}$$

where A_0 is the total magnification of the images unaffected by the caustic crossing and, thus, can be taken to be constant. Furthermore, b_0 can be taken to be 1 for a typical caustic in the region of the crossing. For $u < 0$, outside the caustic, $A(u) = A_0$. This approximation assumes that the caustic is a straight line (i.e. the curvature of the caustic is small in comparison with source size) and that the caustic crossing point is not in the vicinity of a cusp, where the amplification function would take a different form. In order to calculate the lensed flux it is nescessary to integrate over source, with the excess flux due to the crossing being calculated for each surface element inside the caustic structure.

6.3.2 Example line profiles

In the situation illustrated in Figure 6.4, the source trajectory is normal to the fold caustic, i.e. the caustic motion is along the X-axis, as we centre our coordinates on the source in these examples. Consider a point R such that

$$R = (x, y) = (s\cos\theta, s\sin\theta) \tag{6.11}$$

coordinates again centered on the source, the fold is perpendicular to the X axis and so the

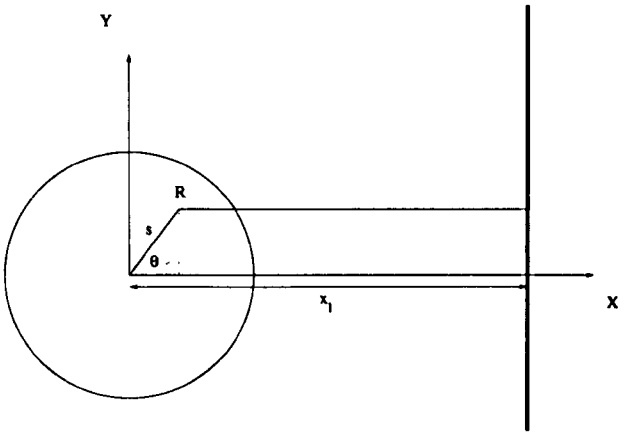

Figure 6.4: The geometry of a line caustic crossing

X coordinate of the caustic is constant at any particular timestep. The distance between the element at point R and the fold caustic is

$$u = x_l - s\cos\theta \tag{6.12}$$

And to ensure real magnifications only, the amplification only occurs if $s\cos\theta < x_l$; i.e. the element must be inside the caustic (to satisfy this inequality). We consider the case in which x_l increases from a negative value before crossing the source to a positive value when the source is inside the caustic. This is equivalent to the first caustic crossing, during which additional images are produced.

Figure 6.6 compares the evolution of microlensed line profiles from expanding shells (right hand panel) and rotating shells (left hand panel). In these figures the observed velocity shift $\mathrm{v_{obs}}$ is equal to v_Z and the maximum velocity shift $\mathrm{v_{max}}$ is equal to v_0 for expanding shells and $v_0 \sin i$ for rotating shells. In this example the shell radius is $0.1\theta_E$. Furthermore in the case of the rotating shells it is assumed that the axis of rotation is orthogonal to the source trajectory.

Figure 6.6 shows a sequence of line profiles beginning with the centre of the shell at a projected distance of 3ρ outside the caustic, crossing the caustic and then ending at a projected distance of 3ρ inside the caustic. The line profiles are plotted as the ratio of the lensed flux to the unlensed flux in each case – a constant offset is used to clearly

demonstrate the effect of the lensing – in the same manner as the examples in the previous section. The line profile evolution is shown from the source being outside the caustic at the bottom of the figure to the centre of the source crossing the caustic in the central line profile to all the source being inside the caustic at the top.

Again it is clear from this example that the microlensed line profiles resulting from constant expansion or constant rotation are different from each other, as the high gradient of magnification has broken the symmetry between the two models of bulk flow. In the case of expansion, the line profiles are symmetric about line centre, yet in the rotating example the peak amplification appears to move through line profile as the event occurs. And again these differences can be explained by considering the geometry of the isovelocity zones in each of the two cases. For example, in the expanding case the isovelocity zones appear as strips and as the amplification at each timestep is dominated by the portion of the circumstellar envelope transiting the caustic, it can be thought that the caustic amplifies each strip in turn. However in the instance of expanding shells, where the isovelocity zones are front-back symmetric, at any instant during the transit the amplication will be dominated by two sources of flux, one from the 'front' of the envelope and one with equal but oppsite sign velocity shift from the 'back' of the envelope.

In these examples the peak magnifications also vary between the models, for that rotating case the peak magnification is 36.5 and for expansion is 8.9. This large difference in peak magnification can be attributed to the isovelocity zones in the rotating case being parallel to the fold and so at any instant during the crossing, it can be considered that all of one individual isovelocity zone is crossing the caustic. Whereas in the expanding case different parts of the same isovelocity zone contribute their peak magnification at different times.

Of course not all the source trajectories will be normal to the caustic and the geometry of such a situation is shown in Figure 6.5, with

$$R = (x, y) = (s\cos\theta, s\sin\theta) \tag{6.13}$$

And

$$P = (x_l, 0) \tag{6.14}$$

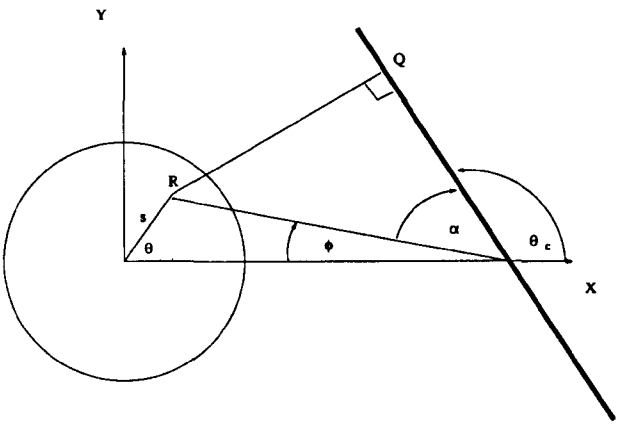

Figure 6.5: The geometry of a generalised line caustic crossing

so the distance $|PR|$ is found

$$|PR| = \sqrt{y^2 + (x - x_l)^2}. \tag{6.15}$$

The angle α is therefore

$$\alpha = \pi - \theta_c - \tan^{-1}(\frac{y}{x - x_l}), \tag{6.16}$$

giving the perpendicular distance to fold caustic from point R to be

$$d_l = \sqrt{y^2 + (x - x_l)^2}\sin(\theta_c + \tan^{-1}(\frac{y}{x - x_l})), \tag{6.17}$$

and so allowing one to integrate over source using Equation 6.8 and amplification approximation in Equation 6.10 with the distance as defined in Equation 6.17 . This has been again computed for both expanding and rotating shells and the results are shown in Figures 6.7, 6.8, 6.9 and 6.10 in this section. In these examples the amplification appears to be spread out over a wider range of frequencies at each timestep. In these cases it can be thought that the minimum impact parameter (the smallest projected caustic/shell distance) occurs for many isovelocity zones at any instant. By varying the value θ_c the fold caustic can cross many isovelocity zones at any point and thus the amplification is dominated by the flux from more than one isovelocity zone. Of course this also means that a particular isovelocity zone makes a contribution at several stages during the event which in turn results in notches being seen in the line profiles as some parts of the isovelocity zone are not being lensed close the peak amplification. As the amplification is generally smaller in these cases, it can be observed that caustic crossings normal to the caustic are the most effective means of probing the circumstellar envelope. One might argue, conversely, that

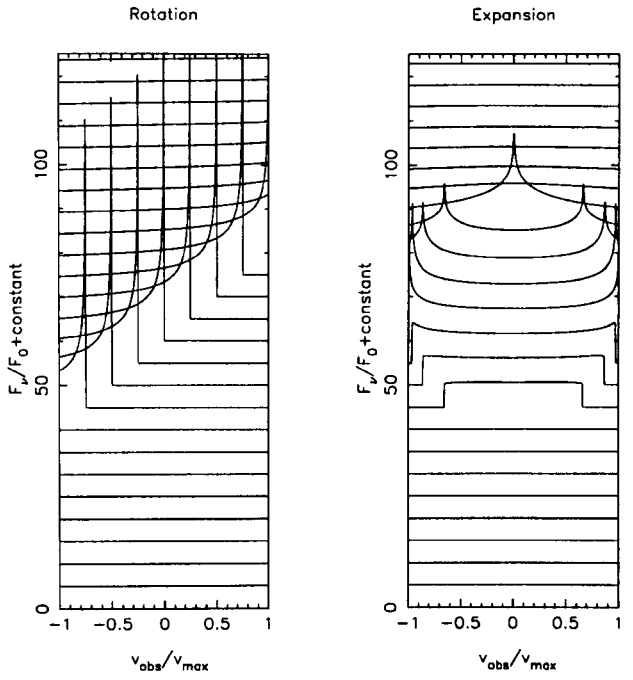

Figure 6.6: The line profile evolution (time increasing upwards) of an uniformly rotating shell, left panel and an uniformly expanding shell, right panel. In this example the shell radius is $0.1\theta_E$ and the source trajectory is perpendicular to the fold caustic with the source exiting the caustic structure. The constant offset is applied between the line profiles in order to clearly show the evolution throughout the event.

the more acute trajectories result in longer timescales, thus resulting in longer integration periods for spectrocopic studies.

6.4 Microlensing by parabolic fold caustic

We are now at a situation where it has been shown that microlensing by both point and fold caustics can powerfully diagnose motion in circumstellar envelopes. It is now possible to improve the inverse square root amplification approximation to account for parabolic caustics rather than straight lines.

6.4.1 Approximation

In the previous section we applied the well known amplification approximation to microlensing circumstellar envelopes. It has been shown however (e.g. Schneider 1992 and

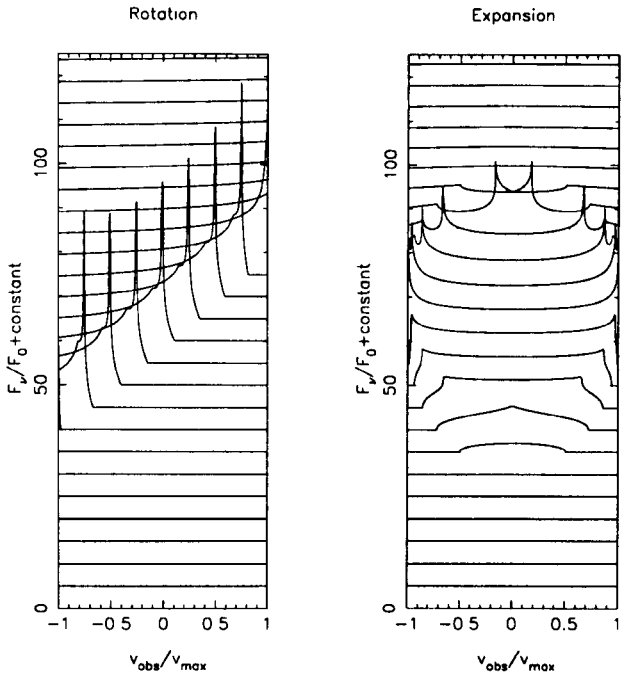

Figure 6.7: The line profile evolution (time increasing upwards) of an uniformly rotating shell, left panel and an uniformly expanding shell, right panel. In this example the shell radius is $0.1\theta_E$ and for a θ_c of 100°.

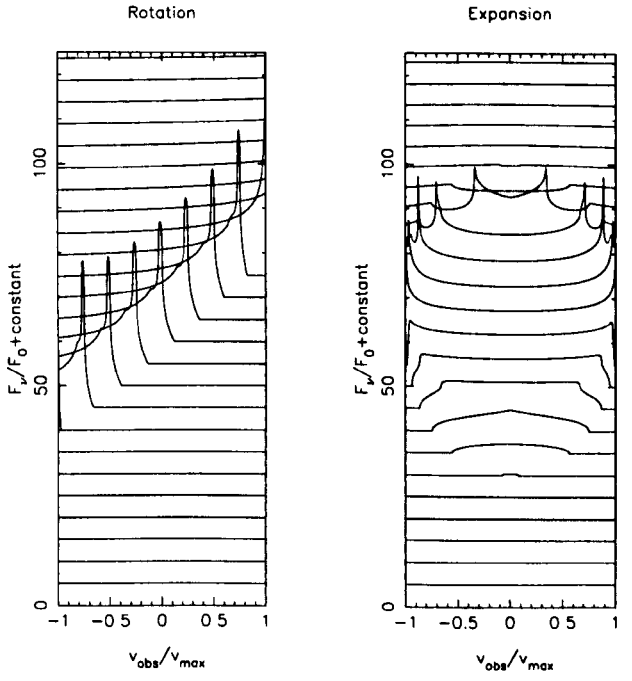

Figure 6.8: The line profile evolution (time increasing upwards) of an uniformly rotating shell, left panel and an uniformly expanding shell, right panel. In this example the shell radius is $0.1\theta_E$ and for a θ_c of 110°.

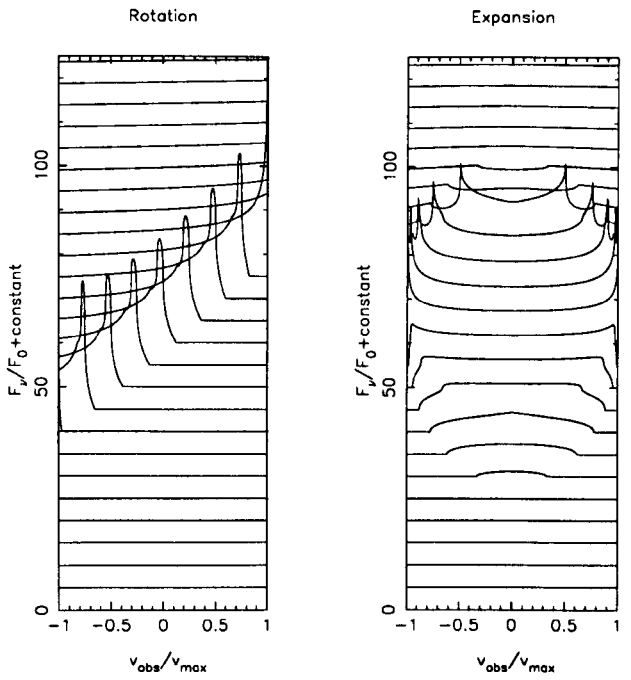

Figure 6.9: The line profile evolution (time increasing upwards) of an uniformly rotating shell, left panel and an uniformly expanding shell, right panel. In this example the shell radius is $0.1\theta_E$ and for a θ_c of 120°.

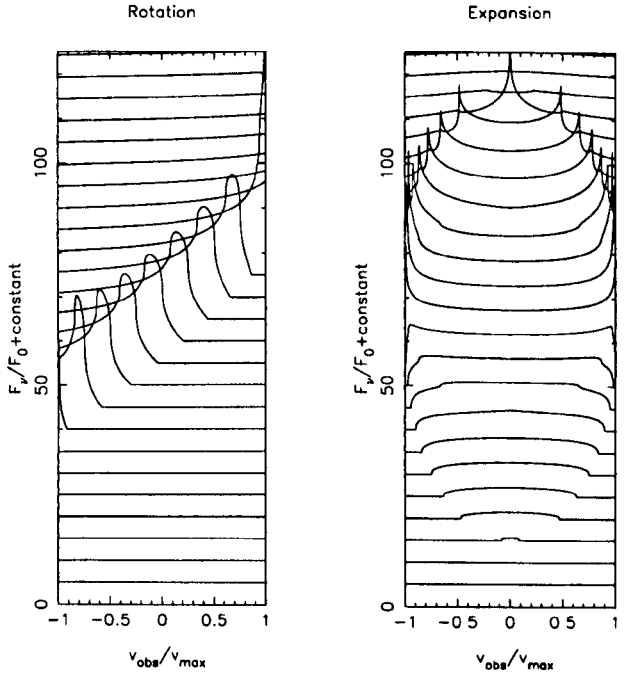

Figure 6.10: The line profile evolution (time increasing upwards) of an uniformly rotating shell, left panel and an uniformly expanding shell, right panel. In this example the shell radius is $0.1\theta_E$, and for a θ_c of 150°.

Chang and Refsdal 1984) that the local shape of a caustic is actually parabolic. Fluke and Webster (1999) demonstrated that a parabolic approximation to the amplification could be applied to extended source microlensing with particular interest to investigating quasar geometry. As with the inverse square root approximation, this is only valid within a few source radii of the caustic and not in the vicinity of a cusp.

The parabola used is of the form

$$x = \zeta y^2 \tag{6.18}$$

Where ζ specifies the shape of the caustic and so the amplification function, as a function of u the distance normal to the caustic becomes

$$A(u) = A_0 + \frac{b_0}{\sqrt{u - \zeta y^2}} \tag{6.19}$$

for sources inside the caustic. And in the manner of the previous section to ensure real amplification, for sources outside the caustic structure $A(u) = A_0$.

For an extended source the amplification is found in the usual manner throughout this thesis, i.e. by integrating the amplification function over the source and normalising by integration over the intensity.

6.4.2 Application to circumstellar envelopes

Considering parabolic caustics is of particular interest in studying circumstellar envelopes because of their considerable size. Binary lenses imaging stars in the Galactic Bulge will have caustic structures of the order of a few AU and so it seems unlikely to assume that all caustic crossings will occur over regions where the source size is considerably smaller than the caustic structure. Analysis of the the event EROS-BLG-2000-5 by the EROS collaboration included the effects of caustic curvature (Afonso et al., 2000b) by varying the trajectory of the caustic over the source, i.e. by changing the angle $theta_c$, rather than incorporating a specific form for the curvature as is used here.

6.4.3 Examples

Figure 6.11 represents the situation in which an extended source is entering a parabolic caustic, where the caustic is of the form $x = \zeta y^2$ and the caustic is progressing along the X-axis during the event (we are employing coordinates centred on the source rather than the caustic). Again we can consider a point R such that

$$R = (x, y) = (s\cos\theta, s\sin\theta) \tag{6.20}$$

The source element crosses the caustic when

$$u = x_l - x - \zeta y^2 = 0 \tag{6.21}$$

where x_l is the distance from the centre of the source to the centre of the caustic. As stated previously the magnification only occurs for elements inside the caustic and thus is only calculated for elements for which $u > 0$.

Figures 6.12, 6.13 and 6.14 present the line profile evolution is the usual manner for the type of event illustrated by Figure 6.11 in which a source being lensed by a parabolic caustic of shape factor, $\zeta = 0.2, 0.9$ and 2.0 respectively.

The Figures show the line profile evolution progressing from 3ρ at the bottom of the figure, entering the caustic, to a position at 3ρ from the centre of the caustic in the uppermost line profile as with the previous examples.

The effect of the curvature is not evident in these Figures 6.12, 6.13 and 6.14. The high gradient of magnification allows one to distinguish between the velocity field models, however one cannot establish any level of caustic curvature from the line profiles. If one is to apply a parabolic caustic with a large shape factor, i.e. $\zeta > 20$, then the number of isovelocity zones crossed at any given timestep increases dramatically.

In fact such a high shape factor for a source of radius $0.1\theta_E$ corresponds to a situation in which, at the moment the leading limb is crossing the caustic, the portions of the caustic

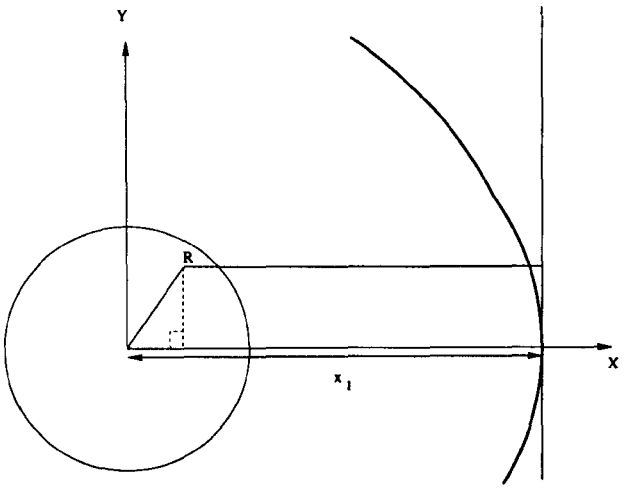

Figure 6.11: The geometry of a parabolic caustic crossing.

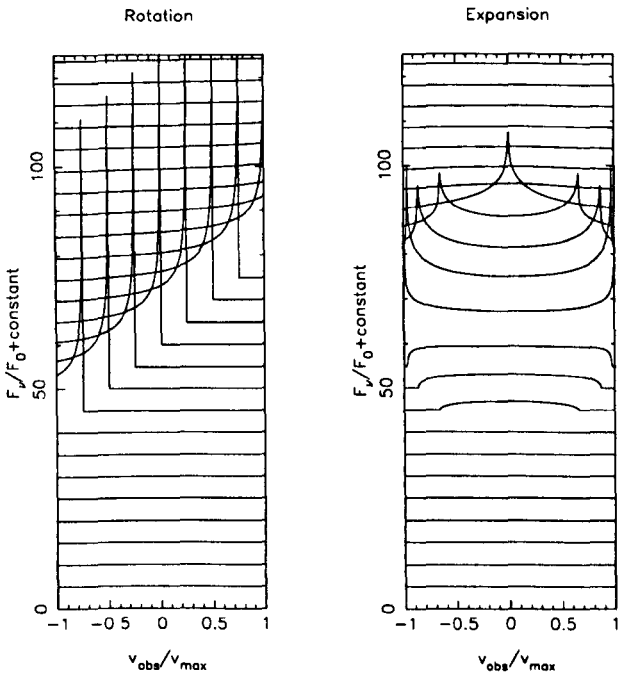

Figure 6.12: The line profile evolution (time increasing upwards) of an uniformly rotating shell, left panel and an uniformly expanding shell, right panel. In this example the shell radius is $0.1\theta_E$ and the source trajectory is perpendicular to the fold caustic. The shape factor ζ of the parabolic caustic is 0.2.

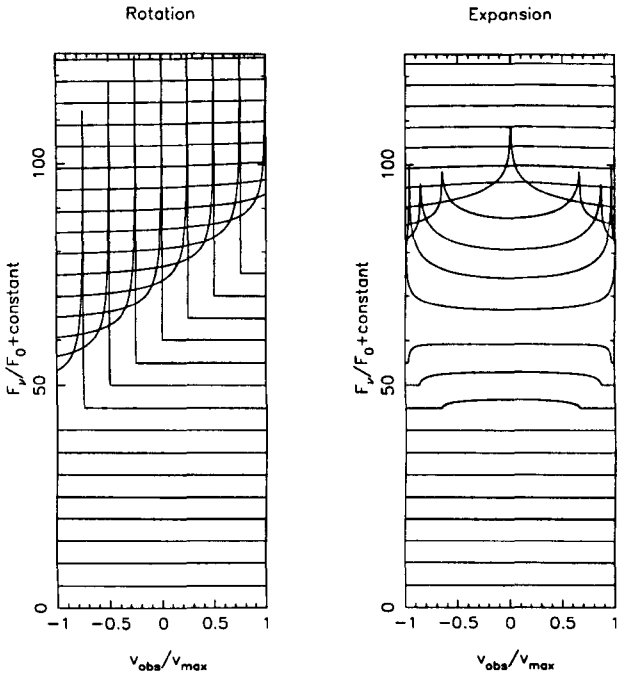

Figure 6.13: The line profile evolution (time increasing upwards) of an uniformly rotating shell, left panel and an uniformly expanding shell, right panel. In this example the shell radius is $0.1\theta_E$ and the source trajectory is perpendicular to the fold caustic. The shape factor ζ of the parabolic caustic is 0.9.

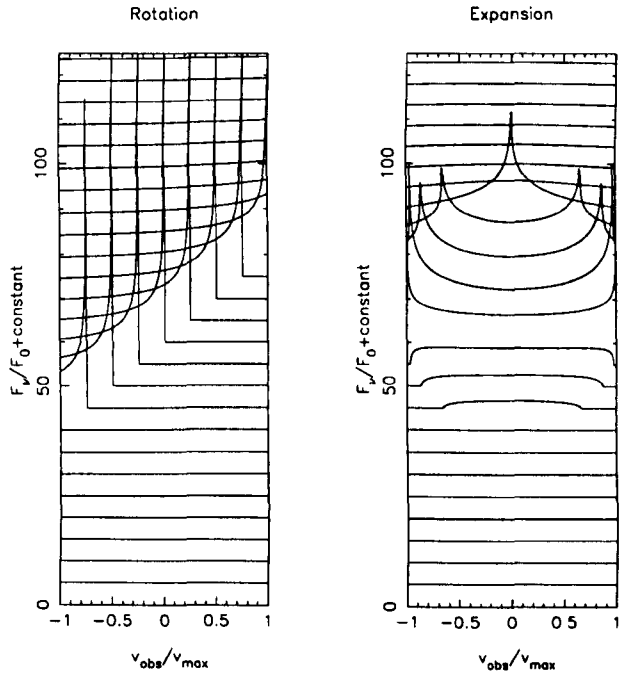

Figure 6.14: The line profile evolution (time increasing upwards) of an uniformly rotating shell, left panel and an uniformly expanding shell, right panel. In this example the shell radius is $0.1\theta_E$ and the source trajectory is perpendicular to the fold caustic. The shape factor ζ of the parabolic caustic is 2.0.

that crossed the source first (at both the uppermost and lowermost parts of the limb) are already a source radius away from the limb. In this situation the fold is crossing a large number of isovelocity zones; which would reduce the peak amplification as well as distorting the line profile evolution to such an extent that one could no longer diagnose an appropriate wind model. However such highly curved caustics are typically close to cusps and the structure as a whole is smaller and so they are by no means ideal for gravitational imaging as they would be difficult to trigger for.

As the effect of considering parabolic caustics in these more realistic examples is not discernable, it is possible to conclude that spectroscopic studies would not be significantly hampered by parabolic caustics with small shape factor. This also means that the gravitational imaging technique would be difficult to use as an additional means of differentiating between degenerte lens models.

6.4.4 Generalised examples

Finally, we consider crossings that are not normal to the caustic; such a situation is illustrated in Figure 6.15. In these examples the amplification was calculated in the usual way, as a function of distance to the caustic.

The element to caustic seperation calculated takes account of the source trajectory in a similar manner to the straight line fold caustics, but with the modification of a parabolic caustic. The sources are again entering the caustic, with the caustic therefore being concave.

Examples of such crossings are shown in Figures 6.16, 6.17, 6.19, 6.20, 6.21 and 6.18 for shape factors $\zeta = 0.2, 0.9$ and 2.0 as before, but for varying source trajectories of either 110° or 130°.

The resulting line profile evolutions on the following pages are much more complex than any of the previous situations. These distorted evolutions are the result of a large number of isovelocity zones being crossed at any instant, and also the fact that varying these parameters means that the zones are effectively crossed and thus amplified at different

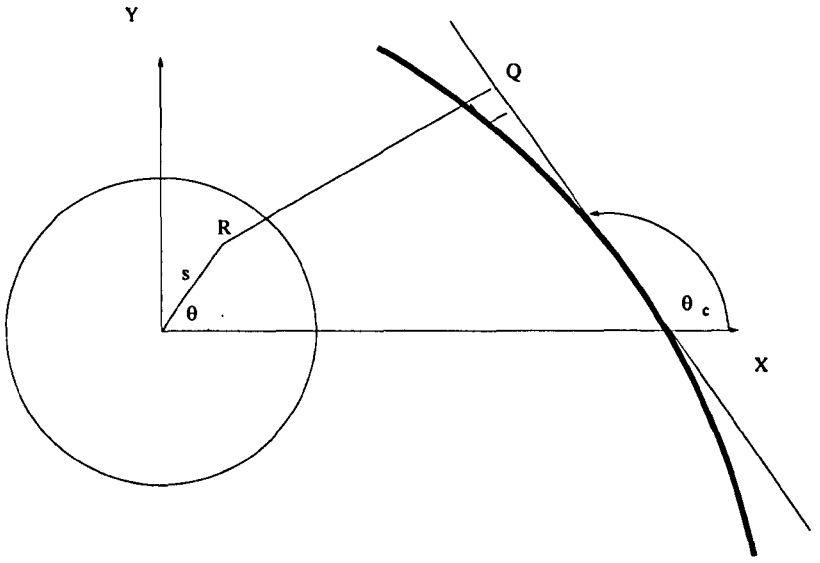

Figure 6.15: The geometry of a generalised parabolic caustic crossing

stages during the event.

However it is still possible to clearly distinguish between the velocity field models and so the 'imaging' of the circumstellar envelope by a slightly parabolic caustic is clearly possible.

6.5 Observational considerations

In order for motion within circumstellar envelopes to be observed during microlensing events, several factors need to be carefully considered. For point mass lens events there is a need for low impact parameter events, which are unfortunately difficult to alert. One could hope that observations of the source pre-transit would indicate the presence of an extended circumstellar envelope, thus making it clear that a spectroscopic study of the event would be appropriate. It is, however, important to stress that there is a need for transit events for the symmetry of the source to be broken before the nature of the bulk motion can be discovered.

It is abundantly clear that the prospects for diagnosing bulk motion are considerably better for the case of caustic crossings. The increased flux and, equally importantly, the first crossing trigger, mean that spectroscopic studies of ongoing events are becoming

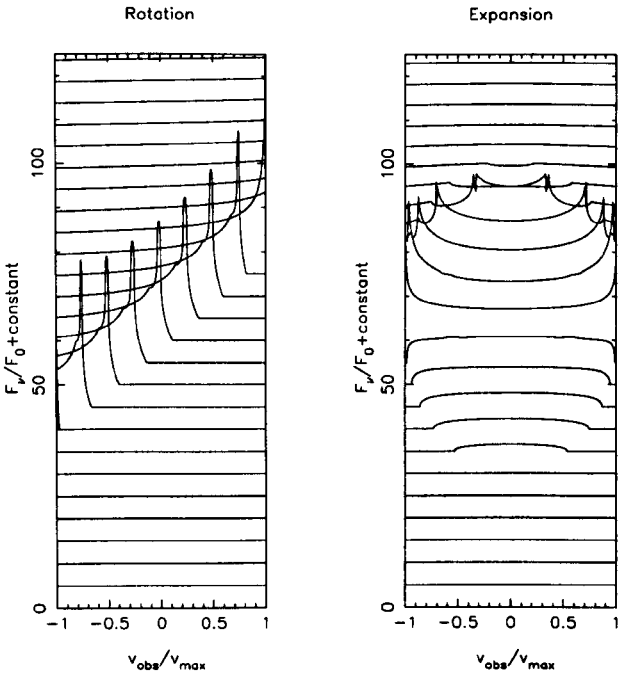

Figure 6.16: The line profile evolution (time increasing upwards) of an uniformly rotating shell, left panel and an uniformly expanding shell, right panel. In this example the shell radius is $0.1\theta_E$ and for a θ_c of 110°. The shape factor ζ of the parabolic caustic is 0.2

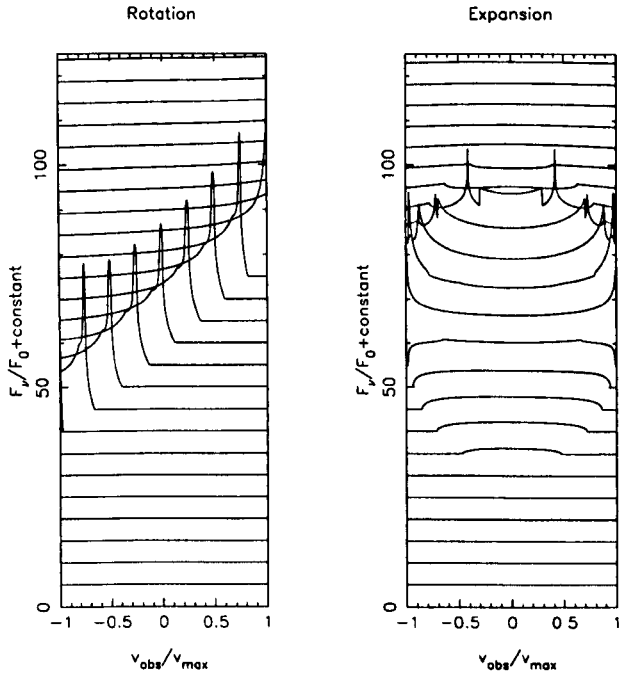

Figure 6.17: The line profile evolution (time increasing upwards) of an uniformly rotating shell, left panel and an uniformly expanding shell, right panel. In this example the shell radius is $0.1\theta_E$ and for a θ_c of 110°. The shape factor ζ of the parabolic caustic is 0.9.

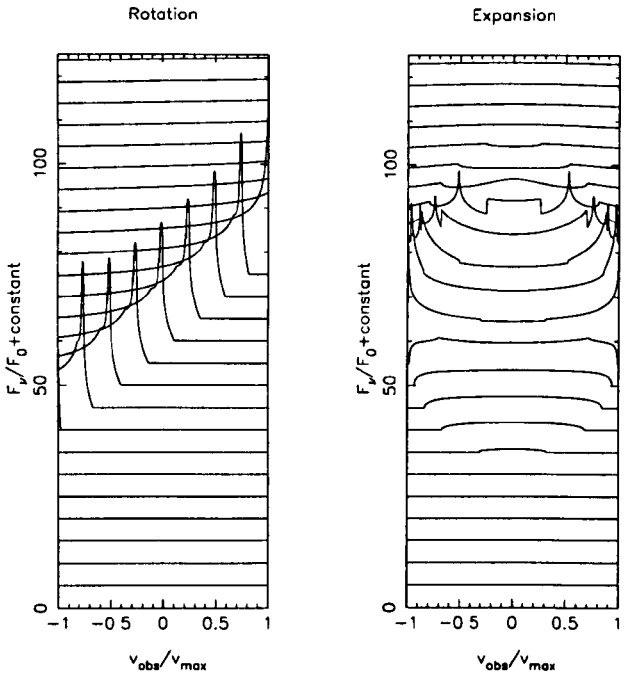

Figure 6.18: The line profile evolution (time increasing upwards) of an uniformly rotating shell, left panel and an uniformly expanding shell, right panel. In this example the shell radius is $0.1\theta_E$ and for a θ_c of 110°. The shape factor ζ of the parabolic caustic is 2.0.

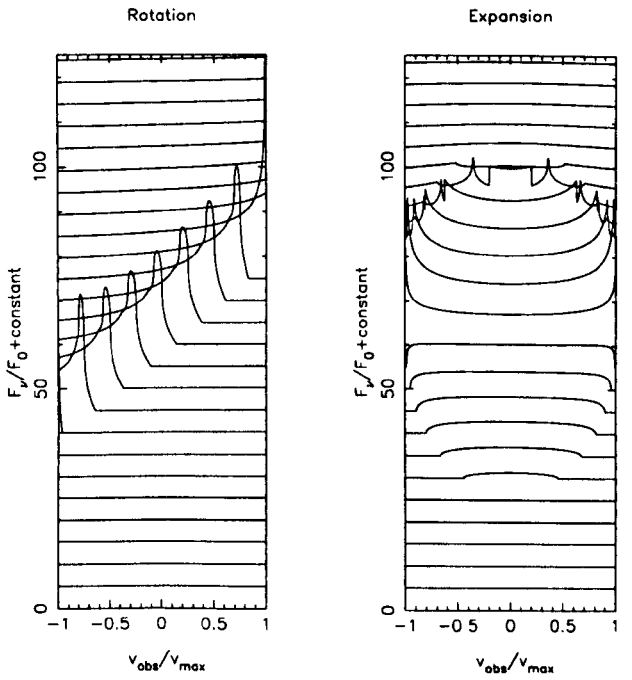

Figure 6.19: The line profile evolution (time increasing upwards) of an uniformly rotating shell, left panel and an uniformly expanding shell, right panel. In this example the shell radius is $0.1\theta_E$ and for a θ_c of 130°. The shape factor ζ of the parabolic caustic is 0.2

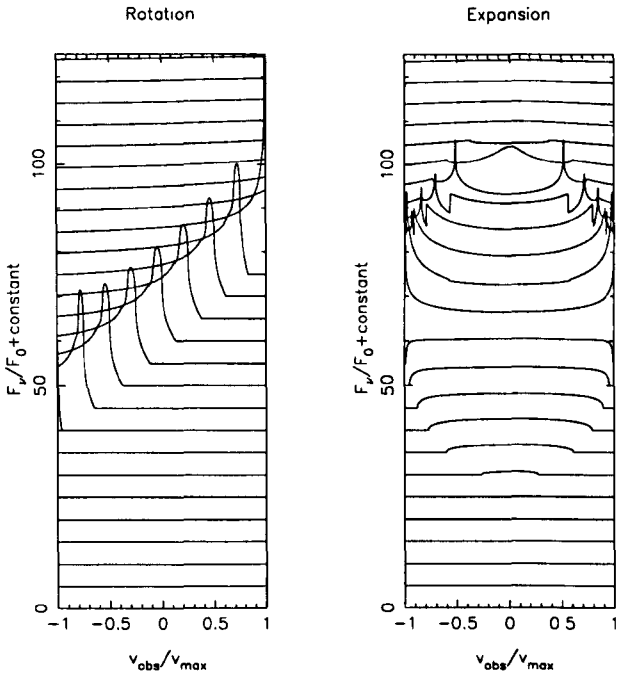

Figure 6.20: The line profile evolution (time increasing upwards) of an uniformly rotating shell, left panel and an uniformly expanding shell, right panel. In this example the shell radius is $0.1\theta_E$ and for a θ_c of 130°. The shape factor ζ of the parabolic caustic is 0.9.

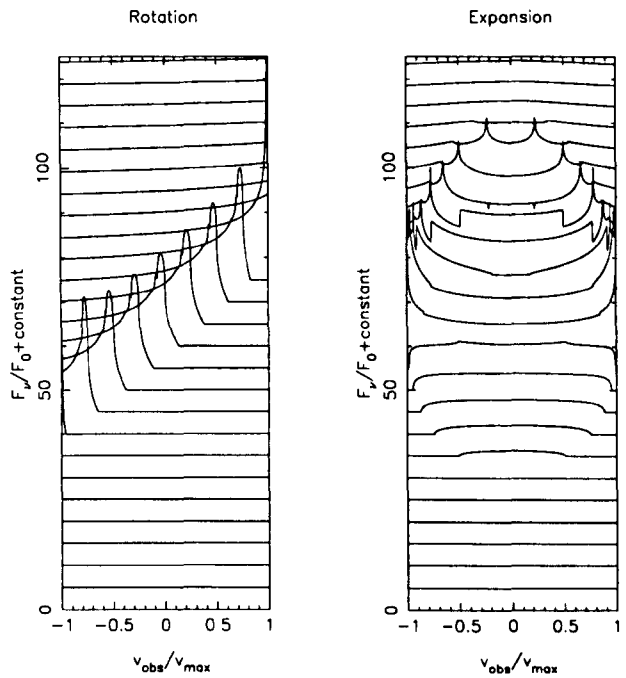

Figure 6.21: The line profile evolution (time increasing upwards) of an uniformly rotating shell, left panel and an uniformly expanding shell, right panel. In this example the shell radius is $0.1\theta_E$ and for a θ_c of 130°. The shape factor ζ of the parabolic caustic is 2.0.

increasingly common. Such studies may choose to examine , for example, the $H\alpha$ line during the source transit, this would not necessarily be the correct choice for observations of the circumstellar envelope, one would have to carefully choose a suitable wavelength of observation, i.e. a wavelength sensitive to circumstellar emissions and more obviously present within the source. Caustic crossing events do, nevertheless, retain the ability to distinguish between the models.

Chapter 7

Conclusions and Future Work

This thesis examined several aspects of extended source microlensing as a probed of the source itself. We have investigated the microlensing signatures of various stellar atmosphere models, as would be seen in multicolour observations of point lens and fold caustic events. We have also considered the photometric signatures of starspots and variable sources, and the spectroscopic signatures of circumstellar envelopes. In all cases we have strived to demonstrate that microlensing is a excellent diagnostic tool for studying these astrophysical situations, and moreover the sampling strategies and observational precison required to yield effective results from microlensing are already within the grasp of current technology.

All the events modelled within this work were located within in the Milky Way. The motivation for this approach was that such events could be observed by current microlensing surveys already intensively observing microlensing events. In some ways, one could say that determining, for example, the source surface brightness profile is a "spin-off" from the search for MACHOs and extra solar planets. Extended source microlensing events are rare, so it would not be feasible to monitor star fields intensively with the sole purpose of observing extended source events. It has been demonstrated, however, that this would also be completely unnecessary, as the rapid alert and then intensive follow-up campaigns currently used in the search for extra solar planets are also ideally suited to observing extended sources.

The vast majority of microlensing observations are photometric, with spectroscopic observations only being made during high amplification events; this strategy was reflected in this thesis, however, one may wish in future work to consider the diagnostic potential of different observational approaches.

One form of observational strategy that was not discussed here is that of using the high amplification to allow polarisation studies of the event to be made. Considerable theoretical work on the polarisation signatures of extended sources has already been carried out, Schnieder & Wagoner (1987); Simmons et al. (1995a, b); Agol (1996); Newsam et al. (1998); Coleman (1998). This work suggests that the high differential amplification across the source during low-impact parameter and caustic crossing events could allow the source limb polarisation to be measured, which could lead to an accurate determination of the actual source size relative to the lens.

There are several issues that could be addressed in future work, in order to develop microlensing as a tool for observing limb polarisation. Firstly, in the period since much of the existing theoretical work was carried out, the capabilities of the follow-up microlensing campaigns have greatly improved. A careful reassessment of the observational requirements and prospects for detecting limb polarisation from microlensing is now timely. On the theoretical side such studies should concentrate on the polarisation signatures during fold caustic crossing events, which are more *observationally friendly*; this case has received little attention so far. The other improvement that could be made to any such model would be the inclusion of a more sophisticated treatment of the scattering, rather than the Chandrasekhar pure electron scattering atmospheres considered already in Simmons et al. (1995a, b). It was shown in this thesis that microlensing could distinguish between competing stellar atmosphere models, such as the NextGen atmospheres which are particularly relevant to microlensing targets. It would be important to next establish the polarisation signatures from likely microlensing sources, by e.g. considering the effects of molecular scattering in cool giant stars. No observations of polarisation during a galactic microlensing event have been made as yet, but such a prospect is becoming less distant.

The model of starspots used in this work could be improved in several ways. For example

the assumption of circular spots is at some level unrealistic and could therefore be extended and improved. It was noted, however, that there are severe degeneracies in determining spot parameters from a microlensing lightcurve. This suggests that a more sophisticated treatment of the starspots may offer little additional insight, as the subtleties of a non-circular spot model may be lost by the smoothing action of the microlensing integral over the source. It is possible, however, that an inverse problem approach – such as the Backus Gilbert method – could be well suited to determining how much information can be acquired from a spotted lightcurve with a given photometric error and sampling rate. Analysis of multi-colour observations of such events may also be another way to extend the constraints on particular spot solutions, as the spot signature itself is strongly chromatic. This would require a careful examination of the optimal sampling strategy in order to observe the source in several colour bands.

The potential of spectroscopic observations is yet to be fully realised and there remain many areas in which further exploration is warranted. The spectroscopic model considered in this thesis allowed an examination of the line profile evolution due to bulk motion in circumstellar envelopes during caustic crossing events. The model applied to this situation was, however, fairly simplistic as only uniform rotation and expansion of a circumstellar shell were considered. The next stage of exploring the diagnostic capabilities of spectroscopy would be to examine the line profile evolution of a more realistic model of bulk motion. In particular, within a stellar context, it would be of interest to examine the spectroscopic signatures that would be produced in the expansion of supernova ejecta.

Appendix A

Starspot geometry and integration limits

We consider a star of radius, R, being lensed by both a point mass lens and a fold caustic.

A.1 Coordinate systems

We calculate the integrated flux from the star, in both the lensed and unlensed case, in terms of an integral over the projected stellar disk. There are three coordinate systems relevant to this calculation:

1. (α', ϕ') : spherical polar coordinates on the surface of the star, with the stellar equator defining $\phi' = 0$, and with α' measured counter-clockwise from the direction which is co-planar with the star's rotation axis and the line of sight (as shown in Figure A.1.).

2. (α, ϕ) : spherical polar coordinates on the surface of the star, but with polar axis $(\phi = \frac{\pi}{2})$ defined as the projection of the star's rotation axis on the plane of the sky and with azimuthal angle, α, measured counter-clockwise from the line of sight.

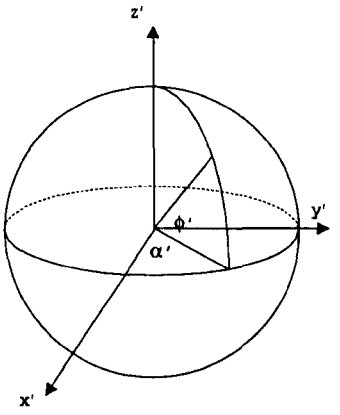

Figure A.1: Coordinate systems I

3. (s, θ) : projected circular polar coordinates on the stellar disk (i.e. the plane of the sky), with θ measured counter-clockwise from the y-axis (see below).

Figures A.1, A.1 and A.1 illustrate these coordinate systems and their associated Cartesian coordinate axes. Thus, we define the x-axis to be the line of sight, the z-axis to be the projection of the star's rotation axis onto the plane of the sky, and the y-axis to be the direction which completes a right-handed coordinate system. It is then easy to see that the y-axis and y'-axis are identical, and the x'-axis and z'-axis are obtained from the x-axis and z-axis by a rotation of $(\frac{\pi}{2} - i)$ about the y-axis, where i is the inclination of the star. In summary, for a star of radius, R, and a general point (x, y, z) on the stellar surface

$$\begin{aligned} x &= R\cos\alpha\cos\phi = R(\cos\alpha'\cos\phi'\sin i + \sin\phi'\cos i) \\ y &= R\sin\alpha\cos\phi = R\sin\alpha'\cos\phi' \\ z &= R\sin\phi = R(\sin\phi'\sin i - \cos\alpha'\cos\phi'\cos i) \end{aligned} \tag{A.1}$$

where all coordinates are expressed in units of the angular Einstein radius (AER) of the lens.

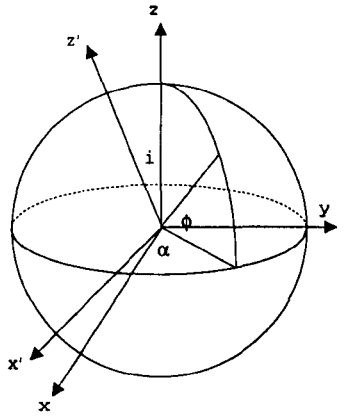

Figure A.2: Coordinate systems II

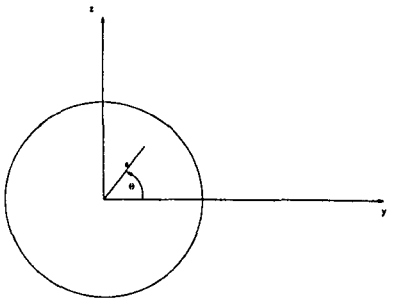

Figure A.3: Coordinate systems III

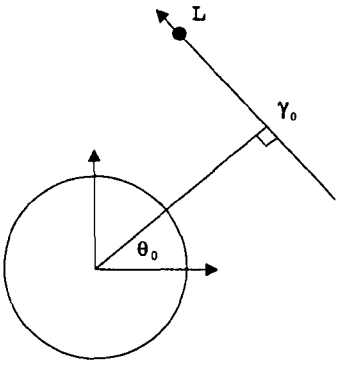

Figure A.4: Lens trajectory

A.2 Point mass lenses

Consider now the path of a point lens, as seen in projection on the sky. Figure A.4 shows the lens trajectory and the position of the lens at some general point, L, and at time, t. Here, γ denotes the impact parameter of the lens and γ_0 denotes the minimum impact parameter at the time of closest approach, t_0, when the lens has position angle θ_0, as shown. Let τ denote the time for the lens to move 1 AER. The coordinates (y_L, z_L), of the lens at position, L, are

$$\begin{aligned} y_L &= \gamma_0 \cos\theta_0 - \frac{(t-t_0)}{\tau} \sin\theta_0 \\ z_L &= \gamma_0 \sin\theta_0 + \frac{(t-t_0)}{\tau} \cos\theta_0 \end{aligned} \tag{A.2}$$

The projected separation, d, of the lens from an arbitrary point, $(y, z) = (s\cos\theta, s\sin\theta)$, on the stellar disk is

$$d = \left[(y_L - s\cos\theta)^2 + (z_L - s\sin\theta)^2\right]^{1/2} \tag{A.3}$$

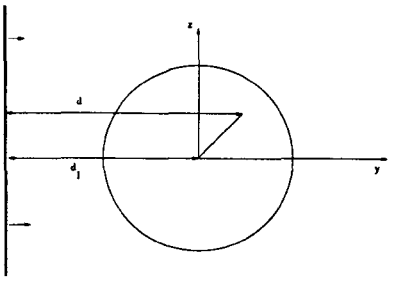

Figure A.5: Fold caustic trajectory

A.3 Fold caustics

Now consider the path of a fold caustic, again as seen inprojection on the sky. Figure A.5 shows the caustic trajectory and it's position at a general point, L, on the y–axis at time, t. We consider the situation for which the caustic is normal to the y–axis in the coordinate system show in Figure A.1. This means that the fold is perpendicular to the x–axis and so the x coordinate of any element of the caustic is constant throughout the duration of the caustic crossing.

The seperation from a point $(y, z) = (s\cos\theta, s\sin\theta)$, on the source to the caustic is

$$d = y_{\mathrm{L}} - s\cos\theta \tag{A.4}$$

To ensure real magnifications only when using the inverse square root approximation, the magnification only occurs if $s\cos\theta < y_{\mathrm{L}}$, meaning the element must be inside the caustic structure when considering the case with y_{L} increasing from a negative value to a positive value, ie the source entering the caustic structure during the first caustic crossing.

A.4 Defining the boundary of a circular starspot

We consider circular starspots – i.e. the locus of points defining the boundary of a spot is a small circle of angular radius δ, say. We suppose that each starspot maintains constant radius, temperature, $\log g$ and latitude (in the stellar-based coordinate system) throughout

the microlensing event, but that its longitude changes if the star is rotating.

Let (α_p', ϕ_p') denote the (stellar-based) coordinates of the centre of the starspot. If the star is not rotating, these coordinates remain fixed; if the star is rotating with period, P, and the spot centre transits at time, t_0, then

$$\alpha_p' = \frac{2\pi}{P}(t - t_0) \tag{A.5}$$

We can easily obtain from eqs. A.1 the projected circular polar coordinates, (s_p, θ_p), of P in the observer-based coordinate system. The circumference of the spot describes a planar circle of radius $R\sin\delta$. The centre, C, of this circle lies inside the star, i.e.

$$\begin{aligned} x_c &= R\cos\delta\cos\alpha_c\cos\phi_c \\ y_c &= R\cos\delta\sin\alpha_c\cos\phi_c = s_c\cos\theta_c \\ z_c &= R\cos\delta\sin\phi_c = s_c\sin\theta_c \end{aligned} \tag{A.6}$$

Note that $s_c = s_p\cos\delta$ and $\theta_c = \theta_p$.

Thus, when seen in projection the centre, C, of the planar circle defining the spot boundary is not coincident with the centre, P, of the spot on the surface of the star, but does lie along the same radial vector joining P to the centre of the stellar disk.

Consider a general point (x, y, z) on the circumference of the spot. We have

$$(x - x_c)^2 + (y - y_c)^2 + (z - z_c)^2 = R^2\sin^2\delta \tag{A.7}$$

and

$$x^2 + y^2 + z^2 = R^2 \tag{A.8}$$

Combining eqs. A.7 and A.8 gives, after some manipulation

$$xx_c + yy_c + zz_c = R^2\cos^2\delta \tag{A.9}$$

which, as expected, defines a plane perpendicular to the position vector (x_c, y_c, z_c).

A.5 Spot visibility conditions

Consider a unit vector in the direction of the spot centre, C. i.e.

$$\hat{n}_c = (\cos\alpha_c \cos\phi_c, \sin\alpha_c \cos\phi_c, \sin\phi_c) \tag{A.10}$$

Let η be the angle between the line of sight and $\hat{n}_c$. Then $\cos\eta = \cos\alpha_c \cos\phi_c$. A spot will be fully visible provided $\eta \leq \frac{\pi}{2} - \delta$, i.e.

$$\cos\alpha_c \cos\phi_c \geq \sin\delta \tag{A.11}$$

Similarly the spot will be fully invisible provided

$$\cos\alpha_c \cos\phi_c \leq -\sin\delta \tag{A.12}$$

and partially visible when

$$-\sin\delta \leq \cos\alpha_c \cos\phi_c \leq \sin\delta \tag{A.13}$$

A.6 Spot centred on the limb of the star

Suppose first that $x_p = 0$. It is straightforward to show that the spot circumference appears in projection as a straight line perpendicular to the radius vector to (y_c, z_c) and the integration limits are

$$\theta_c - \delta \leq \theta \leq \theta_c + \delta \qquad \frac{R\cos\delta}{\cos(\theta - \theta_c)} \leq s \leq R \tag{A.14}$$

A.7 Fully visible spot

Suppose now that $x_c \neq 0$. For a fully visible spot, at any time the projected spot will appear as an ellipse centred on (y_c, z_c). The semi-major axis is perpendicular to the radius vector to (y_c, z_c) and some straightforward algebra shows that it has length $l_1 = R\sin\delta$. To determine the semi-minor axis we require to solve for the value(s) of s at which the spot projection intersects the radius vector through (y_c, z_c). Clearly, at the points of intersection we have

$$y = s\cos\theta_c \qquad z = s\sin\theta_c \tag{A.15}$$

From eq. A.9 it follows that

$$x = \frac{R^2 \cos^2 \delta - y y_c - z z_c}{x_c} \tag{A.16}$$

Combining eqs. A.8 and A.16 gives

$$(R^2 \cos^2 \delta - y y_c - z z_c)^2 + y^2 x_c^2 + z^2 x_c^2 = R^2 x_c^2 \tag{A.17}$$

which, substituting from eqs. A.6 and A.15, may be reduced to the quadratic equation in s

$$R^2 \cos^2 \delta - 2 s_c s + s^2 - R^2 \cos^2 \alpha_c \cos^2 \phi_c = 0 \tag{A.18}$$

This has determinant, Δ, which some algebra reduces to

$$\Delta = 4R^2 \cos^2 \alpha_c \cos^2 \phi_c \sin \delta \tag{A.19}$$

Hence eq. A.18 has roots

$$s = s_c \pm R \cos \alpha_c \cos \phi_c \sin \delta \tag{A.20}$$

from which we see immediately that the projected spot ellipse has semi-minor axis $l_2 = R \cos \alpha_c \cos \phi_c \sin \delta$.

We can parametrise a general point inside this ellipse as

$$y_E = \omega \, l_1 \, \cos \theta_E \qquad z_E = \omega \, l_2 \, \sin \theta_E \tag{A.21}$$

Where $0 \leq \omega \leq 1$ and $0 \leq \theta_E \leq 2\pi$. The coordinates (y_E, z_E) are related to (y, z) via

$$\begin{aligned} y &= y_E \sin \theta_c + z_E \cos \theta_c + s_c \cos \theta_c \\ z &= z_E \sin \theta_c - y_E \cos \theta_c + s_c \sin \theta_c \end{aligned} \tag{A.22}$$

The integral in eq. A.8 may then be expressed in terms of ω and θ_E, viz

$$\Delta F = l_1 l_2 \int_{\theta_E=0}^{2\pi} \int_{\omega=0}^{1} [I_{\rm sp}(s, \theta) - I_*(s)] \; A(d) \, \omega \, d\omega d\theta_E \tag{A.23}$$

A.8 Partially visible spot

The case where a spot is only partially visible is slightly more complicated. Consider the intersection of the projected spot ellipse with a circle of radius s on the stellar disk

and centered on O. Putting $y = s\cos\theta$, $z = s\sin\theta$, $y_c = s_c\cos\theta_c$, $z_c = s_c\sin\theta_c$ and substituting in eq. A.9, gives, after some further reduction

$$\cos(\theta - \theta_c) = \frac{R^2\cos^2\delta - x_c\sqrt{R^2 - s^2}}{ss_c} \tag{A.24}$$

or, writing in terms of α_c and ϕ_c,

$$\theta = \theta_c \pm \cos^{-1}\left[\frac{R\cos\delta - \cos\alpha_c\cos\phi_c\sqrt{R^2 - s^2}}{s(\sin^2\alpha_c\cos^2\phi_c + \sin^2\phi_c)^{1/2}}\right] \tag{A.25}$$

Thus, for a partially visible spot we integrate eq. A.8 using the limits

$$s_c - R\cos\alpha_c\cos\phi_c\sin\delta \leq s \leq R \tag{A.26}$$

for s and using eq. A.25 to define the corresponding limits of θ.

Bibliography

Abe F., et al., 1997, in Ferlet R., ed., Variable Stars and the Astrophysical Returns of the Microlensing Surveys

Afonso C., et al., 2000a, ApJ, 532, 340

Afonso C., et al., 2000b, A & A, in press/astro-ph/0106231

Agol E., 1996, Mon. Not. R. Astron. Soc., 279, 571

Albrow M. D., et al., 2001, ApJ, 550, L173

Albrow M. D., et al., 1998, ApJ, 509, 687

Albrow M. D., et al., 1999a, ApJ, 522, 1022

Albrow M. D., et al., 1999b, ApJ, 522, 1011

Albrow M. D., et al., 2001b, ApJ, 549, 759

Alcock C., et al., 1995, ApJ, 454, L125

Alcock C., et al., 1997a, ApJ, 491, 436

Alcock C., et al., 1997b, ApJ, 486, 697

Alcock C., et al., 2000, ApJ, 542, 281

Ansari R., et al., 1995, A&A, 299, 21

Ansari R., et al., 1996, A&A, 314, 94

Boden A. F., Shao M., van Buren D., 1998, ApJ, 502, 538

Castro S., Pogge R. W., Rich R. M., DePoy D. L., Gould A., 2001, ApJ, 548, L197

Chang K., Refsdal S., 1979, Nature, 282, 561

Chang K., Refsdal S., 1984, A & A, 132, 168

Coleman I. J., 1998, Ph.D. Thesis, pp 34

Craig I. J. D., Brown J. C., 1986, Inverse problems in astronomy. Adam Hilger

Di Stefano R., Esin A. A., 1995, ApJ, 448, 1

Diaz-Cordoves J., Claret A., Gimenez A., 1995, A & AS, 110, 329

Dominik M., 1998, Astron. Astrophys., 333, 893

Dominik M., 1999, A & A, 349, 108

Fluke C. J., Webster R. L., 1999, Mon. Not. R. Astron. Soc., 302, 68

Gaudi B. S., Gould A., 1999, ApJ, 513, 619

Gaudi B. S., Sackett P. D., 2000, ApJ, 528, 56

Gilliland R. L., Dupree A. K., 1996, ApJ, 463, L29

Gould A., 1994, ApJ, 421, 71

Gould A., 1997, ApJ, 483, 989

Gould A., 2001, PASP, 113, 903

Gould A., Han C., 2000, ApJ, 538, 653

Gould A., Welch D. L., 1996, ApJ, 464, 212

Gray N., 2001, in Menzies J. W., Sackett P. D., eds, Microlensing 2001: A New Era of Microlensing Astrophysics Vol. in press

Griest K., Hu W., 1992, ApJ, 397, 362

Gyuk G., Gates E., 1998, Mon. Not. R. Astron. Soc., 294, 682

Han C., Park S., Kim H., Chang K., 2000, Mon. Not. R. Astron. Soc, 316, 665

Hauschildt P. H., Allard F., Baron E., 1999, ApJ, 512, 377

Hauschildt P. H., Allard F., Ferguson J., Baron E., Alexander D. R., 1999, ApJ, 525, 871

Hendry M. A., Coleman I. J., Gray N., Newsam A. M., Simmons J. F. L., 1998, New Astronomy Reviews, 42, 125

Heyrovský D., Loeb A., 1997, ApJ, 490, 38

Heyrovský D., Sasselov D., 2000, ApJ, 529, 69

Hog E., Novikov I. D., Polnarev A. G., 1995, A & A, 294, 287

Ignace R., Hendry M. A., 1999, Astron. Astrophys., 341, 201

Kerins E., et al. 2001, Mon. Not. R. Astron. Soc., 323, 13

Lasserre T., et al., 2000, A & A, 355, L39

Lennon D. J., Mao S., Fuhrmann K., Gehren T., 1996, AP J, 471, L23

Lindegren L., Perryman M. A. C., 1997, 23rd meeting of the IAU, 14, E18

Loeb A., Sasselov D., 1995, ApJ, 449, L33

Minniti D., Vandehei T., Cook K. H., Griest K., Alcock C., 1998, ApJ, 499, L175

Miyamoto M., Yoshi Y., 1995, AJ, 110, 1427

Nemiroff R. J., Wickramasinghe W., 1994, ApJ, 424, L21

Newsam A. M., Simmons J. F. L., Hendry M. A., Coleman I. J., 1998, New Astronomy Reviews, 42, 121

Orosz J. A., Hauschildt P. H., 2000, A&A, 364, 265

Paczyński B., 1986, ApJ, 304, 1

Peng E. W., 1997, ApJ, 475, 43

Refsdal S., 1964, Mon. Not. R. Astron. Soc, 128, 307

Rhie H. S., Bennet D. P., 2001, ApJ, astro-ph/9912050